A Thesis Submitted for the Degree of PhD at the University of Warwick

Permanent WRAP URL:

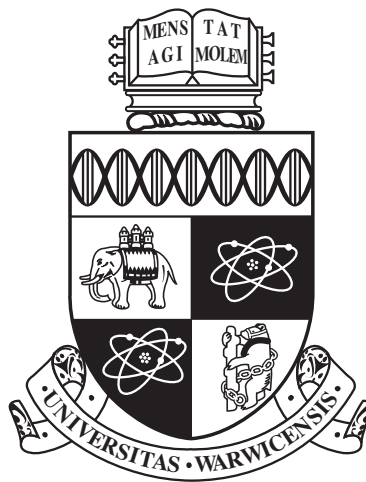http://wrap.warwick.ac.uk/162180

warwick.ac.uk/lib-publications

Study of the skyrmion state stability and metastability with SANS in Ni and Zn substituted Cu_2OSeO_3

by

Marta Crisanti

Thesis

Submitted to the University of Warwick

for the degree of

Doctor of Philosophy

Physics

April 2021

THE UNIVERSITY OF
WARWICK

Contents

Acknowledgments

As these years of my PhD come to an end, I realise how much I have learned and how much life has happened at the same time I was learning. During these four years, I have struggled with several battles on top of the one that is ending as I finish writing this manuscript, and I would have not been able to win any of these without the support of the wonderful people I have met during these years.

As every good student, and as this is written on top of my Thesis, I firstly want to thank from the bottom of my heart Dr. Robert Cubitt, my supervisor in ILL. Bob taught me many things, was super patient, understood my other struggles, and supported me as a human being, not only as his student. His curiosity and passion for the job are contagious, and he managed to transform what to me looked like overwhelming tasks into opportunities to satisfy this curiosity.

I am also profoundly thankful to Prof. Oleg Petrenko, who asked what I thought about the future of my supervision and listened to my opinion. He was always straight forward with me, and he was kind enough to teach me how to use the Laue and read some of this manuscript.

Thanks to Prof. Geetha Balakrishnan. She is an outstanding scientist, and I am thrilled I had such an example of a strong-willed woman so close to me. She was also willing to let me play with her samples, which to me is crazy.

There is a bunch of people who were impactful on my journey, and I will try to mention everyone, although I am sure the writing of this manuscript has made me tired enough to miss someone. Thank you, Beth. You were the first one I managed to open up to when I was in the UK, and I feel very lucky to have had you aside when Don passed away. You will never understand how therapeutic were our calls

Grazie Mamma. Parlando di figure femminili forti e indipendenti che mi hanno resa migliore, tu sei sicuramente la prima fra tutte. Grazie Papà. Sei l'uomo migliore che conosco e questa passione per la scienza è decisamente colpa tua. Grazie Sorella. Vicine o lontane, differenti e simili, sei una roccia a cui conitnuo ad aggrapparmi. Grazie a voi Famiglia, per farmi vivere nel lusso di sapere che, qualsiasi cosa accada, ci siete sempre ad amarmi, supportarmi e accogliermi a braccia aperte. Grazie Haru, la tua morbidezza unica mi sorprende sempre.

Thank you, Don. I always felt like you hired me not only to be your student but because you knew we could be friends, as you said: "...When I interviewed her, I thought that I could go to the pub with this one..". I hope I was able to be both a good student and a good friend to you, even in the little time we were together.

Thank you everyone, now it is time for new adventures.

Marta

Declarations

The experimental work presented in this thesis was performed between January 2017 and March 2020 within the frame of a partnership involving the University of Warwick and the Institut Laue-Langevin (ILL). The sample synthesis was carried out at Warwick by Dr. A. Štefančič, Sam Holt, and Prof. Geetha Balakrishnan. The neutron scattering experiments were performed at the ILL. All neutron data treatments and analyses were performed by myself, with the advise and support of instrument scientists, and in particular of my suprvisor in ILL, Dr. R. Cubitt. The magnetometry measurements were performed by Dr. M. T. Birch at ISIS (Didcot, UK). The experiment described in Chapter 3 was carried out by N. Reynolds, and Dr. J. White. at the Paul Scherrer Institute (PSI, Villigen, CH); the data analysis and interpretation was entirely performed by myself. The content of Chapter 3 lead to a publication in Phys. Rev. B **101**, 214435, (2020). The content of Chapter 4 also lead to a publication in Phys. Rev. B **102**, 224407, (2020). This thesis has been entirely composed by myself and no part has been submitted for examination at any other institute. Part of the work presented in this thesis has been presented under the form of poster and presentations at the following conferences:

- 2017-21 - Skyrmion Project meetings

- 2021 - Unconventional Magnetism Seminars, Institut NEEL, Grenoble (FR)

- 2019 - Theoretical and Experimental Magnetism Meeting, Oxford (UK)

- 2019 - European Conference on Neutron Scattering, St. Petersburg (RU)

- 2019 - Neutron and Muon Science User Meeting, Warwick University (UK)

- 2019 - REIMEI International Workshop, New Excitations in Spintronics, Connemara (IE)

Abstract

Magnetic skyrmions are vortex-like arrangements of magnetic moments and constitute a new topological state of the magnetisation. Skyrmions are characterised by low depinning currents and topological stability. These features make them suitable candidates as information carriers in electronic devices that would be characterised by lower power consumption and a higher data storage density. For technological development, it is crucial to understand skyrmions' characteristics and behaviour in different conditions to ultimately engineer materials with specifications tailored to their needs. Fundamental research on skyrmion materials is needed to identify new avenues for skyrmionic technological developments.

In this thesis, we investigate the properties of the skyrmion lattice in the bulk chiral magnet Cu_2OSeO_3 and its Ni and Zn chemically substituted compounds. We present a thorough investigation of the effect of hydrostatic pressure on the skyrmion state, with particular attention given to the choice of pressure transmitting medium. Our measurements indicate how pressure can be exploited as a third thermodynamic coordinate to the magnetic phase diagram of a bulk skyrmion host. The stability and structure of the skyrmion state have also been studied related to the macroscopic shape of the sample. Although the skyrmion lattice is imagined to be uniform across bulk materials, we show that demagnetisation effects induce several discontinuities in the lattice affecting its shape and stability. Demagnetisation also affects the decay of the metastable skyrmion state, inducing longer lifetimes in specific regions of the sample. Our measurements highlight the importance of considering demagnetisation effects when studying the skyrmion state. We also present a more detailed work on the decay of the metastable skyrmion state. We extracted the velocity of Bloch points, that mediate the decay, from measurements of the lifetime and mean correlation length of skyrmion tubes.

This thesis's work provides insights on the skyrmion state characteristics and shows how small angle neutron scattering (SANS) technique can be used to provide information on the three dimensional ordering of the skyrmion lattice structure. Moreover, we show how SANS can also provide information on the dynamic of the metastable skyrmion state.

Chapter 1

Introduction

In this chapter an introduction to skyrmionics, magnetic neutron scattering, and small angle neutron scattering is given. The content of this chapter is the result of the study of the several sources cited within the text, in particular of [1, 2] for the skyrmion topology; [3–6] for neutron scattering; and of [7] for small angle neutron scattering.

1.1 Skyrmions

The concept of a skyrmion was introduced by the English physicist Tony Skyrme in 1962. Skyrme was building up a theory that could take into account the stability of hadrons: in fact, in quantum field theory, particles are represented as wave-like excitations of the ground state, so they do not correspond to the lowest energy configuration of the system, which brings questions on the nature of their stability. In Skyrme's theory, fundamental particles are described as topological solitons characterised by a topological charge that cannot be modified by continuous deformations of the field, explaining their stability [8]. Although Skyrme's theory was developed in the context of high energy physics, the concept of skyrmions found applications also in condensed matter physics [9–11]. Several years after the work of Skyrme, pioneering theoretical work showed the possibility of stabilising magnetic vortices, analogous to superconducting vortices in superconductivity, in materials with specific crystal structures [12]. Later on, the Dzyaloshinskii-Moriya (DM) interaction was identified as a possible major cause for the stabilisation of such magnetic skyrmion states, both in bulk materials lacking inversion symmetry [13] and in thin films and multilayers [14]. In 2006, in [15], it was shown that the skyrmion state can be stabilised without the application of an external magnetic field, and that it represents the real magnetic ground state. Eventually, magnetic skyrmions were experimentally observed by means of small angle neutron scattering (SANS) in the chiral magnet MnSi [16] in 2009 and by Lorentz transmission electron microscopy in $Fe_{1-x}Co_xSi$ [17] in 2010. At the same time, skyrmions were observed in other materials belonging to the same non-centrosymmetric space group $P2_13$, such as FeGe [18], and Cu_2OSeO_3 [2], where the presence of the Dzyaloshinskii-Moriya interaction induces the necessary chirality to stabilise the skyrmion lattice through thermal fluctuations. Since then, skyrmions have also been observed in centrosymmetric materials [19, 20], where magnetic frustration plays a major role in their stabilization, and in Co-Zn-Mn alloys [21], where, remarkably, the skyrmion state is stable at room temperature. Skyrmions have also been observed in thin films materials, better suited for technological applications, where the lack of inversion symmetry at the interface allows the stabilisation of these chiral structures [22–24].

After their discovery, skyrmions were identified as possible information carriers in spintronic devices, mainly because of the very low current densities needed for their motion, compared to typical domain walls [25, 26]. The interest towards the technological application of skyrmions has not only driven research efforts towards devices [27], but also towards the physics behind their stabilisation, and the
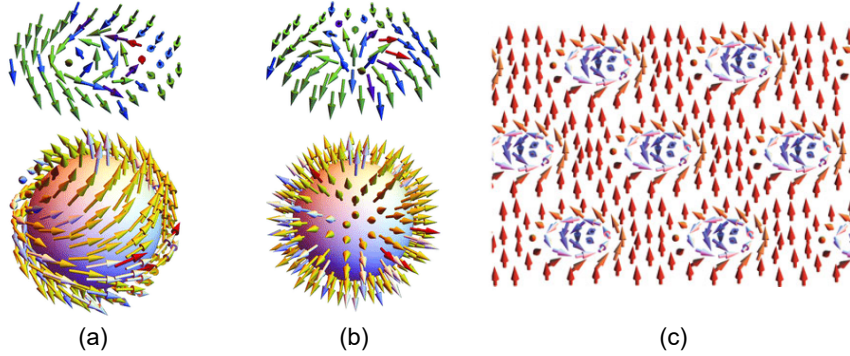
Figure 1.1: **(a)** a Bloch type skyrmion and its stereographic projection onto a sphere **(b)** a Néel type skyrmion and its stereographic projection onto a sphere. **(c)** a skyrmion lattice. (a) and (b) were adapted from ref. [29], (c) was adapted from ref. [30].

understanding of their manipulation [28].

1.1.1 Skyrmion topology

A magnetic skyrmion is a nanosized spin whirl where the spins, or magnetic moments, are pointing in all directions, and it can be described as the projection on a plane of a sphere wrapped by spins, as shown in Figure 1.1. A skyrmion is a topological object, and its spin configuration can be represented as a knot, or a defect, in the continuum identified with a uniformly magnetised state. What characterise this defect is an integer, nontrivial ($\neq 0$) topological charge, providing it its topological stability. The topological charge of a skyrmion, $N = 1$, corresponds to the number of wrappings that the spins constituting the skyrmion do on a unit sphere. The topological charge is also referred to as the winding number, defined as:

$$N = \frac{1}{4\pi} \int d^2r \left(\frac{\partial \hat{\boldsymbol{n}}}{\partial x} \times \frac{\partial \hat{\boldsymbol{n}}}{\partial y} \right), \tag{1.1}$$

where $\hat{\boldsymbol{n}} = \mathbf{M}/|\mathbf{M}|$ is the unit vector describing the direction of the magnetisation of the skyrmion spin texture. For spins wrapping a unit sphere such as shown in Figure 1.1. Several spin textures can have the same winding, or skyrmion number, while differing from each other for their vorticity and helicity, quantities describing the way in which the spins are wrapping the unit sphere, resulting in additional tilting angles in the projection of the spin texture onto a plane [1, 27], as shown in Figure 1.2. To define mathematically the vorticity and helicity, one can start writing the magnetisation of the skyrmion of radius R in polar coordinates $\mathbf{r} = (r cos\varphi, \ r sin\varphi)$, which can be defined as:

$$\mathbf{n}(\mathbf{r}) = (cos\Theta(\varphi)sin\Phi(r), \ sin\Theta(\varphi)sin\Phi(r), \ cos\Phi(r)). \tag{1.2}$$

Inserting this into Equation 1.1, one obtains

$$N = \frac{1}{4\pi} \int_0^R dr \int_0^{2\pi} d\varphi \frac{\partial\Theta(r)}{\partial r} \times \frac{\partial\Phi(\varphi)}{\partial\varphi} \tag{1.3}$$

$$= [cos\Theta(r)]_{r=0}^{r=R} \ [\Phi(\varphi)]_{\varphi=0}^{\varphi=2\pi} \tag{1.4}$$

Where Θ identifies the out-of-plane components of the magnetisation, while Φ identifies the in-plane components. In general, the core of the skyrmion will have the magnetic moment pointing antiparallel to the external field $\mathbf{H}$, hence $\Theta(0) = \pi$, while its outskirt will orient parallel to the field, $\Theta(R) = 0$, giving $[cos\Theta(r)]_{r=0}^{r=R} = 2$. The second part of Equation 1.4 is the definition of the vorticity $m = [\Phi(\varphi)]_{\varphi=0}^{\varphi=2\pi}$ describing the in-plane configuration of the spin texture. The helicity γ is the phase difference that can appear in the rotation of the magnetisation, and models the chirality of the magnetisation as:

$$\Phi(\varphi) = m\varphi + \gamma. \tag{1.5}$$

Bloch-type skyrmions and Néel-type skyrmions present the same topological charge $N = 1$, and same vorticity, while differ in their helicity, as shown in Figure 1.2, where multiple spin texture associated with the same topological charge are represented. For a Néel-type skyrmion with spins pointing down at its edge, the rotation of the spins from the core to the edge can happen with the spins either pointing away from its core for $\gamma = 0$, Figure 1.2(a), or towards it for $\gamma = \pi$, Figure 1.2(c). A Bloch-type skyrmion with spins pointing down at its edge will have the spins rotating counterclockwise, Figure 1.2(b), or clockwise, Figure 1.2(d), depending on its helicity $\gamma = \pm\pi/2$.

A topologically trivial configuration of the magnetisation is characterised by $N = 0$, which is the case for a uniform magnetisation, such as the field-polarised state. The transformation of one structure with a defined topological charge into another structure with the same topological charge can happen continuously. However, it is not possible to pass between two states with different topological charges in a continuous way [1, 15, 31]. The competing magnetic states to the skyrmion state, such as the helical, conical, and uniform magnetisation states, are all characterised by $N = 0$. Hence a discontinuous deformation is needed to pass from the skyrmion state, with $N = 1$, to any of these competing states, making the skyrmion
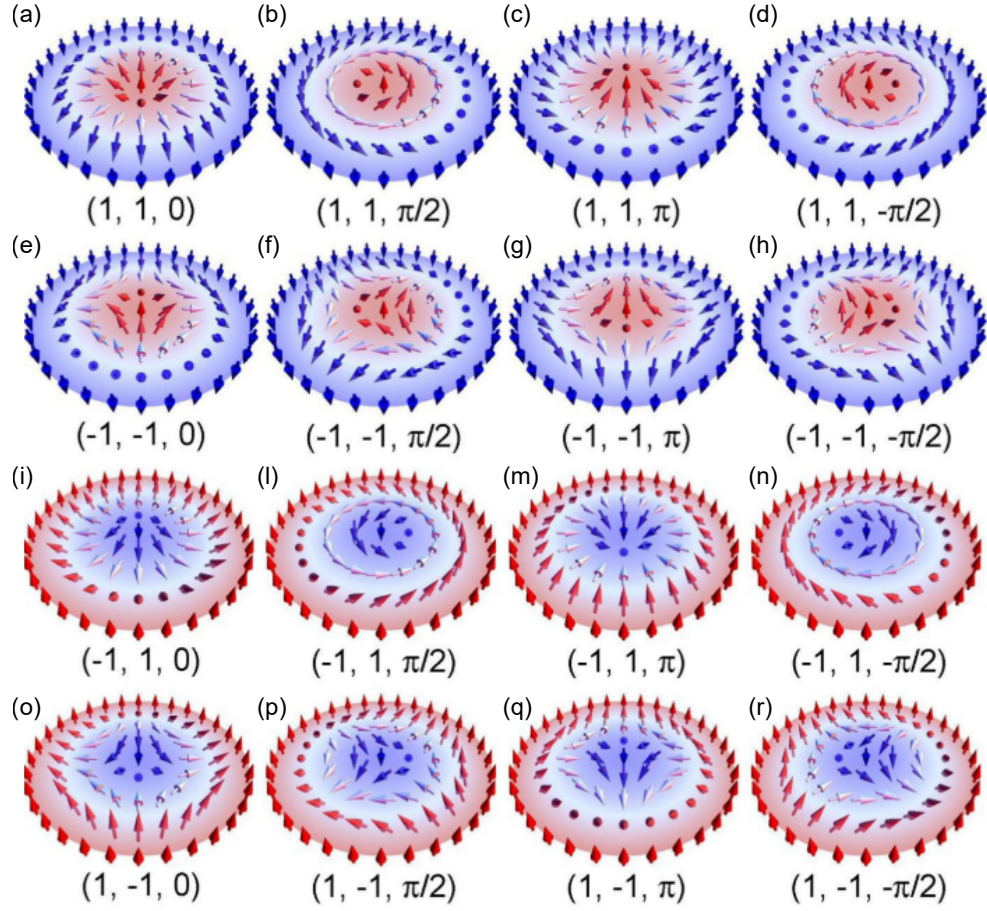
Figure 1.2: Different magnetic skyrmion spin textures characterised by different topological charge, vorticity and helicity, expressed by the numbers (N, m, γ).Reproduced from ref. [27].

a topologically stable state of the magnetisation.

These topological transformations can be thought of as making a vase out of clay. When one starts with a ball of clay, this can be continuously deformed into a vase, hence the ball and the vase are topologically equivalent. If one wants a handle on the vase, either a piece of clay needs to be added on an already shaped vase, or a hole need to be pierced in the ball when starting to shape the vase. The discontinuity in this transformation is due to the fact that a vase with a handle is not topologically equivalent to one without.

1.1.2 Skyrmion stabilisation

As mentioned previously in this chapter, several mechanisms can stabilise the skyrmion state and often contribute simultaneously. In thin films with a perpendicular easy

axis anisotropy, that favours an out-of-plane magnetisation, the competition with long range dipolar interactions, favouring an in-plane magnetisation, results in the stabilization of magnetic stripe domains where the moments rotate in the plane perpendicular to the thin film. In these materials, the application of small magnetic fields leads to the stabilisation of magnetic bubbles, which show the same topology as skyrmions, and have been extensively studied in the 1970s for their potential device application [32, 33]. In non-centrosymmetric materials, the competition between the DM interaction and the magnetic exchange induces the stabilisation of a helical zero field magnetic ground state, and of the skyrmion state in a small region of the $\boldsymbol{H}$-$\boldsymbol{T}$ phase diagram below the ordering temperature T_{C} [2, 16, 18, 21, 34]. The DM interaction is also present at the interface of thin films, where the spatial inversion symmetry is naturally broken, allowing the formation of atomic scale skyrmions [23, 24]. The presence of skyrmions was also theorised and observed in non-centrosymmetric materials with magnetic frustration as the source of the skyrmion state [19, 20, 35].

Among these major mechanisms that allow the formation of the skyrmion state, one of the most studied, and the most relevant for this work, is the competition between the exchange and DM interactions. The Dzyaloshinskii-Moriya interaction originates from the relativistic spin orbit coupling in the absence of inversion symmetry [36]. This interaction favours a 90° canting between neighbouring spins, competing with the exchange interaction which tends to align neighbouring spins. This canting can induce the presence of modulated spin structures with periodicity that are on large scales ($100 \sim 1000\text{Å}$) compared to the underlying atomic structures (Å). In this condition, a continuum model can be used to describe the magnetism of these materials [36], where the Hamiltonian for MnSi, a prototypical non-centrosymmetric skyrmion host, can be written as a sum of different terms [37]:

$$H = \int \left(H_Z + H_{EX} + H_{DM} + H_A \right) d^3r. \tag{1.6}$$

The first term corresponds to the Zeeman effect:

$$H_Z = -\frac{1}{a^3}\mathbf{M} \cdot \mathbf{B}, \tag{1.7}$$

where $\mathbf{M}$ is the magnetisation, $\mathbf{B}$ the external field, and a the lattice constant. The Zeeman interaction arises from the interaction of the magnetic moments with the external applied magnetic field and favours the alignment of the magnetisation vector along the direction of the external field. The second term in Equation 1.6 is related to the Heisenberg exchange interaction:

$$H_{EX} = \frac{J}{2a}(\nabla \mathbf{M})^2, \tag{1.8}$$

where J is the exchange parameter. $J > 0$ for MnSi, as it is a ferromagnet, for antiferromagnets $J < 0$. The interaction between neighbouring spin gives this contribution to the energy of the system, hence the exchange interaction is short ranged. The next term in Equation 1.6 corresponds to the Dzyaloshinskii-Moriya interaction:

$$H_{DM} = \frac{\mathbf{D}}{a^2} \, \mathbf{M} \cdot (\nabla \times \mathbf{M}) . \tag{1.9}$$

The DM represents the main contribution deriving from the spin-orbit coupling in crystal structures lacking in inversion symmetry, like the case of MnSi. $\mathbf{D}$ is a vector that depends on the symmetry of the magnetic exchange path between the two involved spins. The DM contribution can be seen as a small perturbation on the underlying ferromagnetic or antiferromagnetic structure (J), leading to modulated spin structures with propagation vectors D/J, that are long compared to the typical characteristic dimensions of the unit cell. As the orientation and sign of the vector $\mathbf{D}$ depend only on the symmetry of the crystallographic structure of the system, the modulated magnetic structures arising from this interaction present a single handedness [38]. The breaking of inversion symmetry inducing DMI can be induced locally by different causes than the crystallographic structures, such as interfaces [23, 24] and defects [39].

The last and weakest term H_A represents the magnetocrystalline anisotropy, which is responsible for determining the magnetic easy axes of the material. Similarly to the DM interaction, the origin of the anisotropy is in the spin-orbit coupling and represents the amount of energy required to overcome the coupling between the spin and the orbital motion of the electron while rotating a spin away from the easy axis of the magnetisation. The magnitude of crystal anisotropy diminishes with increasing temperature and vanishes at the ordering temperature.

For a cubic system, the magnetocrystalline anisotropic energy density can be expressed as

$$\frac{E}{V} = K_0 + K_1(\alpha^2\beta^2 + \beta^2\gamma^2 + \gamma^2\alpha^2) + K_2\alpha^2\beta^2\gamma^2 + O^4, \tag{1.10}$$

where K_0, K_1 and K_2 are the parameters of the anisotropy, and α, β and γ are the cosines of the angles between the local magnetisation and the crystal axes. All the higher order terms are included in O^4. When $K_2 = 0$, the easy direction is determined by K_1 and it is $\langle 100 \rangle$ for $K_1 > 0$, while it is $\langle 111 \rangle$ for $K_1 < 0$. When
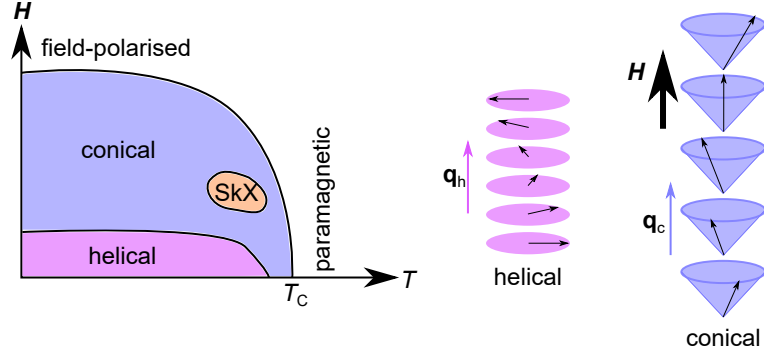
Figure 1.3: Generic $\boldsymbol{H}$-$\boldsymbol{T}$ phase diagram for non-centrosymmetric skyrmion hosts, where the stabilisation mechanism of the skyrmion state is determined by the interplay between the exchange interaction and the DMI. The characteristics of the helical and conical magnetic structures are also shown.

$K_2 \neq 0$ also the $\langle 110 \rangle$ direction is allowed as a easy axis [40]. In B20 materials, the balance of these components of the anisotropy determines the direction of the helical propagation vectors which is [111] for MnSi, and the main crystallographic axes [100], [010] and [001] for Cu_2OSeO_3.

The role of cubic anisotropy in the stabilization of the skyrmion state is recently at the centre of new interest, as its effect does not seem to be so marginal as that was first thought. Specifically, both in MnSi [41] and $Co_8Zn_8Mn_4$ [42], an increase of the effective anisotropy at low temperatures is identified as responsible for a hexagonal to square transition of the skyrmion lattice. In Cu_2OSeO_3, the strong spin-orbit coupling leads to unusually large values of the cubic anisotropy which, at low temperature, is observed tilting the conical state from the direction of the applied field and stabilising a low temperature skyrmion phase [43–45].

The interplay among the aforementioned internal interactions in MnSi leads to a $\boldsymbol{H}$-$\boldsymbol{T}$ phase diagram whose main characteristics are generic for bulk non-centrosymmetric skyrmion hosts, as they share the same mechanism of the skyrmon stabilisation. A generic phase diagram for this class of materials is shown in Figure 1.3. The ground state of the Hamiltonian in Equation 1.6 is a single-$\mathbf{q}$, multi domains helical state, where the wave vector's magnitude $|\mathbf{q}| = D/J$ and it is related to the wavelength of the helix by $q = 2\pi/\lambda$. In the helical state, the moments turn on a plane perpendicular to the propagation vector. With the application of an external magnetic field, the system turns into a single domain conical state, where, compared to the helical state, the moments exhibit an additional tilt towards the direction of the external field, as shown in Figure 1.3.

The skyrmion state, surrounded by the conical state, is stable over a narrow

temperature and field region of the **H-T** phase diagram near the ordering temperature, where thermal fluctuations stabilise it. This area of the phase diagram was previously referred to as the A phase (for anomalous), but it is now commonly referred to as the skyrmion pocket. The structure of the magnetisation in the skyrmion state can be written as:

$$\mathbf{M}(\mathbf{r}) \approx \mathbf{M}_{\text{uniform}} + \sum_{i=1}^{3} \mathbf{M}_{\mathbf{q}_i}(\mathbf{r} + \Delta \mathbf{r}_i), \tag{1.11}$$

$$\mathbf{M}_{\mathbf{q}_i}(\mathbf{r}) = A[\mathbf{n}_{i1} cos(\mathbf{q}_i \cdot \mathbf{r}) + \mathbf{n}_{i2} sin(\mathbf{q}_i \cdot \mathbf{r})]. \tag{1.12}$$

where Equation 1.12 is the magnetisation of a single helix with amplitude A and wave vector q_i. Each helix have a phase $\mathbf{q}_i \cdot \Delta \mathbf{r}$. In Equation 1.11, $\mathbf{M}_{\text{uniform}}$ is the uniform state of the magnetisation that the Zeeman effect would induce. This formulation, with the three $\mathbf{q}$ perpendicular to the direction of the applied field, with a relative angle between each other of 120°, and satisfying the relation

$$\sum_{i=1}^{3} \mathbf{q}_i = 0, \tag{1.13}$$

represents the skyrmion crystal. In small angle neutron scattering, this arrangement of the magnetisation produces a hexagonal scattering pattern, typical signature of the ordering of the skyrmion state [16]. Skyrmions extend in the direction of the applied magnetic field in a tube-like fashion, in which ideally, each layer of moments would correspond exactly to the same skyrmion lattice [46], as shown in Figures 1.4(a) and (b). However, it has been shown that skyrmions can present a variation in their configuration along their length, passing from Néel-type in the bulk, to Bloch-type skyrmions on the surface [47]. Moreover, skyrmion tubes can present topological defects along their length, known as Bloch points, identified by the red dots in Figure 1.4(b) [31, 48].

Bloch points constitute a divergent configuration of the magnetisation, where the magnetisation rotates by 180° in the space of a single spin, and they have been referred to as emergent magnetic monopoles [31, 50]. The spin configuration of a Bloch point is reported in Figure 1.4(c). The creation and motion of these defects have been identified as responsible for both the creation and annihilation of skyrmion tubes [51–53]. Stable structures involving Bloch points consists of short skyrmion tubes ending in a Bloch point near the surface, referred to as a chiral Bobber [48], and observed in FeGe lamellae [54].

9
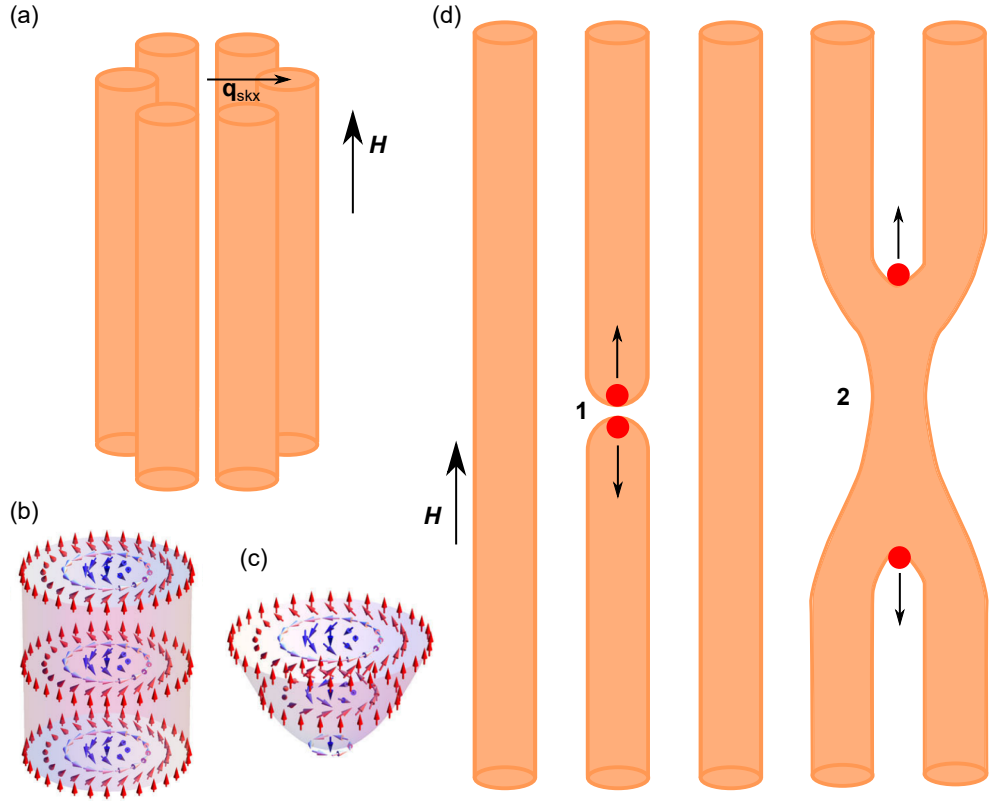
Figure 1.4: (a): skyrmion tubes elongating along the direction of the applied field, arranged in an hexagonal lattice. The propagation vector is perpendicular to the direction of the magnetic field. (b): illustration of the topological texture of a single skyrmion tube. (c): representation of a Bloch point. (d): illustration of two mechanisms of unwinding of the skyrmion tubes through the movement of the Bloch points marked in red. Reproduced and adapted from [27, 49].

1.1.3 Tuning of the skyrmion state

For practical device applications, the skyrmion state has to be ideally stabilised at room temperature and zero magnetic field. However, as shown in Figure 1.3, the skyrmion state is stable only over a narrow region of the $\boldsymbol{H}$-$\boldsymbol{T}$ phase diagram of chiral bulk materials. For this reason, several methods have been studied and developed to control the position and dimensions of the skyrmion pocket.

The reduction of the sample dimensions into thin films was proven effective for a massive enhancement of the skyrmion pocket [17, 22, 55]. This enhancement is linked to the fact that, when the field is applied perpendicular to the thin film, the conical state is destabilised compared to the skyrmion state, as the moments have increasingly less space to turn as the sample thickness diminishes [17].

The application of electric fields in the only insulating and multi-ferroic skyrmion host Cu_2OSeO_3 was also proven as a valid mechanism for manipulating the size of the skyrmion pocket [53, 56–58]. The electric field enhances the size of the skyrmion pocket and acts as a switch between the conical and skyrmion states for temperatures near to the low temperature boundary of the skyrmion pocket at $E = 0$.

The application of uniaxial pressure was observed to induce a selective enlargement of the skyrmion pocket when the pressure is applied perpendicular to the magnetic field [59–61]. These results were interpreted as an effect related to a stress induced magnetic anisotropy in MnSi [60], while as an effect of increased DM interaction in Cu_2OSeO_3 [61]. Increasing hydrostatic pressure in MnSi is reported to decrease the ordering temperature and suppress the helimagnetic ordering [45, 62]. In Cu_2OSeO_3, the ordering temperature increases and a shift towards higher temperatures of the whole $\boldsymbol{H}$-$\boldsymbol{T}$ phase diagram is observed [62–65]. The extraordinary sensitivity of chiral bulk skyrmion hosts to the application of both uniaxial and hydrostatic pressure highlights the fine interplay of the different magnetic interactions needed for the stabilisation of the skyrmion state.

Another way to manipulate the fine energy balance that characterises this set of skyrmion hosts is controlled chemical substitution. The elemental composition is modified with varying results affecting the various energy terms of Equation 1.6. Chemical substitution has been studied in several systems, such as $Fe_{1-x}Co_xSi$ [66], $Co_{10-x}Zn_{10-y}Mn_{x+y}$ [21, 67], $GaV_4(S_{8-x}Se_x)$ [68, 69], and several others. In this work we focus on $[Cu_{1-x}(Zn/Ni)_x]_2OSeO_3$ [49, 53, 63, 70–72]. The effects induced by the chemical substitution include a variation of T_C, accompanied by a variation in J; a variation in the DMI vector $\mathbf{D}$ identified by a change in chirality and periodicity of the skyrmion and helimagnetic states; a modification of the magnetic anisotropy,

hence a modification of the low T, zero field, state orientation.

1.1.4 Metastable Skyrmions

Metastable skyrmions constitute another way to overcome the narrow size of the skyrmion pocket and were observed for the first time after rapid field cooling (FC) through the skyrmion pocket down to low temperatures [73]. This procedure quenches the skyrmion state out of its equilibrium region in the $\boldsymbol{H}$-$\boldsymbol{T}$ phase diagram; some skyrmions survives in a metastable state that is present over a wide parameter range. Up to now, the metastable skyrmion state has been observed and studied in several skyrmion materials such as MnSi [41, 74, 75], Cu_2OSeO_3 [43, 49, 56, 58], Co-Zn-Mn [42, 67, 76] alloys and $Fe_{0.5}Co_0.5Si$ [31, 73]. As this state is metastable, it only represents a local minimum of the system, separated from the energy ground state by an energy barrier ΔE. This energy barrier can be overcome via thermal fluctuations, inducing a decay into the magnetic ground state of the system with a characteristic lifetime. Three major factors determine the characteristics of the metastable skyrmion state and its decay: the cooling rate, which determines its population [49]; as well as the target temperature [41–43, 56, 67, 73–77] and the disorder of the underlying crystal structure [49], both of which determine its lifetime. The inherent instability of the metastable skyrmion state appears to be problematic for device applications. However, it has been shown that, for a temperature sufficiently lower than the ordering temperature, the metastable skyrmion state has a lifetime long enough to be suitable for applications [75, 78, 79]. Specifically, for $Co_9Zn_9Mn_2$ a metastable skyrmion state with an exceptionally long lifetime was observed at zero applied field and room temperature [67].

The decay mechanism of the skyrmion tubes in bulk samples is mediated by Bloch points [31, 51, 74]. When the metastable skyrmion state decays into the conical state, two Bloch points let two adjacent skyrmion tubes merge together and then move away from each other, acting like a zip [31], as depicted in Figure 1.4, scenario 2. When the transition is towards the conical state, the Bloch points unwind the configuration of one single skyrmion tube by moving along it [51, 74]. The Bloch points act like sources and sinks of topological charge, mediating the transition between two topologically different states of the magnetisation [31, 74].

The motion of Bloch points can be influenced via applied electric currents, providing a direct tool for the manipulation of this unwinding mechanism. Moreover, this motion is also influenced by the underlying crystal structure, as observed in $Co_9Zn_9Mn_2$ and $Fe_{0.5}Co_0.5Si$, that have a more disordered structure than MnSi [41], and present longer lifetimes for the metastable skyrmion state. A similar effect

has also been observed in Zn and Ni substituted Cu_2OSeO_3, compared to pristine Cu_2OSeO_3. The chemical substitution induces a certain level of disorder in the underlying crystal structures, given by the random positioning of the dopant ions in the two different Cu^{2+} sites (see Section2.1). This chemically substituted sites act as pinning sites for the Bloch points, inducing longer lifetime in the substituted samples, compared to the pristine parent compound [49, 53, 80].

1.2 Neutron Scattering

Neutron scattering is a powerful tool for the study of bulk samples. Specifically, since the neutron has no net charge, it can penetrate matter better than other particles typically used in scattering measurements, such as electrons and X-rays. This characteristic derives from the fact that neutrons interact through nuclear forces, in the short range of fm (10^{-15} m), travelling far distances in matter without being scattered or absorbed by nuclei. The high penetration power of the neutron allows the study of bulk samples also when they have to be placed in a container (powder samples, liquid, or samples that have to be maintained under pressure or at low/high temperatures).

Neutron scattering is also a very powerful and versatile technique for studying magnetic materials. Neutrons possess an intrinsic magnetic moment that allows them to couple to the magnetic state of the sample, from the orbital motion and spin of single unpaired electrons, to variations in the magnetisation of the sample. The cross section of magnetic neutron scattering is similar to the cross section of nuclear scattering.

The generally weak interaction of neutrons with matter would require very intense neutron sources, which are inherently weak, especially compared with X-ray sources. Neutrons are also very difficult to control given their missing electric charge, which increases the complexity of the building of neutron guides and detectors. The Institut Laue-Langevin (Grenoble, (FR)) with a fission reactor of 57 MW is the most intense stable neutron source available with (10^{15} $ns^{-1}cm^{-3}$), and contributed significantly to the success of a multitude of neutron scattering experiments.

Even with all the drawbacks associated with it, neutron scattering provides crucial information on the structural and magnetic properties of bulk samples, complementary to other techniques such as X-ray scattering, nuclear magnetic resonance, magnetometry, etc.; for this reason it is still a very active and important field in condensed matter.

1.2.1 Crystal lattice and reciprocal lattice

Before introducing the formalism of neutron scattering, it is important to be familiar with the basic concepts of crystal lattice and reciprocal lattice.

A crystal consists of a periodic structure of several identical units that fills space. A crystal has a periodicity defined by a lattice, constructed as

$$\mathbf{R} = n_1\mathbf{a}_1 + n_2\mathbf{a}_2 + n_3\mathbf{a}_3, \tag{1.14}$$

where $\mathbf{a}_1$, $n_2\mathbf{a}_2$ and $\mathbf{a}_3$ are three vectors, not in the same plane, describing the periodicity of the lattice in the three-dimensional space, and are referred to as *primitive vectors*. The arrangement of atoms in the structure is called *motif*.

The *unit cell* is the building block of the crystal, and adding many together fills up the space generated by the whole crystal. Several unit cells can be defined for any given crystal structure: the smallest one contains only one lattice point and it is called *primitive unit cell*.

For all lattices described here, a *reciprocal* lattice exists in wavevector space and consists of the Fourier transform of the real-space lattice. The reciprocal lattice is defined by a set of reciprocal vectors that satisfy the condition:

$$e^{\mathbf{K}\cdot\mathbf{R}} = 1. \tag{1.15}$$

This set can be generated as

$$\mathbf{K} = m_1\mathbf{b}_1 + m_2\mathbf{b}_2 + m_3\mathbf{b}_3, \tag{1.16}$$

where the relationship between the primitive vectors of the two representation is given by [81]:

$$\mathbf{b}_1 = 2\pi\frac{\mathbf{a}_2 \times \mathbf{a}_3}{\mathbf{a}_1 \cdot (\mathbf{a}_2 \times \mathbf{a}_3)}; \ \mathbf{b}_2 = 2\pi\frac{\mathbf{a}_3 \times \mathbf{a}_1}{\mathbf{a}_1 \cdot (\mathbf{a}_2 \times \mathbf{a}_3)}; \ \mathbf{b}_3 = 2\pi\frac{\mathbf{a}_1 \times \mathbf{a}_2}{\mathbf{a}_1 \cdot (\mathbf{a}_2 \times \mathbf{a}_3)}. \tag{1.17}$$

From the definition of reciprocal lattice follows that for a given family of crystallographic planes separated by a distance d, the reciprocal lattice vector associated to them is perpendicular to the set of planes and will have magnitude

$$q = \frac{2\pi}{d}. \tag{1.18}$$
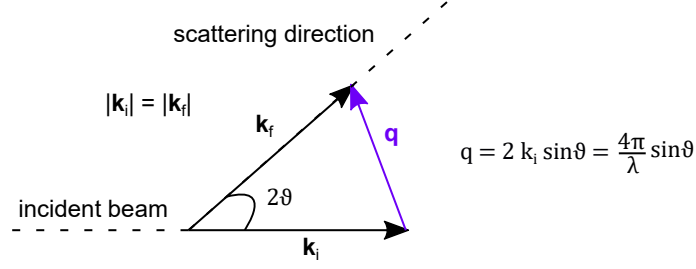
Figure 1.5: Scattering triangle for elastic neutron scattering. The incoming neutron has momentum $\mathbf{k}_i$, it is deflected by an angle 2θ in the diffraction process, and has an outgoing momentum $\mathbf{k}_f$.

1.2.2 Scattering Kinematics

Neutron scattering, as other scattering processes, obeys the laws of momentum and energy conservation expressed by:

$$\mathbf{Q} = \mathbf{k}_f - \mathbf{k}_i, \qquad (1.19)$$

$$\hbar\omega = E_i - E_f, \qquad (1.20)$$

where i and f indicate the neutron's initial and final states during a scattering process that exchange a $\hbar\omega$ quantity of energy. $\mathbf{Q}$ is the scattering vector, identifying the momentum transfer of the scattering process, Figure 1.5. From these considerations, one can distinguish between two basic scattering processes: elastic scattering in which $E_i = E_f$, and inelastic scattering in which the neutron exchanges energy with the nucleus, hence $E_i \neq E_f$. In this work we focus on elastic scattering.

For elastic scattering $|\mathbf{k}_i| = |\mathbf{k}_f| = k$, and the momentum transfer can be written as:

$$Q = 2\ k\ sin\theta = \frac{4\pi}{\lambda} sin\theta. \qquad (1.21)$$

1.2.3 Nuclear neutron scattering from a single nucleus

Formally, scattering is a quantum mechanical process, and it can be described in terms of wavefunctions, as depicted in Figure 1.6. The incident neutron can be represented by a plane wave $\Psi_{in} = Ae^{ik\bar{r}}$, with a definite wave vector $k = 2\pi/\lambda$. $|\Psi_{in}|^2 = |A|^2$ at positions $\bar{r}$, indicating that the neutron has the same probability to be found at any point at distance $\mathbf{r}$. The neutron interacts with the nucleus through nuclear forces that act on a distance range several orders of magnitude smaller than
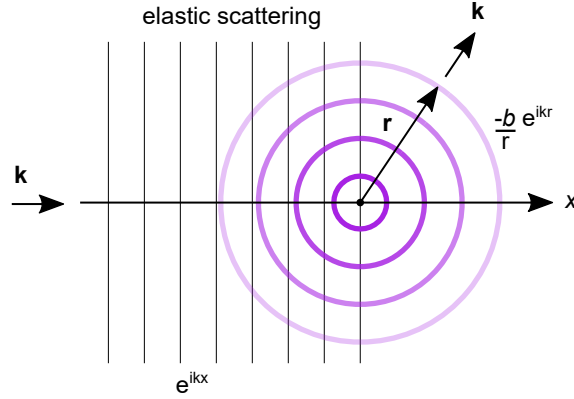
Figure 1.6: Scattering of a plane wave from a single nucleus. Adapted from [4]

the wavelength of a thermal neutron $(10^{-10}m)$. In these conditions, the neutron is scattered isotropically by the nucleus, which acts as a point scatterer. In these conditions, the scattering is isotropic and can be written in terms of a spherical wave function $\Psi_{out} = -b/r\ e^{ik\bar{r}}$, with $|\Psi_{out}|^2 = b^2/r^2$.

The scattered neutron intensity, $|\Psi_{out}|^2$, decreases as $1/r^2$ with distance, as the scattered wavefront grows in size. The constant b, modulating the amplitude of the scattered wave function, refers to the strength of the interaction between the nucleus and the neutron. Apart from particular cases, including elements that are strong neutron absorbers, b can be considered a real number independent from the energy of the neutron. b is commonly referred to as the *scattering length* of a specific nucleus and has to be experimentally determined, or looked up in published tables. The scattering length depends on the details of the interaction between the nucleus and the neutron, as such, its value depends also on the spin state of the nucleus-neutron system. Importantly, b does not show a systematic dependence on the atomic number of the nuclei, instead it shows significant variations among different isotopes of the same element, making neutron scattering very effective for the study of hydrogen rich samples, or compounds made of elements with very similar atomic number.

1.2.4 Nuclear scattering from bound nuclei

Ultimately, real experiments involve neutron scattering from an arbitrary set of bound nuclei. Let us consider a set of nuclei arranged as depicted in Figure 1.7, with d indicating the spacing between each plane of nuclei. In real experiments, the distance between the scattering nuclei and the detector, as much as the distance between the source of the incoming neutrons and the scattering nuclei are far bigger
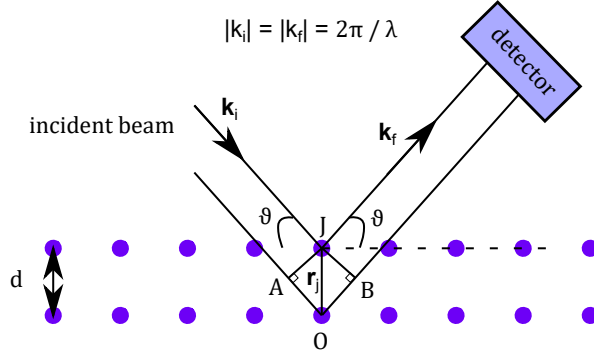
Figure 1.7: A lattice nuclei with characteristic spacing d hit by a neutron beam. The neutron beam is scattered and collected at the detector position.

than d, hence it is possible to assume that the neutron waves with wavelength λ hitting the different nuclei in Figure 1.7 are parallel. The neutron wave hitting the nuclei in position O in Figure 1.7, travels a longer distance compared to the other ray hitting in position J. The additional path is represented by the segment $\overline{AOB}$, which by construction is equal to $2d\ sin\theta$. When this path difference is equal to an integer number of wavelengths of the incoming beam, the scattered waves will be in phase and will produce constructive interference at the detector according to the relation

$$n\ \lambda = 2\ d\ sin\theta. \tag{1.22}$$

This is Bragg's law of diffraction, which gives the condition to be satisfied to have Bragg peaks in the diffracted neutron intensity. Using the Bragg's law it is possible to relate the position of the scattered intensity peaks on the detector plane to the microscopic structure of the material studied d.

As it was just introduced with the Bragg's law, When considering neutron diffraction from a set of bound nuclei, the scattered wave function Ψ_{out} will have to take into account the interference between scattered waves by different nuclei. From Figure 1.7 we consider the j-th nucleus as the nucleus in position J, identified by the vector $\mathbf{r}_j$, with respect to the point O. The phase difference between the neutron wave hitting the nucleus in J and the one hitting the nucleus in O can be expressed as

$$\delta_j = \mathbf{k}_f \cdot \mathbf{r}_j - \mathbf{k}_i \cdot \mathbf{r}_j = \mathbf{Q} \cdot \mathbf{r}_j, \tag{1.23}$$

where $\mathbf{Q}$ is the momentum transfer vector introduced in Equation 1.19. Considering the phase difference in the scattered function at the detector position $\mathbf{R}$,
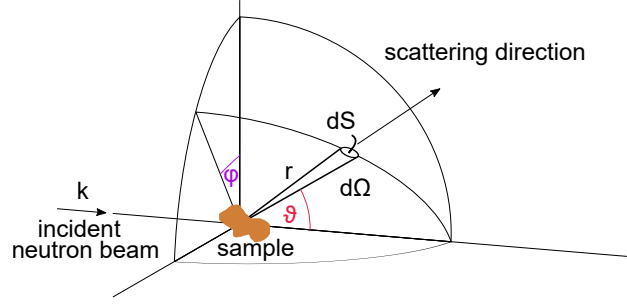
Figure 1.8: Scattering geometry, adapted from [3]

and the scattering from the whole set of nuclei, Ψ_{out} can be written as follow:

$$\Psi_{out}(\mathbf{R}) = e^{ikR} \sum_j -\frac{b_j}{|\mathbf{R} - \mathbf{r}_j|} e^{i\mathbf{Q}\mathbf{r}_j}. \tag{1.24}$$

Since the distance from the sample to the detector is going to be several orders of magnitude bigger than the characteristic spacing of the structure in study, a fair assumption is to consider $\mathbf{R} >> \mathbf{r}_j$. In this case, at the detector position, the scattered intensity $|\Psi_{out}|^2$ will be proportional to:

$$|\Psi_{out}|^2 \propto I(\mathbf{Q}) = \left| \sum_j -b_j e^{i\mathbf{Q}\mathbf{r}_j} \right|^2. \tag{1.25}$$

This equation indicates how the scattered intensity depends on the momentum transfer more than the initial and final state of the neutron, allowing to calculate the scattering from any system provided the previous knowledge of the location and type of the scattering nuclei.

1.2.5 Cross-section

Equation 1.25 does not allow to determine the intensity of the scattering, and to do so, the simplest way is to express the scattering in terms of a cross-section σ. σ represents the effective area of the nucleus seen by the incoming scattering neutron, and it is measured in barns ($10^{-28}m^2$). The total scattering cross-section measures the probability that any scattering event will occur, independently of any change in momentum or energy, and it is defined as

$$\sigma_T = \frac{\text{total neutrons scattered per second}}{\Phi_{in}}, \tag{1.26}$$

where Φ_{in} is the incoming neutron flux, given in neutrons per unit area per second, in the scattering geometry shown in Figure 1.8. The incoming neutron

flux can be expressed as $\Phi_{in} = |\Psi_{in}|^2 v = |A|^2 v$, considering v as the velocity of the incoming neutrons, A the amplitude of the function. The scattered flux at a distance r from the scattering nucleus can be written as $\Phi_{out} = |\Psi_{out}|^2 v = |A|^2 v b^2/r^2$. σ_T takes into account the scattering processes in all directions, hence the flux needs to be integrated over a surface surrounding the whole scattering nucleus, and since the scattering is isotropic the flux can be integrated over a sphere of radius r. Given these considerations, σ_T becomes

$$\sigma_T = \frac{4\pi \; r^2 \times |A|^2 v b^2/r^2}{|A|^2 v} = 4\pi b^2, \tag{1.27}$$

which represents the total scattering cross-section in all directions for a single bound nucleus.

In real experiments, one is usually able to collect scattered neutrons only in specific directions, for this reason the concept of differential scattering cross-section is essential, as it is defined as

$$\frac{d\sigma}{d\Omega} = \frac{\text{neutrons scattered per second into the solid angle } d\Omega}{\Phi_{in} \times d\Omega}, \tag{1.28}$$

where the solid angle can be defined by the dimensions and position of the detector used in the experiment. More correct is to consider $d\Omega$ in the limit of approaching zero, as this corresponds to an infinitesimal area in which the scattered intensity is uniform. Considering the definition of differential scattering cross-section, and the incident and scattered neutron wave functions, for a set of bound nuclei $d\sigma/d\Omega$ is just the function $I(\mathbf{Q})$ that was previously introduced:

$$\frac{d\sigma}{d\Omega} = \left| \sum_j -b_j e^{i\mathbf{Q}\mathbf{r}_j} \right|^2. \tag{1.29}$$

1.2.6 Coherent and Incoherent scattering

As discussed previously, the scattering length b varies widely with the atomic number and the spin state of the neutron-nucleus system. This variation would make the calculation of the scattering cross-section almost impossible, as this implies the knowledge of the isotope and spin state of each nucleus in the sample. However, as the distribution of isotopes and nuclear spins is random, assuming the number of nuclei is large, then the scattering of two samples of the same material will be indistinguishable. This reasoning allows to write the differential cross-section as follows

$$\frac{d\sigma}{d\Omega} = \sum_{jk} \overline{b_j b_k} e^{i\mathbf{Q}\cdot(\mathbf{r}_k - \mathbf{r}_j)}. \tag{1.30}$$

The square modulus has been explicitly written out as the product of one factor and its complex conjugate, with the scattering length considered to be a real number. The bar over the scattering lengths indicates the average over the natural isotopic distribution of the nuclei in the sample. Considering p as the probability of occurrence of a specific isotope, then the average scattering length $\bar{b}$ can be written out as:

$$\bar{b} = \sum_i p_i b_i \ \ \text{and} \ \ \overline{b^2} = \sum_i p_i b_i^2. \tag{1.31}$$

The average scattering length in Equation 1.30 can be written for the case with $j = k$ as $\overline{b_j^2}$, and for the case of $j \neq k$ as $\bar{b}_j \bar{b}_k$. The differential cross-section can be written to explicitly considering this two cases as:

$$\frac{d\sigma}{d\Omega} = \sum_{jk} \overline{b_j b_k} e^{i\mathbf{Q}\cdot(\mathbf{r}_k - \mathbf{r}_j)} + \sum_j (\overline{b_j^2} - \overline{b}_j^2). \tag{1.32}$$

In this expression the differential scattering cross-section is divided in two terms that identify coherent and incoherent scattering processes.

$$\frac{d\sigma}{d\Omega}_{\text{coh}} = \Big| \sum_j \bar{b}_j e^{i\mathbf{Q}\cdot\mathbf{r}_j} \Big|^2, \tag{1.33}$$

$$\frac{d\sigma}{d\Omega}_{\text{inc}} = \sum_j (\overline{b_j^2} - \overline{b}_j^2). \tag{1.34}$$

In coherent scattering processes the scattered neutrons from different nuclei will interfere with each other. These kind of scattering depends on the interatomic distances, and on the scattering vector $\mathbf{Q}$. Elastic coherent scattering describes the structure of the material, inelastic coherent scattering describes collective excitations of atoms such as phonon.

In incoherent scattering processes there is no interference between the scattered wavefunctions. The intensities coming from the scattering of different nuclei add up independently. Elastic incoherent scattering is isotropic and represent a flat background of measurements. Inelastic incoherent scattering provides information on atomic diffusion.

1.2.7 Master Equation

What has been discussed up to now does not consider the quantum mechanical nature of the neutron and only exploits the properties of classical waves usually used in optics. However, for the introduction of magnetic neutron scattering, it is important to derive a more general formula for the differential scattering cross-section.

Let us consider a generic neutron in a state defined by a wavevector $\mathbf{k}_0$, and a spin state σ_0, interacting with a sample in a generic state λ_0. The neutron is scattered by the sample into a final state with a wavevector $\mathbf{k}_1$ and a spin σ_1, while the sample transitions to the state λ_1. The final state of the neutron includes wavevectors falling in a small solid angle $d\Omega$ centred in the direction of $\mathbf{k}_1$, and within a small energy interval dE_f centred at $E_f = \hbar^2 k^2/(2m_n)$, where m_n is the mass of the neutron. With this formulation, the emphasis is on what information about the intrinsic properties of the sample is possible to extract from the measured cross-sections.

The partial differential scattering cross-section can be written as

$$\left(\frac{d\sigma^2}{d\Omega \ dE_f}\right)_{\mathbf{k}_0,\sigma_0,\lambda_0 \to \mathbf{k}_1,\sigma_1,\lambda_1} = \frac{1}{\Phi_{in} \ d\Omega \ dE_f} \sum_{\lambda_0} p_{\lambda_0} \sum_{\lambda_1} W_{\mathbf{k}_0,\sigma_0,\lambda_0 \to \mathbf{k}_1,\sigma_1,\lambda_1}, \quad (1.35)$$

where Φ_{in} is the incident neutron flux at the sample position. It is possible that several different transitions can induce neutrons to pass from their initial to their final state $(k_0\sigma_0) \to (k_1\sigma_1)$, while conserving the energy of the process. This means that after several scattering events, the neutrons will be probing the average over a statistical distribution of initial states of the sample. For this reason we sum over all the possible transitions, which have a contribution defined by the probabilities p_{λ_0}.

As there might be several transitions that can let the system pass from the initial to the selected final state, one can define p_{λ_0} as the probability for the initial state. $W_{\mathbf{k}_0,\sigma_0,\lambda_0 \to \mathbf{k}_1,\sigma_1,\lambda_1}$ indicates the transition rate in the solid angle $d\Omega$, and energy interval dE_f, from the initial state of the neutron and the sample $\mathbf{k}_0, \sigma_0, \lambda_0$ to the final state $\mathbf{k}_1, \sigma_1, \lambda_1$. For simplicity, the initial and final states of the system neutron-nucleus will be identified as $|\mathbf{0}\rangle$ and $|\mathbf{1}\rangle$, respectively.

The transition rate will depend on the interaction potential of the scattering process, that is assumed to be very weak, hence not imposing significant changes to the state of the neutron-nucleus system before and after the interaction (*first Born*

approximation). With this approximation, $W_{\mathbf{0}\rightarrow\mathbf{1}}$ can be written in terms of Fermi's golden rule

$$W_{\mathbf{0}\rightarrow\mathbf{1}} = \frac{2\pi}{\hbar}\,|\langle\mathbf{1}|V(\mathbf{r})|\mathbf{0}\rangle|^2\,\rho_{\mathbf{k}_1\sigma_1}(E_f)\frac{d\Omega}{4\pi}, \tag{1.36}$$

where V is the interaction potential, and $\rho_{\mathbf{k}_1\sigma_1}(E_f)$ represents the density of final states per unit energy. $\frac{d\Omega}{4\pi}$ indicates the fraction of directions in the interval $d\Omega$. Equation 1.36 is only valid for weak interactions, that can be expressed with a first order perturbation theory. This is valid for both nuclear and magnetic neutron scattering since, while in the first case the nuclear potential acts on a very short range, in the second the interaction, although acting on a longer range, it is very weak. Ultimately both scattering processes have similar strength [5].

To evaluate $\rho_{\mathbf{k}_1\sigma_1(E_f)}$, one can consider the scattering process to be confined in a box of volume V_0, giving neutron wave functions

$$\Psi(\mathbf{r},\sigma) = \frac{1}{\sqrt{V_0}}e^{i\mathbf{k}\cdot\mathbf{r}}|\sigma\rangle. \tag{1.37}$$

The box approximation induces a periodic boundary condition also on the wave vectors which are restricted to discrete values $k = n(2\pi/L)$, where L is the size of the box in one specific direction. These wave vectors will form a lattice in reciprocal space with volume $(2\pi)^3/V_0$ per point, hence a density in reciprocal space of $g(\mathbf{k}) = V_0/(2\pi)^3$. The density of final states can then be written as:

$$\rho_{\mathbf{k}_1\sigma_1}(E_f)dE = 4\pi k^2 g(\mathbf{k})dk \;\Rightarrow\; \rho_{\mathbf{k}_1\sigma_1}(E_f) = \frac{V_0}{2\pi^2}\frac{m_n}{\hbar^2}k. \tag{1.38}$$

The conservation of energy in the scattering process can be introduced in the differential scattering cross section as a *delta* function $\delta(E_{\lambda_1} - E_{\lambda_0} - \hbar\omega)$, indicating with $\hbar\omega$ the energy exchanged by the neutron in the interaction. The incoming neutron flux can be expressed as a function of the incoming neutron wave vector as $\Phi_{in} = \frac{v}{V_0} = \frac{\hbar k_0}{V_0 m}$. Substituting the various terms in Equation 1.35, the partial differential scattering cross-section can be written as

$$\frac{d^2\sigma}{d\Omega dE_f} = V_0^2\frac{k_1}{k_0}\left(\frac{m_n}{2\pi\hbar^2}\right)^2\sum_{\lambda_0}p_{\lambda_0}\sum_{\lambda_1}|\langle\mathbf{1}|V(\mathbf{r})|\mathbf{0}\rangle|^2\,\delta(E_{\lambda_1} - E_{\lambda_0} - \hbar\omega). \tag{1.39}$$

The evaluation of $|\langle\mathbf{1}|V(\mathbf{r})|\mathbf{0}\rangle|^2$ is done considering that the spin and angular momentum parts of the neutron wave function are separated from the spatial part (Equation 1.37. In this case, one can explicitly write $|\langle\mathbf{k}_1\sigma_1\lambda_1|V(\mathbf{r})|\mathbf{k}_0\sigma_0\lambda_0\rangle|^2$, and

22

consider the potential affecting only the spatial part of the wavefunction:

$$
\begin{aligned}
\langle \mathbf{k}_1 | V(\mathbf{r}) | \mathbf{k}_0 \rangle &= \frac{1}{V_0} \int e^{-i\mathbf{k}_1 \cdot \mathbf{r}} V(\mathbf{r}) e^{i\mathbf{k}_0 \cdot \mathbf{r}} d^3 \mathbf{r} \\
&= \frac{1}{V_0} \int V(\mathbf{r}) e^{i\mathbf{Q} \cdot \mathbf{r}} d^3 \mathbf{r} \\
&= \frac{1}{V_0} V(\mathbf{Q}),
\end{aligned}
\tag{1.40}
$$

where $V(\mathbf{Q})$ indicate the Fourier transform of the interaction potential. Substituting this result in Equation 1.39 we obtain the master equation for the partial differential cross-section

$$
\frac{d^2\sigma}{d\Omega dE_f} = \frac{k_1}{k_0} \left(\frac{m_n}{2\pi\hbar^2} \right)^2 \sum_{\lambda_0} p_{\lambda_0} \sum_{\lambda_1} |\langle \sigma_1 \lambda_1 | V(\mathbf{Q}) | \sigma_0 \lambda_0 \rangle|^2 \, \delta(E_{\lambda_1} - E_{\lambda_0} - \hbar\omega). \tag{1.41}
$$

One can simplify this equation for the case of elastic scattering of a set of bound nuclei that was previously discussed. In the case in which the nuclei are rigidly bound, scattering processes will not affect their state, hence the interaction potential will not act on λ_1 and λ_0, which are going to be equal $\lambda_1 = \lambda_0$. This identity implies that the sum over the initial states in Equation 1.41 will disappear, and the sum over the final states will contain only the term where $\lambda_1 = \lambda_0$. Moreover, considering only elastic scattering, where there is no change in the neutron energy, the master equation can be written as:

$$
\frac{d\sigma}{d\Omega} = \left(\frac{m_n}{2\pi\hbar^2} \right)^2 |\langle \sigma_1 | V(\mathbf{Q}) | \sigma_0 \rangle|^2. \tag{1.42}
$$

Fermi pseudopotential

Up to now, no specifics on the interaction potential $V(\mathbf{r})$ have been given, and for nuclear interactions, no complete description exists for it. What is known is that the potential has to describe a short range interaction producing isotropic scattering from bound nuclei. The scattering can also be described with the single parameter b, the scattering length, modulating the amplitude of the scattered neutron waves (Section 1.2.3). According to these characteristics, the simplest one-parameter potential for a short range interaction is

$$
V_N(\mathbf{r}) = a\delta(\mathbf{r}). \tag{1.43}
$$

The general parameter a can be linked to the scattering length b by simply solving the integral in Equation 1.40 and substituting the result in Equation 1.42, yielding $a = b2\pi\hbar^2/m_n$, and the potential:

$$V_N(\mathbf{r}) = \frac{2\pi\hbar^2}{m_n}b\delta(\mathbf{r}). \tag{1.44}$$

This is the Fermi pseudopotential, and it represents an approximation to the correct potential for nuclear interactions. In fact, the derivation of the parameter a of the pseudopotential is valid only at large distances from the nucleus, where a first order perturbation theory is applicable. At the same time, it is not valid near the nucleus where $V_N(\mathbf{R})$ is large.

1.2.8 Magnetic Neutron Scattering

Neutrons interact with nuclei in matter also magnetically, thanks to their dipole moment which couples to the microscopic electromagnetic filed generated by unpaired electrons and magnetic nuclei in the samples. In contrast with nuclear forces, electromagnetic interactions have a longer range but are also much weaker, still allowing us to interpret the scattering interaction as a small perturbation of the incoming neutron wave function.

Given the long range of the interaction, to study magnetic neutron scattering is necessary to consider an accurate form of the magnetic interaction potential

$$V_M(\mathbf{r}) = -\boldsymbol{\mu}_n \cdot \mathbf{B}(\mathbf{r}), \tag{1.45}$$

where $\boldsymbol{\mu}_n$ is the neutron dipole moment in the flux density $\mathbf{B}(\mathbf{r})$. The flux density in a medium is the result of the sum of two major components: one coming from the intrinsic spin of the electrons $\mathbf{B}_S(\mathbf{r})$, and one coming from the motion of the electrons generating electronic currents $\mathbf{B}_L(\mathbf{r})$.

Considering the standard form of the flux density for a magnetic dipole moment [82], the spin contribution of a single electron is

$$\mathbf{B}_S(\mathbf{r}) = -2\mu_B \frac{\mu_0}{4\pi} \nabla \times \left(\frac{\boldsymbol{\sigma} \times \mathbf{r}}{r^3} \right), \tag{1.46}$$

where $\mathbf{s}$ is the spin of the electron, μ_B is the Bohr magneton. The orbital contribution to the flux density, hence the contribution given by the electrons non-relativistic movement, can be written as:

$$\mathbf{B}_L(\mathbf{r}) = -2\mu_B \frac{\mu_0}{4\pi} \frac{1}{\hbar} \frac{\mathbf{p} \times \mathbf{r}}{r^3}. \tag{1.47}$$

Considering that the magnetic moment of the neutron can be expressed as a function of its spin as $\boldsymbol{\mu}_n = -2\gamma\mu_N\boldsymbol{\sigma}_n$, where μ_N is the nuclear magneton and $\gamma = 1.913$. The magnetic interaction potential can be written as:

$$V_M(\mathbf{r}) = 2\gamma\mu_N\boldsymbol{\sigma}_n \cdot (\mathbf{B}_S(\mathbf{r}) + \mathbf{B}_L(\mathbf{r})). \tag{1.48}$$

Let us now consider a system with many electrons and evaluate the contribution of the j-th electron and the form of the potential V_M in its Fourier transform. Considering the j-th electron to be in a position $\mathbf{r}_j$, with spin $\mathbf{s}_j$, the spin dependent flux density becomes:

$$\begin{aligned}
\mathbf{B}_S(\mathbf{r})_j &= -2\mu_B\frac{\mu_0}{4\pi}\int \nabla \times \left(\frac{\boldsymbol{\sigma}_j \times \mathbf{R}}{R^3}\right) e^{i\mathbf{Q}\cdot\mathbf{r}}d^3\mathbf{r} \\
&= -2\mu_B\mu_0(\hat{\boldsymbol{Q}} \times (\boldsymbol{\sigma}_j \times \hat{\boldsymbol{Q}}))e^{i\mathbf{Q}\cdot\mathbf{r}_j},
\end{aligned} \tag{1.49}$$

where $\mathbf{R} = \mathbf{r} - \mathbf{r}_j$, and $\hat{\boldsymbol{Q}}$ is the unit vector identifying the direction of the momentum transfer vector $\mathbf{Q}$. The orbital contribution can be written as

$$\begin{aligned}
\mathbf{B}_L(\mathbf{r}) &= -2\mu_B\frac{\mu_0}{4\pi}\frac{1}{\hbar}\int \frac{\mathbf{p}_j \times \mathbf{R}}{R^3}e^{i\mathbf{Q}\cdot\mathbf{r}}d^3\mathbf{r} \\
&= -2\mu_B\frac{\mu_0}{4\pi}\frac{1}{\hbar Q}(\mathbf{p}_j \times \hat{\boldsymbol{Q}})e^{i\mathbf{Q}\cdot\mathbf{r}_j}.
\end{aligned} \tag{1.50}$$

The two terms combined give the expression for the Fourier transform of the magnetic interaction potential of a set of electrons:

$$V_M(\mathbf{Q}) = -4\mu_0\mu_B\mu_N\boldsymbol{\sigma}_n\sum_j\left(\hat{\boldsymbol{Q}} \times (\boldsymbol{\sigma}_j \times \hat{\boldsymbol{Q}}) + \frac{1}{\hbar Q}(\mathbf{p}_j \times \hat{\boldsymbol{Q}})\right)e^{i\mathbf{Q}\cdot\mathbf{r}_j}. \tag{1.51}$$

The interaction potential in real space can be written in terms of the magnetisation of the material $\mathbf{M}(\mathbf{r}) = \mathbf{M}_S(\mathbf{r}) + \mathbf{M}_L(\mathbf{r})$. From a physical point of view, the magnetisation related to the electrons spin $\mathbf{M}_S(\mathbf{r})$ identifies the spin density in the material. The magnetisation relative to the electron current $\mathbf{M}_L(\mathbf{r})$ has a less intuitive meaning. It can be interpreted as the density of angular momentum of the electrons travelling in bound orbits around the nuclei. In reciprocal space, the interaction potential is a function of the Fourier transform of the magnetisation $M(\mathbf{Q})$ and can be written as:
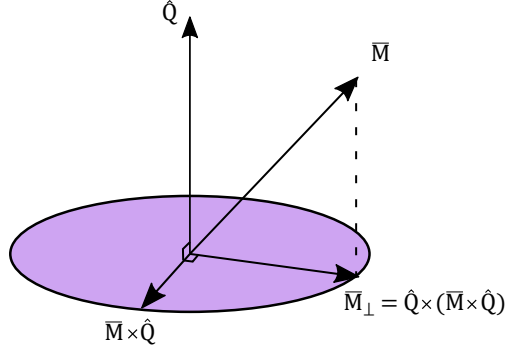
Figure 1.9: Relative orientation of the vectors $\hat{Q}$, $\mathbf{M}$, and $\mathbf{M}_\perp$, adapted from [5].

$$V_M(\mathbf{Q}) = 2\gamma\mu_0\mu_N\boldsymbol{\sigma}_n\mathbf{M}_\perp(\mathbf{Q}), \tag{1.52}$$

where

$$\mathbf{M}_\perp = \hat{Q} \times (\mathbf{M}(\mathbf{Q}) \times \hat{Q}) = \mathbf{M} - (\mathbf{M} \cdot \hat{Q})\hat{Q}. \tag{1.53}$$

This formulation indicates that magnetic scattering is sensitive only to the component of the magnetisation that lies perpendicular to the direction of the momentum transfer $\mathbf{Q}$, as shown in Figure 1.9, leaving the longitudinal component inaccessible in scattering experiments. This property is a direct consequence of Maxwell's equation $\nabla \cdot \mathbf{B}(\mathbf{r}) = 0$. This can be seen considering the Fourier component of the flux density

$$\mathbf{B}(\mathbf{r}) = \mathbf{B}(\mathbf{Q})e^{i\mathbf{Q}\cdot\mathbf{r}} \tag{1.54}$$

$$\nabla\mathbf{B}(\mathbf{r}) = -i\mathbf{Q} \cdot \mathbf{B}(\mathbf{Q})e^{i\mathbf{Q}\cdot\mathbf{r}} = 0 \tag{1.55}$$

imposing $\mathbf{Q} \cdot \mathbf{B}(\mathbf{Q}) = 0$, hence the component of the flux density along the direction of the momentum transfer vector is zero. Neutron scattering is only sensitive to the variations of flux density perpendicular to $\mathbf{Q}$.

Ultimately, one can write the elastic magnetic cross section as

$$\frac{d\sigma}{d\Omega} = \left(\frac{\gamma r_0}{2\mu_B}\right)^2 |\langle\mathbf{M}_\perp(\mathbf{Q})\rangle|^2, \tag{1.56}$$

where $r_0 = \mu_0 e/(4\pi m_e)$ can be obtained from the multiplication of the various terms in front of the summation of Equation 1.51 and $\gamma = 1.913$. With Equation 1.56 it is possible to relate the scattered intensity to the Fourier transform of

the magnetisation of the material.

Most magnetic neutron scattering experiments operate under the assumption to be in the dipole approximation [5], under which the orbital contribution to the magnetic scattering is ignored. Since only the contribution of the unpaired electrons is considered, under this condition, it is possible to link the measured magnetic cross sections to the microscopic magnetism of the material. To do so it is necessary to consider the magnetic moment of single site in the unit cell, that can be written as

$$\boldsymbol{\mu}_{ld} = \sum_{\mathbf{k}} \mathbf{m}_{\mathbf{q},d} e^{i\mathbf{k}\cdot\mathbf{l}}, \tag{1.57}$$

expressing the magnetic moment of the dth site in the lth unit cell, where $\mathbf{m}_{\mathbf{k},d}$ are the Fourier transforms of the moment's components on site d. In this notation, $\mathbf{k}$ identifies the propagation vector of the magnetic structure in reciprocal space. Summing the contribution of the different magnetic moments in the unit cell, it is possible to write the magnetic structure factor

$$\mathbf{F}_M(\mathbf{Q}) = \frac{\gamma r_0}{2\mu_B} \sum_{d} \boldsymbol{\mu}_d f_d(Q) e^{-W_d} e^{i\mathbf{k}\cdot\mathbf{d}}, \tag{1.58}$$

which corresponds to the Fourier transform of the magnetisation of the unit cell. f_d indicates the form factor of each magnetic moment in the unit cell, and e^{-W_d} is the Debye-Waller factor, indicating the damping of the scattered intensity given by thermal atomic vibrations. Through Equation 1.58, it is possible to rewrite the cross section for elastic magnetic scattering as

$$\frac{d\sigma}{d\Omega} = N_m \frac{(2\pi)^3}{v_m} \sum_{\mathbf{G}_m} |\mathbf{F}_\perp(\mathbf{Q})|^2 \delta(\mathbf{Q} - \mathbf{G}_m), \tag{1.59}$$

where N_m is the number of magnetic unit cells in the material and v_m is their volume. The same arguments for the perpendicular components of the magnetisation being the ones contributing to the scattering used for Equation 1.53 apply also in the case of the single unit cell, then $\mathbf{F}_\perp = \hat{\boldsymbol{Q}} \times (\mathbf{F}(\mathbf{Q}) \times \hat{\boldsymbol{Q}})$. $\mathbf{G}_m$ is the reciprocal lattice vector of the magnetic lattice, and the summation is carried over all the atoms in the magnetic unit cell.

1.2.9 Modulated magnetic structures

A magnetic structure exhibiting a large periodicity compared to the crystal periodicity is identified as a modulated magnetic structure. These structures can be identified by the wave vector $\mathbf{k}$, defining their spatial periodicity,
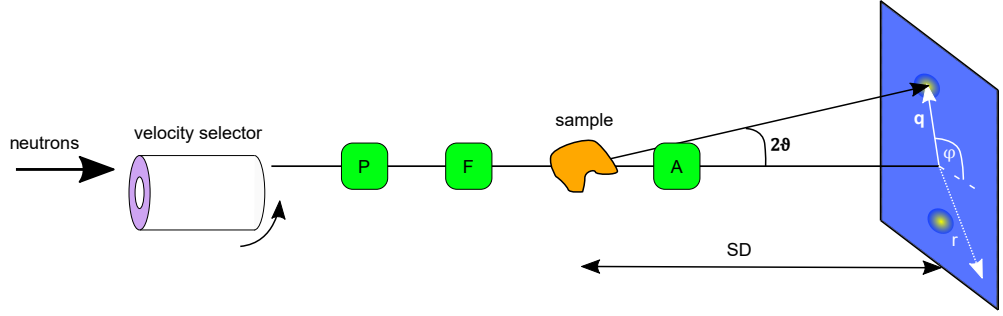
Figure 1.10: SANS general experimental setup adapted from [6]. The boxes indicated with P, F, and A correspond to polarizer, flipper and analyzer, respectively. SD indicates the distance between the sample and the detector. r identifies the position on the detector plane, while q is the momentum transfer vector. The scattering angle is indicated with 2θ, while the angle defining the position of the Bragg spots on the detector is indicated by ϕ.

$$\mathbf{k} = \mathbf{k}_0 + \delta, \tag{1.60}$$

where δ is a small variation on the initial wave vector $\mathbf{k}_0$ identifying the underlying ferromagnetic (FM, $\mathbf{k}_0 = 0$) or antiferromagnetic (AF) structure. The long modulation of these structures produces Bragg scattering at $\mathbf{Q} = \boldsymbol{\tau} \pm \mathbf{k}$, hence the scattering from a modulated magnetic structure appears as two satellites at position $\pm\mathbf{k}$ from each nuclear Bragg spots in position $\boldsymbol{\tau}$.

The modulation can affect the amplitude of the magnetic moments, their orientation, or both. Of particular interest for this work is the helimagnetic structure that can be described by the magnetic moment distribution $\boldsymbol{\mu}_l$

$$\boldsymbol{\mu}_l = \mu(cos(\mathbf{k} \cdot \mathbf{l} + \phi) \cdot \hat{\mathbf{u}}_k + sin(\mathbf{k} \cdot \mathbf{l} + \phi) \cdot \hat{\mathbf{v}}_k]. \tag{1.61}$$

In this case, the magnetic moment amplitude is not varying, while its orientation is rotating in the plane identified by the unit vectors $(\hat{\mathbf{u}}_k, \hat{\mathbf{v}}_k)$ from one unit cell to the other with a phase ϕ.

The helical is a non-collinear spin structure, such as the conical and cycloidal, and several different mechanisms can be at its origin [3]. For the purpose of this work we focus on the non-collinear modulated magnetic structures induced by the Dzyaloshinskii-Moriya interaction in non-centrosymmetric materials.

1.3   Small angle neutron scattering

Among the different neutron scattering techniques, small angle neutron scattering (SANS) has the peculiarity of being able to resolve scattering happening at such small angles that other techniques can not distinguish from the transmitted neutron beam. This is possible thanks to the very long distances at which the detector is usually placed in SANS experiments. From Bragg's law, Equation 1.22, it is evident that for a given wavelength, the smaller the angle of the diffracted beam, the bigger the structure probed. SANS is optimised to study magnetic and non-magnetic structures from a few to hundreds of nm, hence very small momentum transfer vectors [6]. SANS is also a powerful tool for the study of disordered structures such as liquid and glasses. These structures would produce diffuse scattering on the detector plane [5], in contrast with well defined diffraction spots characterising ordered structures such as the skyrmion lattice. In this work we focus our attention on the Bragg scattering originating from the skyrmion lattice, as the contribution of the diffuse scattering was very small and its characterisation was outside the scope of this thesis.

The typical setup of a SANS instrument is illustrated in Figure 1.10. The neutrons are collected at the reactor (or spallation) source and are directed towards the experimental area via neutron guides. SANS instruments are usually placed on neutron guides delivering cold neutrons moderated to have an energy in the range of $\sim 0.1 - 10$ meV. The neutron wavelength can be modified at the instrument by means of velocity selectors or choppers, selecting a wavelength in the range of $\sim 3 - 30$Åwith a resolution that varies between 1% to 30%, according to the method used. Before the sample position, the neutron beam is collimated with a set of apertures and passes through polarisers and spin flippers, used optionally to modify the characteristics of the beam. Neutrons are delivered to the sample area where several sample environments can be mounted, such as high pressures, low temperatures and high magnetic field devices. Typically, the size of the irradiated area is in the order of $\sim 1 - 10$ mm. After the sample position, one or more two-dimensional position sensitive detectors are placed on rails in an evacuated tank where they can be moved closer and further away from the sample position, in a range of $\sim 1 - 40$ m. Moreover, an optional analyser can be used to select neutrons with one specific spin polarization, allowing polarization analysis. On the detectors, Bragg spots appear at position $|\mathbf{q}| = (4\pi/\lambda)sin\theta$, where the scattering angle $\theta < 5° - 10°$. With such small scattering angles, the momentum transfer modulus q, can be written as a function of its position on the detector r, and the

sample-detector distance SD:

$$q = \frac{2\pi r}{\lambda} SD. \tag{1.62}$$

Using this expression, it is possible to adjust the wavelength and the sample-detector distance to optimise the scattering conditions on the detector, considering that r has to vary withing the angular and spatial range of physically covered by the detectors, usually $\sim 0.04 - 0.7$m.

1.3.1 Imaging skyrmions with SANS

As mentioned before, the SANS technique is optimised for the study of nano-sized structures, hence it is a powerful tool for the study of the aforementioned modulated magnetic structure, which can have a periodicity up to several thousand Å. In B20 materials, the magnetic ground state at zero applied magnetic field consists of a multi-domain of single-$\mathbf{q}$ helices with propagation vectors, in the case of Cu_2OSeO_3, pinned along the main crystallographic directions [100], [010], and [001]. Upon the application of a sufficiently large magnetic field, the system passes into a single domain conical state, with a propagation vector parallel to the applied field. In the skyrmion pocket area of the $\boldsymbol{H}$-$\boldsymbol{T}$ phase diagram, the skyrmion lattice can be described as a superposition of three helices tilting away from each other by 120°, with the same magnitude and phase of the propagation vectors, which lie on a plane perpendicular to the applied field. In Section 1.2.9, it was shown how modulated structures, with propagation vectors $\mathbf{k}$, produce magnetic satellites that decorate the nuclear Bragg peaks, giving scattering at $Q = \boldsymbol{\tau} \pm \mathbf{k}$. In SANS, one looks at the scattering at low angles happening around $\boldsymbol{\tau} = (0,0,0)$, hence the momentum transfer vector coincides with the propagation vector of the modulated structure, and we identify it as $\mathbf{q}$.

As shown before in Section 1.2.8, the only components of the magnetisation visible in a SANS experiments are the ones that are perpendicular to the momentum transfer vector, in this case, to the propagation vector of the modulated structures. In Figure 1.11 are presented the scattering patterns relative to the magnetic states of Cu_2OSeO_3, except the paramagnetic and field polarised states that produce no scattering. Passing from the geometry in which the magnetic field is parallel to the neutron beam to the field perpendicular to it, let different helix domains diffract on the detector plane. The conical phase produces two horizontal diffraction spots only when the field is perpendicular to the neutron beam. When the field is parallel to the neutron beam, also the propagation vector of the conical phase is parallel
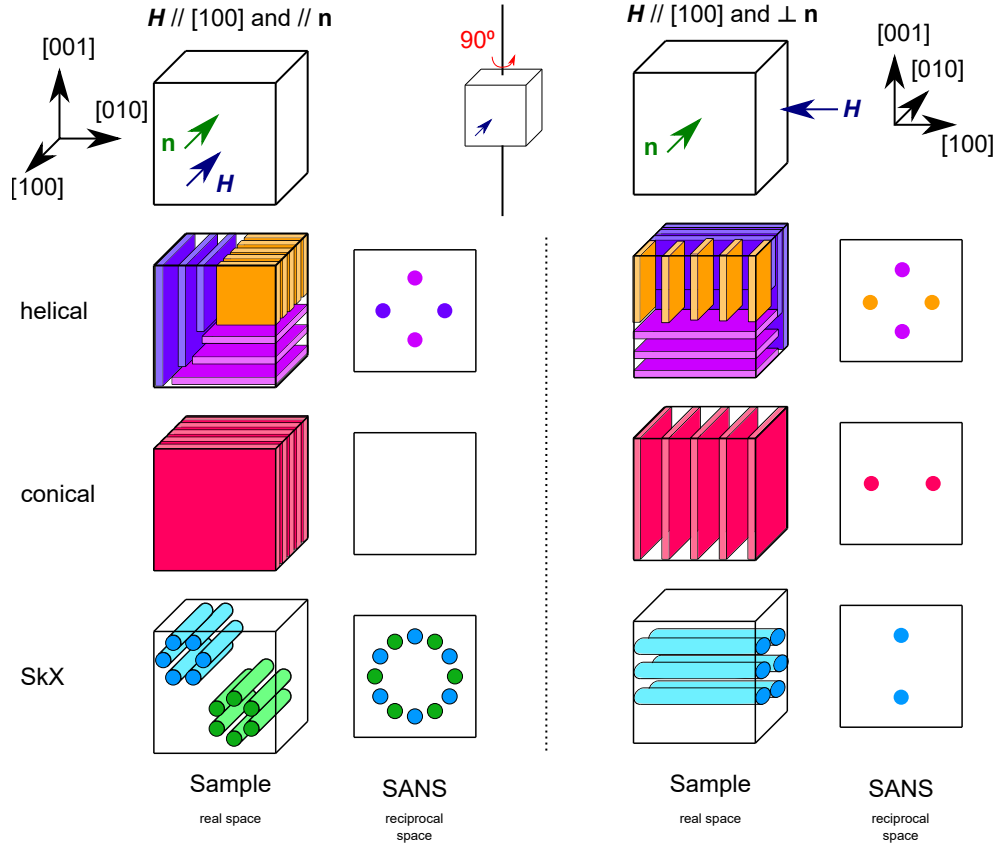
Figure 1.11: Illustration of the helical, conical and SkX phases in a generic skyrmion material and their corresponding SANS patterns for the two geometries $\mathbf{H} \parallel \mathbf{n}$, and $\mathbf{H} \perp \mathbf{n}$. The external magnetic field in both cases is always applied along the [100] crystallographic direction. This figure was adapted from [42].
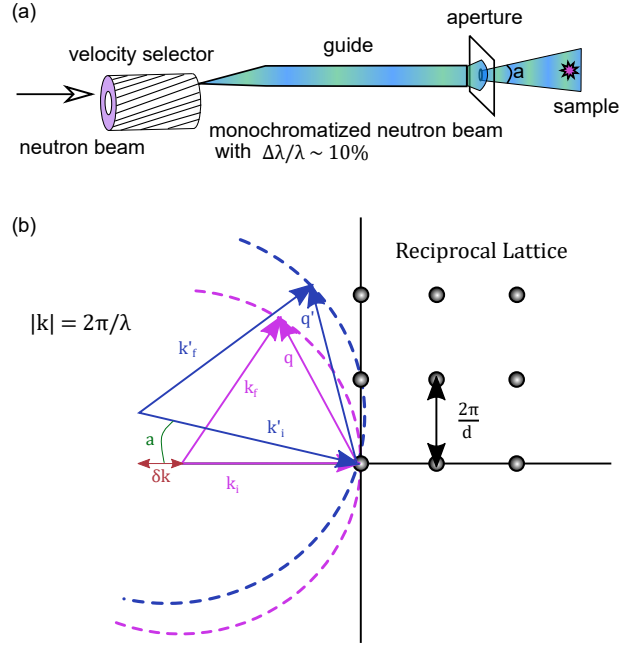
Figure 1.12: (a): the neutron beam with an angular spread a is monochromatised by the velocity selector with a fractional spread of the wavelength of 10%, hence a spread in the wavevector k. (b): Ewald's sphere representation of the scattering considering the angular spread and the wavelength fractional spread of the incoming neutron beam. The reciprocal lattice points in this representation are of a perfect structure, hence point-like.

to the to the neutrons, hence no variations of the magnetisation lie on the plane perpendicular to the propagation vector, letting the conical state appear uniform in this geometry. The periodicity of the conical state is revealed in the $\mathbf{H}_\perp$ geometry, as shown in Figure 1.11. The SkX hexagonal arrangement corresponds, in reciprocal space, to the typical 6-fold scattering pattern. The skyrmions elongate like tubes in the material, and in the $\mathbf{H}_\perp$ geometry it is possible to study the distance between skyrmion tubes planes.

1.3.2 Extracting Correlation Lengths from SANS patterns

A perfectly collimated neutron beam, with no spread in wavelength, hitting a lattice with a perfect spacing and no defects would produce scattering only under the very specific condition dictated by Bragg's law in Equation 1.22. However, in real experiments, the incoming neutron beam will be characterised by a finite angular spread a and a specific wavelength spread $\delta\lambda/\lambda$. At the same time, the structure analysed might not be perfectly ordered, showing a variation in its characteristic
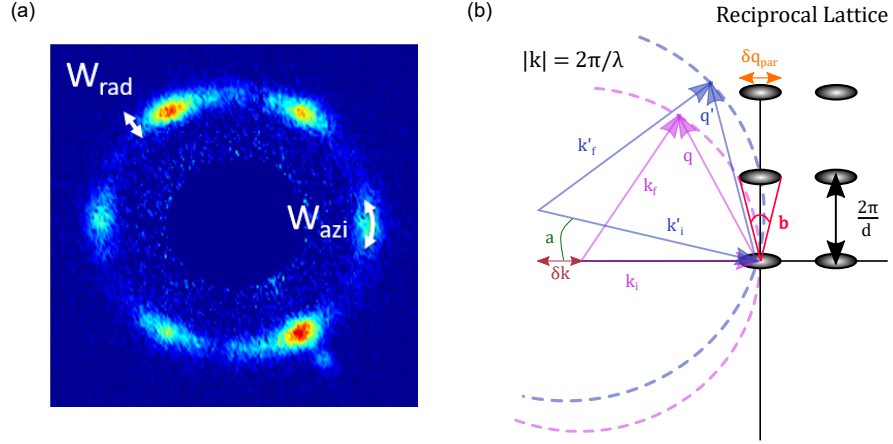
Figure 1.13: The intrinsic disorder of the structure studied is encoded in the size of the Bragg spots. In panel (a) is shown a SANS scattering pattern of the skyrmion lattice taken in Zn substituted Cu_2OSeO_3. The radial width of the spots indicated as W_{rad} is related to the d-spacing spread of the lattice $\delta d/d$. The azimuthal width W_{azi} of the spots is related to the rotational disorder of the skyrmion lattice t. In panel (b) is depicted the imperfect Ewald's sphere of Figure 1.12 interacting with an imperfect structure. The reciprocal space points of the structure are elongated along the direction of the incoming neutron beam and their width in the direction of the neutron beam is δq_{par}. b is the angular size of δq_{par}.

spacing $\delta d/d$, a mosaic spread s, and a rotational disorder t. The imperfections in both the incoming neutron beam and the structure studied allow a more relaxed Bragg condition, where the scattering is satisfied for a certain spread of angles. In these conditions, the Bragg spots in reciprocal space will have a width in each of the three dimensions of the reciprocal space that relate to $\delta d/d$, b, and t, which are the parameters describing the intrinsic disorder of the structure studied, as previously reported in [7, 83, 84].

The azimuthal width of the Bragg spots W_{azi}, shown in Figure 1.13(a), is affected by the angular spread of the neutron beam and contains information on the rotational disorder of the studied structure

$$W_{azi} = \sqrt{t^2 + a^2}. \tag{1.63}$$

W_{azi} is measured considering the angle of the Bragg spot on the detector panel ϕ. The value of a can be obtained by measuring the azimuthal width of the transmitted beam by centring the analysis on the selected Bragg spot, to take into account any anisotropy of a related to ϕ.

The radial width of the Bragg spots W_{rad}, shown in Figure 1.13(a) has a

33

more complicated description since it is caused by several effects at the same time

$$W_{rad} = \sqrt{\frac{a^2c^2 + a^2b^2 + 4b^2c^2}{a^2 + b^2 + c^2}}, \tag{1.64}$$

where b indicates the angular spread of the Bragg spots in the direction of the neutron beam, and c is

$$c = \theta\sqrt{\left(\frac{\delta\lambda}{\lambda}\right)^2 + \left(\frac{\delta d}{d}\right)^2}. \tag{1.65}$$

In the measurements presented in this work it is possible to assume that $b >> a$, $b >> c$. In this case,

$$W_{rad} = \sqrt{a^2 + 4c^2} = \sqrt{a^2 + 4\theta^2\left(\left(\frac{\delta\lambda}{\lambda}\right)^2 + \left(\frac{\delta d}{d}\right)^2\right)}. \tag{1.66}$$

The size of the Bragg spots in the direction parallel to the incoming neutron beam δq_{par} is related to the mosaicity of the structure. This dimension of the Bragg spots is not projected onto the detector plane and can be written as

$$W_{par} = \sqrt{a^2 + b^2 + c^2}. \tag{1.67}$$

In the same conditions considered for W_{rad} where $b >> a, c$, then

$$W_{par} = b, \tag{1.68}$$

which can be directly measured performing rocking scans. A rocking scan consists in rotating the sample around its vertical axis while being in the Bragg condition. In the case of the skyrmion lattice a rocking scan is performed rotating about the vertical axis both the sample and the applied magnetic field, as the skyrmion tubes elongate along the direction of $\boldsymbol{H}$, as shown in Figure 1.14(a). The diffracted intensity of skyrmion lattice is collected as a function of the rotating, 'rocking', angle ω, and then plotted for selected Bragg spots as shown in Figure 1.14(a). The finite width of the rocking curve derives from the convolution of the instrument resolution, and the mosaicity of the skyrmion lattice. For a given instrumental resolution, a high mosaicity of the skyrmion lattice corresponds to a wide profile of its rocking curve, as shown in Figure 1.14(c). The correspondence between the rocking curve profile and the characteristcs of the skyrmion lattice is treated in detail in Chapter 4.

Performing a rocking scan, corresponds to rotating the reciprocal lattice in and out of the Ewald's sphere, in reciprocal space. Recording the scattered intensity

as a function of the rotating angle produces rocking curves, which width is equal to b.

Equations 1.63, 1.66 and 1.68 can be solved for t, $\frac{\delta d}{d}$ and b to collect information about the intrinsic disorder of the lattice. Particular attention is needed in the process of converting these quantities in real space correlation lengths since the conversion implies doing a Fourier transform which result depends on the shape of the peaks (Gaussian, Lorentzian).

Here we explicitly show how to convert b into the longitudinal correlation length of the structure L_{par} since it is the simplest case, and the most relevant to the work presented in this manuscript. To measure b, one has to measure the rocking curve of the selected Bragg spot, Equation 1.68. The rocking curve will have a Gaussian or Lorentzian profile. In the Gaussian case, $b = \sigma_q$, where b is the angular size of the Bragg spot's width in the direction of the incoming neutron beam, Figure 1.13(b). b relates to δq_{par} as

$$ b = \frac{\delta q_{par}}{q} \quad \Rightarrow \quad \delta q_{par} = bq, \tag{1.69} $$

where q is the magnitude of the momentum transfer vector, and δq_{par} has to be multiplied by $\pi/180$ to have the dimensions of Å^{-1}. To transform δq_{par} in a correlation length in real space, one has to consider the Fourier transform of the rocking curve, which in this case is still a Gaussian with a $\sigma_r = 1/\sigma_q$, describing the correlation length x_0 of the lattice in the direction parallel to the neutron beam. If the rocking curve has a Lorentzian profile $L(q)$, then the angular size of the Bragg spot b will be equal to the FWHM$_q$ of the Lorentzian. Equation 1.69 is still valid, however, one has to consider the Fourier transform (FT) of the Lorentzian function describing the profile of the rocking curve:

$$ L(q) = \frac{1}{2\pi} \frac{\delta q}{(q - q_0)^2 - (\frac{\delta q}{2})^2} \quad \Rightarrow \quad FT[L(q)](x) = e^{-\delta q \pi |x|}, \tag{1.70} $$

considering the FWHM of $FT[L(q)](x)$, the correlation length in real space in this case is given by $x_0 = 2ln(2)/(\delta q \pi)$.
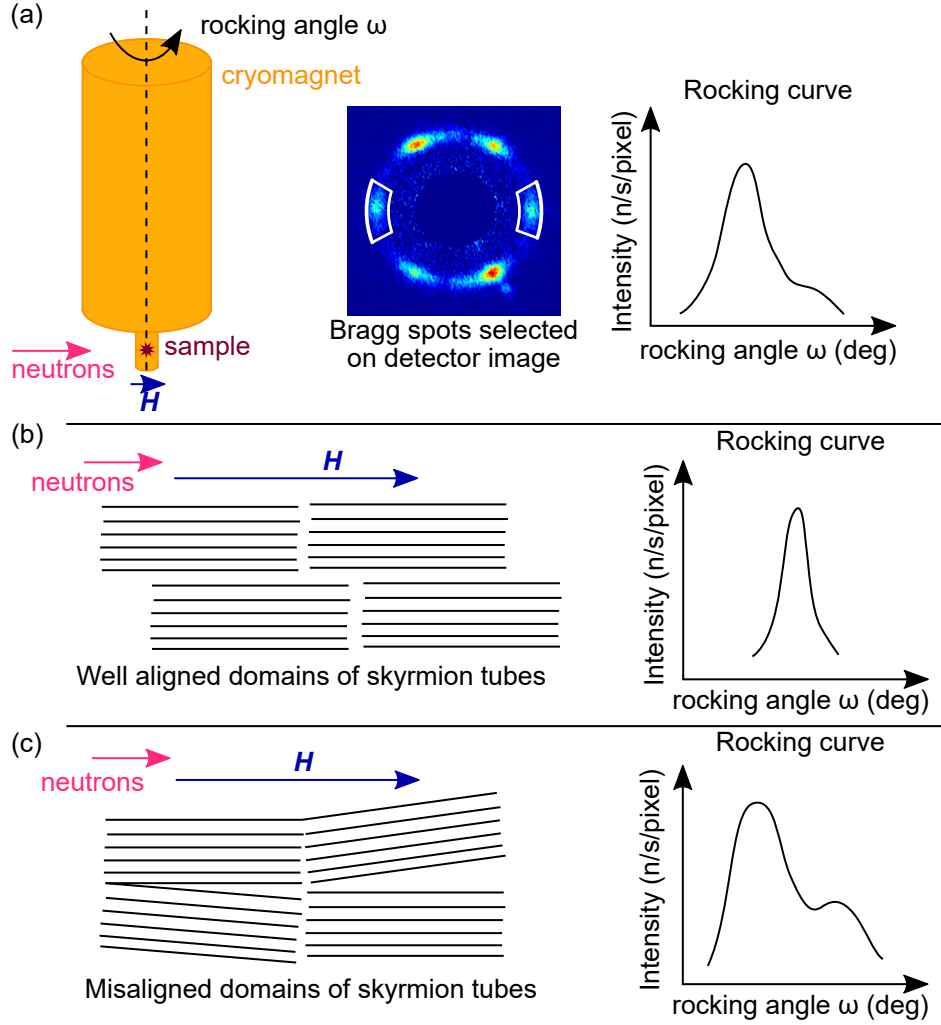
Figure 1.14: (a): illustration of a rocking scan of the skyrmion lattice. The sample and the cryomagnet are rotated together along the vertical axis. On the detector the typical six-fold scattering pattern is recorded as a function of the rocking angle ω, and the intensity of a pair of selected Bragg spots is plotted as a function of ω. (b): illustration of a group of skyrmion domains well aligned between each other and along the direction of the magnetic field. The corresponding rocking curve profile is sharp. (c): a group of skyrmion domains presenting a higher mosaicity, with skyrmion tubes bending, a domains tilting away from the direction of the applied field. The corresponding rocking curve profile is wider than in case (b).

Chapter 2

Samples and their characterisations methods

This chapter contains an overview of sample preparation methods and characterisation via magnetometry measurements and Laue diffraction. Marta Crisanti performed the Laue diffraction measurements. The samples used for this thesis work were prepared by Dr A. Štefančič, Sam Holt, and Prof. Geetha Balakrishnan at the University of Warwick [71]. Dr Max Birch performed the AC susceptibility measurements at the Diamond Light Source in Didcot (UK) [49].

The stabilisation of magnetic skyrmions was first predicted for non-centro-symmetric materials [12], and they were later observed for the first time in the B20 material MnSi [16]. MnSi belongs to the $P2_13$ spacegroup, where the lack of inversion symmetry allows the presence of the Dzyaloshinskii-Moriya interaction, which favours the presence of long wavelength helimagnetic structures, as discussed in Section 1.1.2. Shortly after, skyrmions were observed in other B20 materials such as $Fe_{1-x}Co_xSi$ [17], FeGe [22], and MnGe [85]. In these materials, Bloch-type skyrmions are stabilised by thermal fluctuations in a narrow region of the $\boldsymbol{H}$-$\boldsymbol{T}$ phase diagram below the ordering temperature, and their magnetic ground state consists of helimagnetic structures.

2.1 Cu_2OSeO_3

Among the non-centrosymmetric bulk skyrmion hosts, the only insulating material is Cu_2OSeO_3. This material crystallises in the same spacegroup as MnSi, and it shows a similar magnetic phase diagram, indicating that it shares with MnSi the same hierarchy of interactions defining its magnetic structures [2, 86–88]. Although crystallising in the cubic chiral $P2_13$ spacegroup like MnSi, the atomic coordination of Cu_2OSeO_3 is very different. The structure hosts two different Cu^{2+}, one situated either at the centre of a trigonal bipyramid of oxygen ligands or at the centre of a square pyramid base [2, 89, 90], as shown in Figure 2.1(a). These two sites have spins antiparallel to each other. The building block of the magnetic structure consists of a tetrahedron formed by four Cu^{2+} ions ferrimagnetically [89, 90] arranged, as the two different Cu sites are in ratio 3:1 in the magnetic tetrahedron, as shown in Figure 2.1(b).

Cu_2OSeO_3 is also multiferroic [2], hence its magnetisation can be manipulated via the application of an electric field, and magnetic fields can influence its electric polarisation. These characteristics make this system perfect for studying the manipulation of the skyrmion state via electric fields. In particular, it has been shown that the skyrmion state can be rotated via the application of electric fields [91, 92]. Moreover, the application of electric fields can enhance or suppress the size of the skyrmion pocket, allowing a topological phase switching between the conical and skyrmion magnetic states [53, 56–58], as previously mentioned in Section 1.1.3. The possibility of manipulating the skyrmion state, and moving the skyrmions with the application of electric fields, provides a way to avoid energy loss through Joule heating effects associated with electric currents [93].
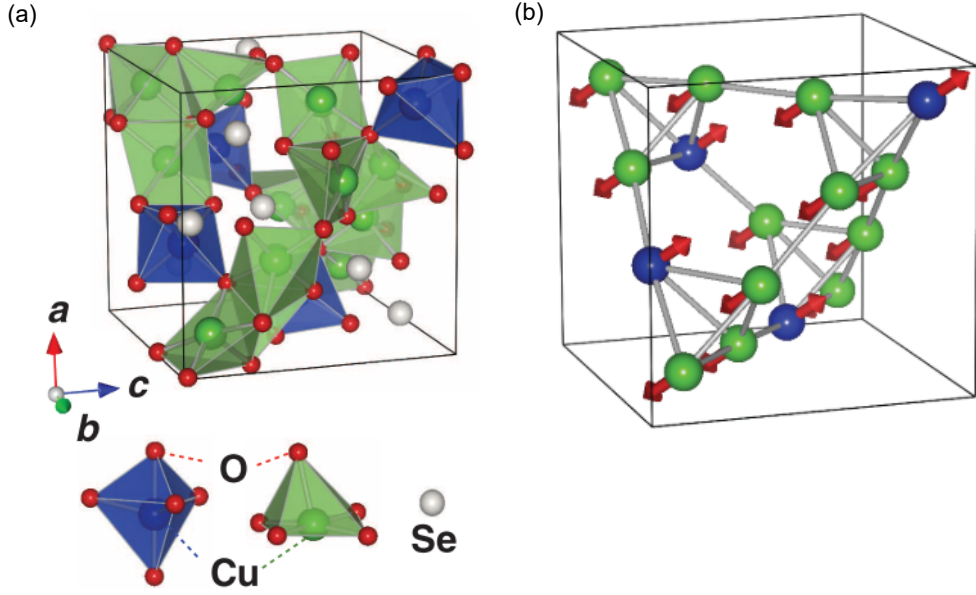
Figure 2.1: (a) crystal structure of Cu_2OSeO_3, the different coloured area identifies different Cu^{2+} sites. (b) magnetic structure. Adapted from [2, 90].

Zn and Ni substituted Cu_2OSeO_3

As previously introduced in Section 1.1.3, controlled chemical substitution is a possible avenue for the manipulation of the skyrmion pocket size and position, and allow the study of the interplay between the underlying crystal structure and the magnetic states of a material. In Cu_2OSeO_3, two different chemical substitutions have been reported, one where Cu ions were substituted with Zn [71, 72, 94], and another with Ni [70, 72]. In the case of the Zn substitution, a split of the skyrmion pocket along the temperature axis of the H-T phase diagram was firstly observed in polycrystalline samples [94]. Moreover, the separation between the two independent skyrmion pockets was observed to increase with increasing Zn concentration. However, the same effect was not observed in single crystal samples [71], where the increasing Zn content is associated with a shift towards lower temperatures of the whole magnetic phase diagram, also observed in polycrystalline samples in [72]. On the other hand, the substitution with Ni ions was studied in polycrystalline samples and evidence of an enhancement of the temperature range of the skyrmion pocket was found [70, 72]. In both cases, the changes in the magnetic properties were linked to a distortion of the bipyramidal and square pyramidal structures inducing an increase of the DMI strength.

In this thesis, Zn and Ni substituted Cu_2OSeO_3 single crystals, and pristine
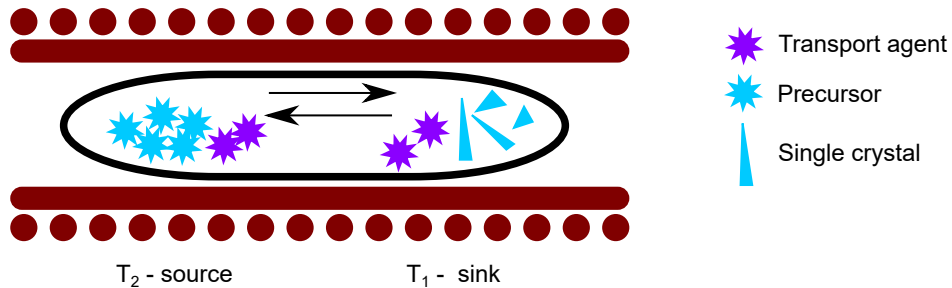
Figure 2.2: Schematic of the chemical vapour transport method.

Cu_2OSeO_3 single crystals were studied with small angle neutron scattering and neutron diffraction.

2.2 Chemical Vapour Transport

Chemical vapour transport (CVT) is a technique for the growth of single crystals and it consists of the volatilising of a solid in the presence of a reactant, a gaseous transport agent, that deposits the solid elsewhere where crystals are formed. A schematic of the experimental apparatus is depicted in Figure 2.2. The transport agent moves the solid within a sealed ampule in a two-zone furnace. The transport is governed by convection and diffusion processes. Favouring convection over diffusion can lead to the growth of larger single crystals however, these crystals would be more prone to host defects and inhomogeneities. Several parameters need to be optimised for each crystal growth, such as temperature, transport direction, mass transport rate, transport agent.

Initial precursors of Zn substituted, Ni substituted (with different nominal content of dopant) and pristine Cu_2OSeO_3 were placed into silica tubes and sealed under vacuum. The precursors were heated to 920 K at a 3.5 K/hr rate and held for 96 hours. The heating procedure was followed by water quench cooling, resulting in polycrystalline samples with different chemical substitution levels. From these polycrystalline powder samples, single crystals were prepared using the CVT. 2.5g of powder samples were mixed with 1.5 to 2.0 mg/cm^3 of transport agent, TeCl$_4$, and then sealed in silica tubes under vacuum that were then put in a two zone furnace with a source temperature of 913 K and a sink temperature of 823 K. The mixture was left in the furnace for four weeks.
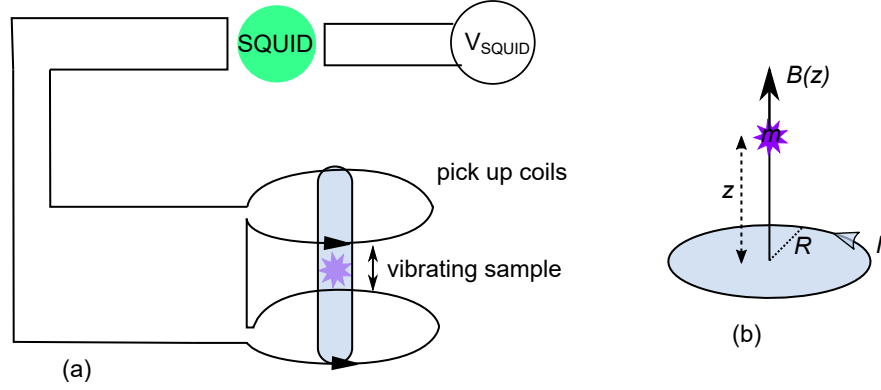
Figure 2.3: (a) schematic of a SQUID-VSM. (b) Schematic of a field generated by a flowing current I in point z, where a sample with magnetic moment m is.

2.3   Magnetometry

Magnetometry measurements were performed using a commercial SQUID vibrating sample magnetometer (VSM), a Quantum Design MPMS3. In a VSM, the DC magnetisation of the sample is determined via the flux change induced by the oscillation of the sample within two pick-up coils. When a magnetic moment m placed at a height z along the axis of a coil of radius R through which is passed a current I induces a flux $\Phi(z)$ on the coil, that can be expressed following the Biot-Savart law [82] as:

$$\Phi(z) = \frac{B(z)}{I} \cdot m = \frac{m\,\mu_0}{2} \frac{R^2}{(z^2 + R^2)^{3/2}} = G(z)m. \tag{2.1}$$

In a VSM, the sample's position changes with time as the sample is vibrating inside the constant field provided. This induces a voltage and in the pick up coils

$$V = \frac{d\Phi(z)}{dt} = \frac{dG(z)}{dz} m \frac{dz}{dt}. \tag{2.2}$$

In a SQUID-VSM, the signal of the VSM is measured with a superconducting quantum interference device (SQUID), which measures the magnetic flux passing through its cross sectional area, proportional to a voltage V_{SQUID}. Ultimately one measures this voltage as the sample is moved through the pick-up coils. A simplistic schematic of the experimental apparatus is depicted in Figure 2.3. The software of the machine extracts from the voltage the magnetisation of the sample that can be measured as a function of temperature and applied magnetic field [95].

It is also possible to measure the susceptibility, which is the rate of change of magnetisation with applied field (dM/dH). This can be done without moving the

sample, but oscillating the applied field. In this mode, the time dependent sample moment induces currents in a coil, that are picked up as a voltage, proportional to $\frac{dM}{dt}$ locked into the drive frequency. These measurements are highly sensitive to small changes in the magnetisation. The time dependent magnetisation in AC mode for a driving field of amplitude H_{AC}, and an oscillating frequency ω can be written as

$$\frac{dM}{dt}(H) = \frac{dM}{dH}H_{AC}sin(\omega t), \tag{2.3}$$

where $dM/dH = \chi$, the magnetic susceptibility. The lock in amplifier can provide an in and out-of-phase measurement of the susceptibility, relative to drive frequency. In this context, the susceptibility can be written as a complex number $\chi = \sqrt{\chi'^2 + \chi''^2}$, where χ' corresponds to the in-phase component, and the real part of the susceptibiliy. The imaginary part of the susceptibility χ'' corresponds to the out-of-phase component and it is related to dissipative processes in the samples such as magnetic relaxations, domain wall motions and phase transitions.

2.4   Laue Diffraction

Neutron Laue diffraction measurements performed on OrientExpress in ILL, which setup is shown in Figure 2.4, were used to align the single crystal samples for other diffraction experiments. This technique employs a white neutron beam, passing through a hole between two CCD sensor panels and two neutron scintillator panels, for then reaching the sample. The back-scattered neutrons hit the scintillators, where they interact producing photons that are collected by the CCD sensors. Since the beam is polychromatic, the Bragg condition is satisfied for every set of lattice planes, producing scattering at different angles. In this way, a reciprocal space picture of the crystal is obtained. For samples of high crystalline quality, individual reflections can be identified and indexed, allowing the determination of the sample orientation in the laboratory reference frame.

OrientExpress side view

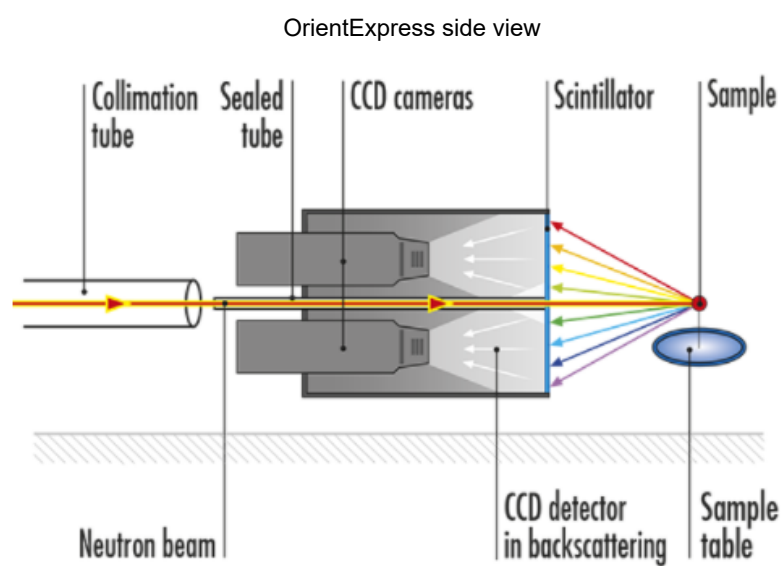Figure 2.4: Schematic of the single crystal neutron Laue instrument OrientExpress. Figure reproduced from [96].

Chapter 3

Skyrmions under pressure

The contents of this chapter are published in [65]. The experiment was performed by N. Reynolds, and Dr J. White. The data analysis was done by M. Crisanti, who also worked on the article's publishing process with Dr J. White. The figures were adapted or reproduced from [65].

Several methods exist for the manipulation of the parameter space over which the skyrmion state is stable in chiral magnets. The size of the skyrmion pocket can be substantially enhanced both by reducing the samples' dimensions into thin films [22] and via supercooling through the skyrmion pocket, creating a metastable state [42, 49, 53, 56, 75]. However, in the first case, the generality of the H-T phase diagram typical of bulk chiral magnets is lost, and its characteristics become highly sensitive to the method and quality of the sample preparation process. In the second case, such metastable skyrmion states display a lifetime that decreases for increasing temperature and a population that depends on the cooling rate [49, 75]. Controlled chemical substitution also constitutes a viable approach for the tuning of the position and size of the skyrmion phase [70–72], however, the theoretical treatment of such disordered systems represent an ongoing challenge.

Applied pressure, both uniaxial and quasi-hydrostatic, has also proven to be an effective tuning parameter for the magnetic ordering of chiral magnets [45, 59, 60, 97, 98]. In the itinerant chiral magnet MnSi, T_C is suppressed by the application of hydrostatic pressure and tends to 0 at a specific critical point near 14.6 kbar [99, 100]. In the form of uniaxial compressive strain, uniaxial pressure was also shown to affect characteristics of MnSi phase diagram. Specifically, according to the relative direction of the strain σ and the applied magnetic field $\mathbf{H}$, the skyrmion phase stability was either enhanced ($\sigma \perp \mathbf{H}$) or suppressed ($\sigma \parallel \mathbf{H}$)

3.1 Effects of quasi-hydrostatic and uniaxial pressure on Cu_2OSeO_3

The application of quasi-hydrostatic pressure on the archetypal skyrmion host Cu_2OSeO_3 has been shown to monotonically increase the ordering temperature T_C [62–64]. In particular, a significant increase in the skyrmion pocket's size was observed with AC susceptibility in [64]. The temperature extent of the skyrmion region of stability was substantially enhanced by the application of pressure, passing from a $\Delta T_{Skx} \approx 3$ K at ambient pressure to an extension of $\Delta T_{Skx} \approx 26$ K at 2.3 GPa. The enlargement of the skyrmion pocket with increasing hydrostatic pressure was tailored to an increase in the effective anisotropy K, measured by the increase of $\mathbf{H}_{c1}$. The application of uniaxial pressure on Cu_2OSeO_3 resulted in a similar behaviour to what was shown for MnSi, where the relative direction of the applied strain σ and the magnetic field $\mathbf{H}$ determining an enhancement or suppression of the skyrmion region of stability [61]. Contrary to the hydrostatic pressure case, in Cu_2OSeO_3, no increase in T_C was observed up to a strain of 1.01 kbar.

The uniaxial pressure results in both MnSi and Cu_2OSeO_3 suggest that just moderate compressive strains, in the order of kbars, can be responsible for a considerable increase of the skyrmion pocket size. For this reason, it is not clear whether the remarkable enhancement of the skyrmion pocket reported in Ref. [64] in Cu_2OSeO_3 was an effect induced by the hydrostatic pressure, or it rose from inhomogeneity in the applied pressure, leading to an expansion of the skyrmion pocket caused by an unwanted uniaxial pressure component.

With this in mind, we turn our attention to the study of the magnetic ordering of Cu_2OSeO_3 under hydrostatic pressure applied using He as a pressure transmitting medium (PTM), which has been shown to provide better hydrostatic conditions than other commonly used PTMs.

3.2   Experimental setup

Typical hydrostatic pressure experiments on chiral magnets use liquid pressure transmitting medium (PTM) in which the sample is immersed. However, these liquid PTMs, such as Daphne-7373 oil, Fluorinert, or methanol-ethanol mixture, do not perform as well as gaseous PTMs such as He, Ne, and N_2 in neutron scattering experiments at cryogenic temperatures [101]. Gaseous PTMs display lower shear strengths when they solidify at low T, compared to the liquid PTMs, providing higher hydrostaticity but lower maximum pressures.

For this experiment, a 91 mg single crystal of Cu_2OSeO_3 was mounted on an Al pillar in a Ti-Zr gas pressure cell. The pressure cell was inserted in an orange cryostat, where the magnetic field was provided by an electromagnet. The sample was aligned with orthogonal $[0\bar{1}1]$-$[100]$ axes lying in the horizontal plane and with the $[110]$ axis vertical. The magnetic field was applied along the $[0\bar{1}1]$ direction for the whole experiment. The measurements were performed with the applied field either parallel or perpendicular to the neutron wave vector. In this way it was possible to study all the magnetic phases of interest in the sample. The Bragg condition at the detector position is satisfied only by structures whose wave vector lies perpendicular to the one of the neutron beam. For this reason, when $H \parallel \mathbf{k}_i$, it was possible to study the typical six-fold scattering pattern of the skyrmion state, while no contribution to the scattering was given by the conical state. When $H \perp \mathbf{k}_i$ instead, it was possible to measure the scattering from the conical phase. The helical state produced scattering in both geometries: the $[010]$ and $[001]$ domains were visible in the perpendicular geometry, while the $[100]$ was visible in the parallel geometry [86, 90–92], as shown in Figure 3.1(a) and Figure 3.1(c), respectively.
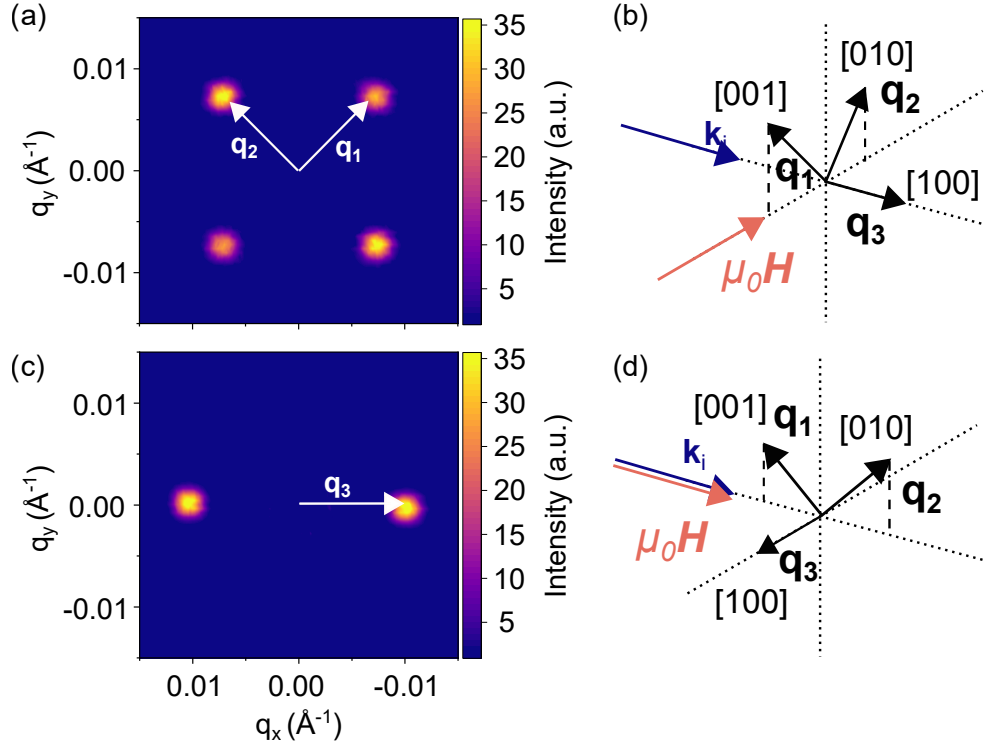
Figure 3.1: Schematic of the two experimental geometries employed during the SANS measurements. In panel (a) is reported the diffraction pattern at zero applied magnetic field in the $\boldsymbol{H}_\perp$ geometry at $T = 30$ K, as illustrated in panel (b), where the applied magnetic field direction is perpendicular to the neutron's wave vector $\mathbf{k}_i$. In this geometry, the measurements are sensitive to two helical domains, which propagation vector is perpendicular to the incoming neutron beam and identified as q_1 and q_2. In panel (c) is shown the scattering pattern corresponding to the $\boldsymbol{H}_\parallel$ geometry, illustrated in panel (d). In this case, the field direction is parallel to the incoming neutron beam, and only one helical domain is in the Bragg condition at the detector position, identified as q_3.

The SANS experiment was performed on the D33 beamline at ILL. The neutron beam was collimated for 12.8 m before the sample, and the neutrons were collected 12.8 m after the sample. A wavelength of $\lambda_n = 5$ Å with a FWHM fractional spread of $\Delta\lambda/\lambda = 10\%$ was selected for the experiment. Rocking curve measurements were collected in both geometries, rotating the cryomagnet-field-sample ensemble, recording the scattered neutron intensity at each angle with an average exposition of 30 s per angle.
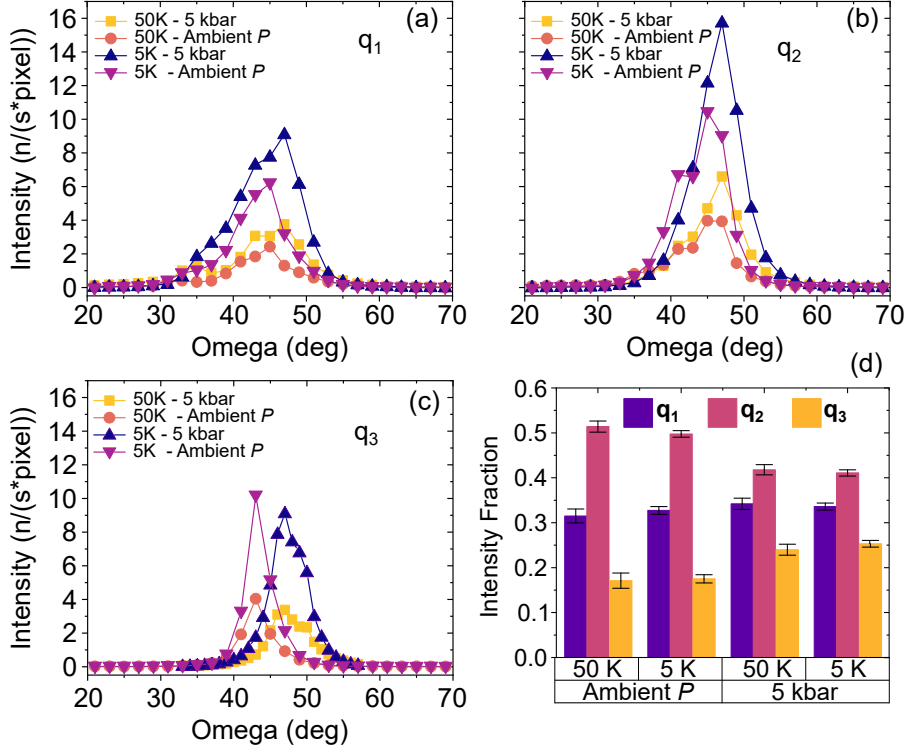
Figure 3.2: **(a), (b), (c)**: Omega rocking scans of the three helical domains recorded at 5 K and 50 K in ambient pressure and 5 kbar of hydrostatic pressure applied. **(d)**: population fraction of each helical domain at both temperature and pressure conditions. The population fraction was determined from the integrated intensity of the rocking scans.

3.3 Results

3.3.1 Helical state population and hydrostaticity of the applied pressure

The characterisation began with a measurement of the magnetic state in zero applied magnetic field. Rocking scans in omega were performed by rotating the sample around its vertical axis in order to collect the full scattered intensity of the helical domains. The rocking curves are presented in Figure 3.2.

It can be noticed by inspection of panels (a), (b) and (c) of Figure 3.2 that, in both pressure conditions, the intensities of the rocking curves are not equal among the three helical domains, hence the population of the helical phase is not distributed equally among the domains. A more quantitative evaluation of this uneven distribution of the helical population is plotted in Figure 3.2(d), where we report the population fraction of the helical domains at 5 K and 50 K at both pressure condi-

	Ambient P		5 kbar	
	50 K	5 K	50 K	5 K
$\lvert q_1 \rvert$ (Å)	0.010480(7)	0.010240(7)	0.010410(6)	0.010190(6)
$\lvert q_2 \rvert$ (Å)	0.010500(7)	0.010260(7)	0.010440(6)	0.010160(6)
$\lvert q_3 \rvert$ (Å)	0.01047(2)	0.01022(1)	0.01040(1)	0.010160(9)

Table 3.1: Fitted values of $\lvert q_i \rvert$ at ambient pressure and in 5 kbar, at both $T = 5$ K and $T = 50$ K. At each P-T condition, the fitted values of $\lvert q_i \rvert$ of all the helical domains are the same within experimental uncertainty. The values have been obtained fitting the scattered intensity as a function of the momentum transfer $\mathbf{q}$.

tions. While the population fraction of the $\mathbf{q}_1$ domain remains almost unchanged with the application of pressure, the $\mathbf{q}_2$ domain appears to be overpopulated, occupying half of the sample volume at ambient pressure, mainly at the expense of the $\mathbf{q}_3$ domain. Under 5 kbar of hydrostatic pressure, the helical population is redistributed among the domains, lowering their disparity. Moreover, for the $\mathbf{q}_3$ domain, the application of pressure induced a shift in the centre of the peak of about $\approx 5°$, while no significant shift is observed for the other two helical domains. These observations indicate the presence of a uniaxial component in the applied pressure during the experiment.

Helical domains with different populations in Cu_2OSeO_3 at ambient pressure have been previously observed in Ref [61]. This effect might be attributed to residual directional stresses originating at the sample production stage or by the specific conditions of the experiment. As previously reported in [61], in Cu_2OSeO_3, uniaxial stress in the order of ≈ 0.1 kbar $\perp \mathbf{q}_i$ induced an increase of the $\mathbf{q}_i$ population of 500%, without changing the $\lvert q_i \rvert$ to a level of 0.1%. In our measurements, at ambient pressure, we observe a lower disparity among the populations of the three helical domains than was reported in [61]. Moreover, the modulation vector $\lvert q_i \rvert$ in each experimental condition was the same for all the domains within the experimental accuracy of 0.1%, as reported in Table 3.1. Considering these minor effects on the magnitude of the helical modulation vectors and on the population fraction disparity, we take 0.1 kbar as an upper-limit estimate for possible undesired uniaxial stress components in the experiment. In all directions, the propagation vectors had values close to 0.01 Å^{-1}, consistent with the value reported in the literature [2, 86, 91, 92].

We concluded that besides the slight modification of the distribution of internal residual stresses, the applied pressure was predominantly hydrostatic.
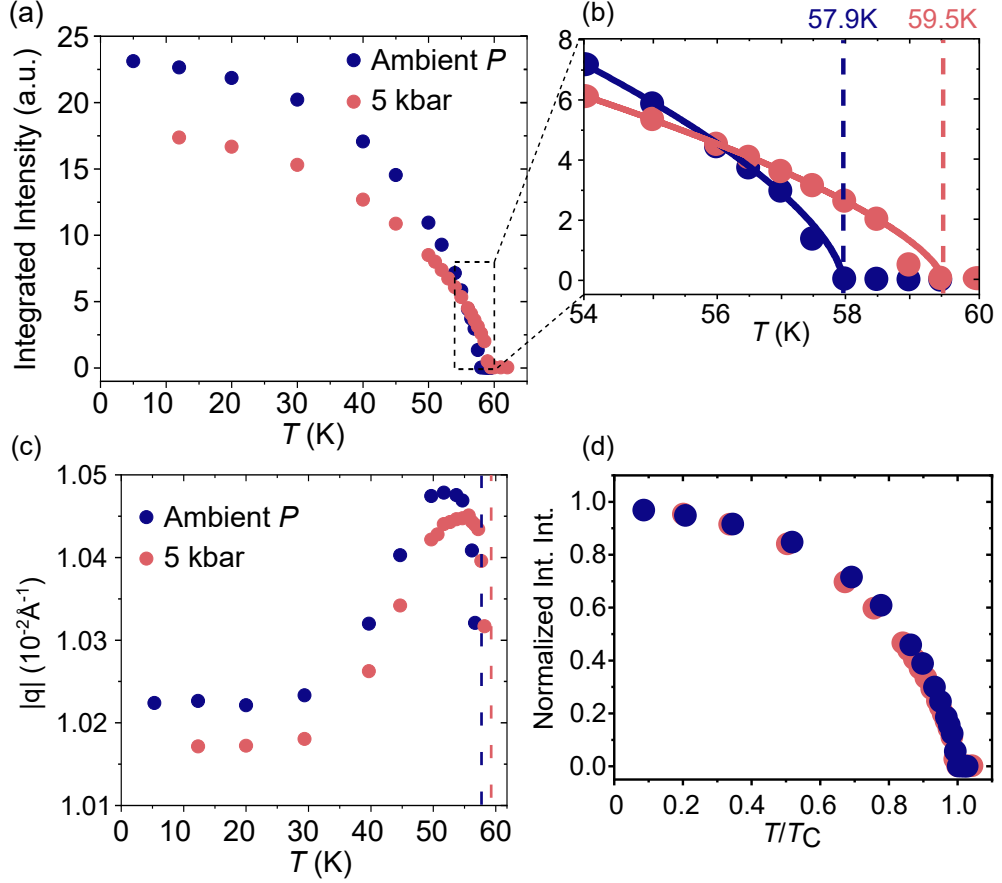
Figure 3.3: **(a)**: temperature dependence of the SANS integrated intensity from the two helical domains $\mathbf{q}_1$ and $\mathbf{q}_2$ visible in the $\mathbf{H} \perp$ geometry. The integrated intensity results from the average of $I\mathbf{q}_1$ and $I\mathbf{q}_2$ and is reported for both ambient pressure and 5 kbar. In panel **(b)** is shown in detail the high-T range where the data is fitted to the Curie-Weiss law to determine T_{C}. **(c)**: temperature dependence of the helical propagation vector value $|\mathbf{q}|$ at $\mathbf{H} = 0$ at both pressure conditions. **(d)**: SANS integrated intensity normalised by the estimated zero-T value versus T/T_C. The data presented here do not show any obvious consequences of the solidification of the He PTM, which happens at 39.6 K under 5 kbar.

3.3.2 Helical order and critical fields

We determined the value of the ordering temperature by analysing the integrated intensity of $\mathbf{q}_1$ and $\mathbf{q}_2$ averaged together, and shown in Figure 3.3(a). The reduced averaged intensity of the 5 kbar data in the low temperature region of Figure 3.3 is due to the population redistribution, which favours $\mathbf{q}_3$ at the expense of $\mathbf{q}_2$, as already discussed and shown in Figure 3.2(d).

Figure 3.3(b) is shown the detail of the plot near T_C. The data points in this range have been fitted to the Curie-Weiss law, with a critical exponent, to determine the value of the ordering temperature at both pressure conditions. T_C increases under pressure passing from T_C= 57.9(1) K at ambient pressure to T_C= 59.5(1) K under 5 kbar. The pressure dependent increase of T_C is $\partial T_C/\partial P = +0.32(1)$ K/kbar, in agreement with previously published measurements on bulk samples [62, 64, 102], which show a linear dependence between the ordering temperature and the applied pressure. In Figure 3.3(d), the integrated intensity was normalised to its expected value at zero-T and it is plotted as a function of $T/\ T_C$. Figure 3.3(d) shows that the application of pressure has a weak effect on the form of the T dependence of the integrated intensity .

The pressure and temperature dependence of the helical propagation vector's magnitude are shown in Figure 3.3(c), where $|q|$ was determined averaging $|q_1|$ and $|q_2|$. In both pressure conditions, $|\mathbf{q}|$ firstly increase near T_C, it then drops between 50 K and 30 K, to then plateau below 30 K, away from the effect of thermal fluctuations [16, 57]. Pressure induces a suppression of $\sim 0.5\%$ on the helical $|q|$ in the low T range.

These results can be interpreted from a mean field point of view, where $|q| \propto D/J$ and $T_C \propto J$ [36]. In this context, the increase of the ordering temperature indicates an increase of J, while the concomitant reduction of $|q|$ shows the weaker dependence on pressure of D compared to J.

In Figure 3.4 is shown the field dependence of the scattered intensity of the helical and conical domains measured at 5 K. These measurements have been performed in the $\boldsymbol{H} \perp$ geometry, where the Bragg reflections produced by the conical phase lie on the detector plane. At zero applied magnetic field, the total scattered intensity originates from the helical phase. By increasing the magnetic field, the helices turn into a single-$\mathbf{q}$ conical domain. The transition fields were determined by fitting the peaks found in the first magnetic field derivative of the SANS intensity and are presented in the graph. H_{C1} identifies the magnetic field at which the sample passes from the helical to the conical domains, and it is marked by a dash-dotted line. H_{C2} identifies the field at which the system passes from the conical state to a
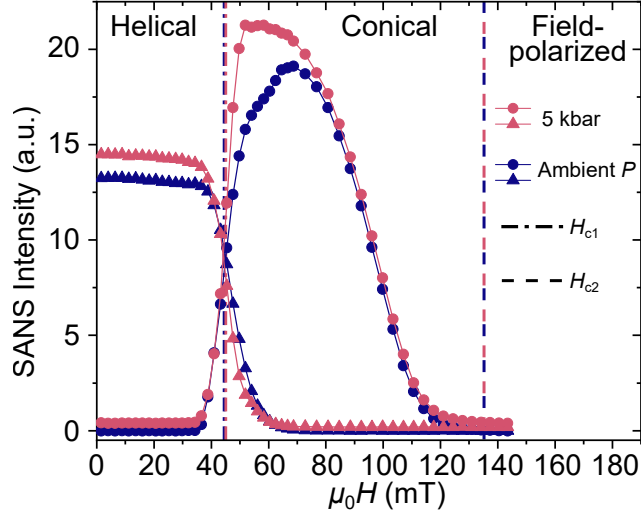
Figure 3.4: Field scans performed at $T = 5$ K of the SANS intensity of the helical state and conical state. The measurements were performed in the $\mathbf{H} \perp$ geometry in both pressure conditions. The helical state data correspond to the average of the intensities of $\mathbf{q}_1$ and $\mathbf{q}_2$ domains. The peaks in the first magnetic field derivative of the data were fitted to determine the values of the critical fields. H_{C1}, at the transition between helical and conical phases, is indicated by the dash-dotted lines. H_{C2}, at the transition between the conical and field-polarised states, is indicated by dashed lines.

uniformly magnetised state, and it is marked by a dashed line.

The application of pressure has a weak effect on both critical fields: H_{C2} at both pressure conditions stayed unchanged within uncertainty: $\mu_0 H_{C2}(\text{ambient} P) = 99.5(5)$ mT and $\mu_0 H_{C2}(5 \text{ kbar}) = 99.1(5)$ mT. $\mu_0 H_{C1}$ increases by $2.5\%(1.0)$ under pressure, passing from $\mu_0 H_{C1}(\text{ambient } P) = 44.6(3)$ mT to $\mu_0 H_{C1}(5 \text{ kbar}) = 45.7(3)$ mT.

3.3.3 Skyrmion phase stability under pressure

In Figure 3.5 is shown the pressure dependence of the skyrmion state's parameter space. Figures 3.5(a) and 3.5(c) show the SANS intensity field scans at different temperatures. From these data, we determined the upper and lower boundaries of the skyrmion pocket at both pressure conditions, identified by white circles in Figures 3.5(b) and 3.5(d). The skyrmion pocket appeared only slightly enlarged under 5 kbar of applied pressure, passing from a maximum extent at ambient pressure of $T_C(\text{ambient } P)$ - 2.5(5) K, to $T_C(5 \text{ kbar})$ - 3.0(5) K, and no other significant deformation of the skyrmion's parameter space was observed.

In Figure 3.6, we report the *in situ* measurements demonstrating in detail the
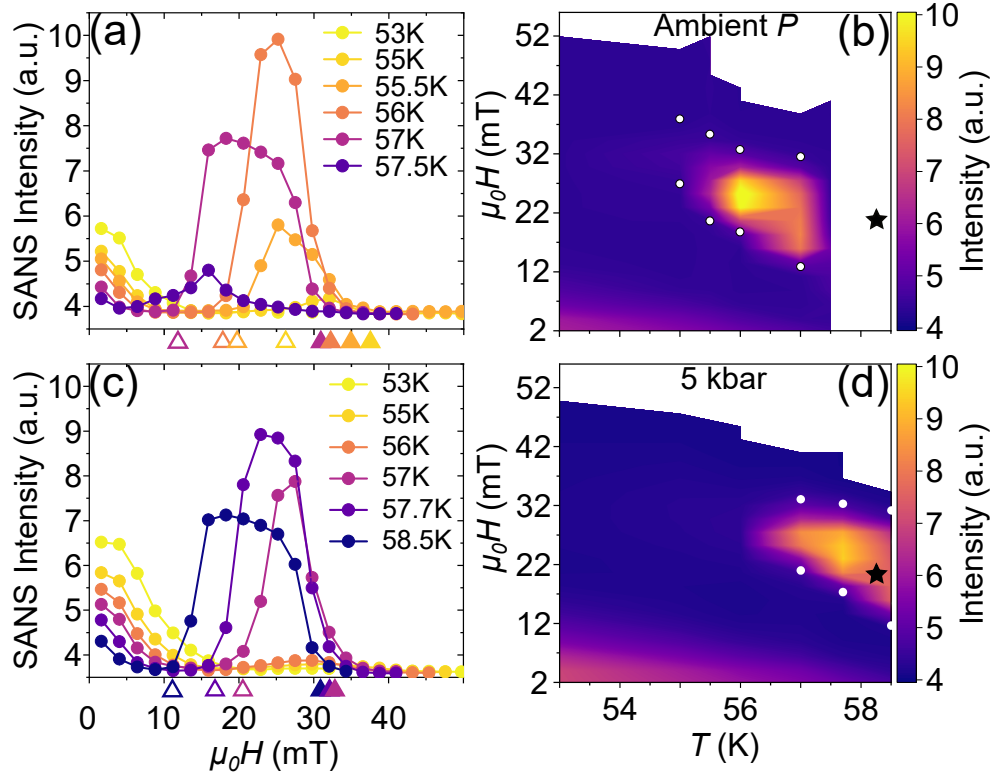
Figure 3.5: Panel (a) show the ambient pressure field scans of the SANS intensity used to draw the colour map of the skyrmion pocket in panel (b). The triangles on the field axis of panel (a) indicate the transition fields marking the edges of the skyrmion pocket (open = low field edge; filled = upper field edge) and are reported in panel (b) as white dots in the colour map. Panel (c) shows the field scans collected at 5 kbar and used in panel (d) to draw the phase diagram. The triangles and circles in panels (c) and (d) have the same meaning as the ones in panel (a) and (b). The colours of the triangles identify the temperature of the field scan to which they belong. The black star in the colour maps indicated the field and temperature conditions under which the data in Figure 3.7 were collected. The increased intensity observed in each panel at low temperatures and low field corresponds to the SANS intensity of the helical domain $\mathbf{q}_3$.
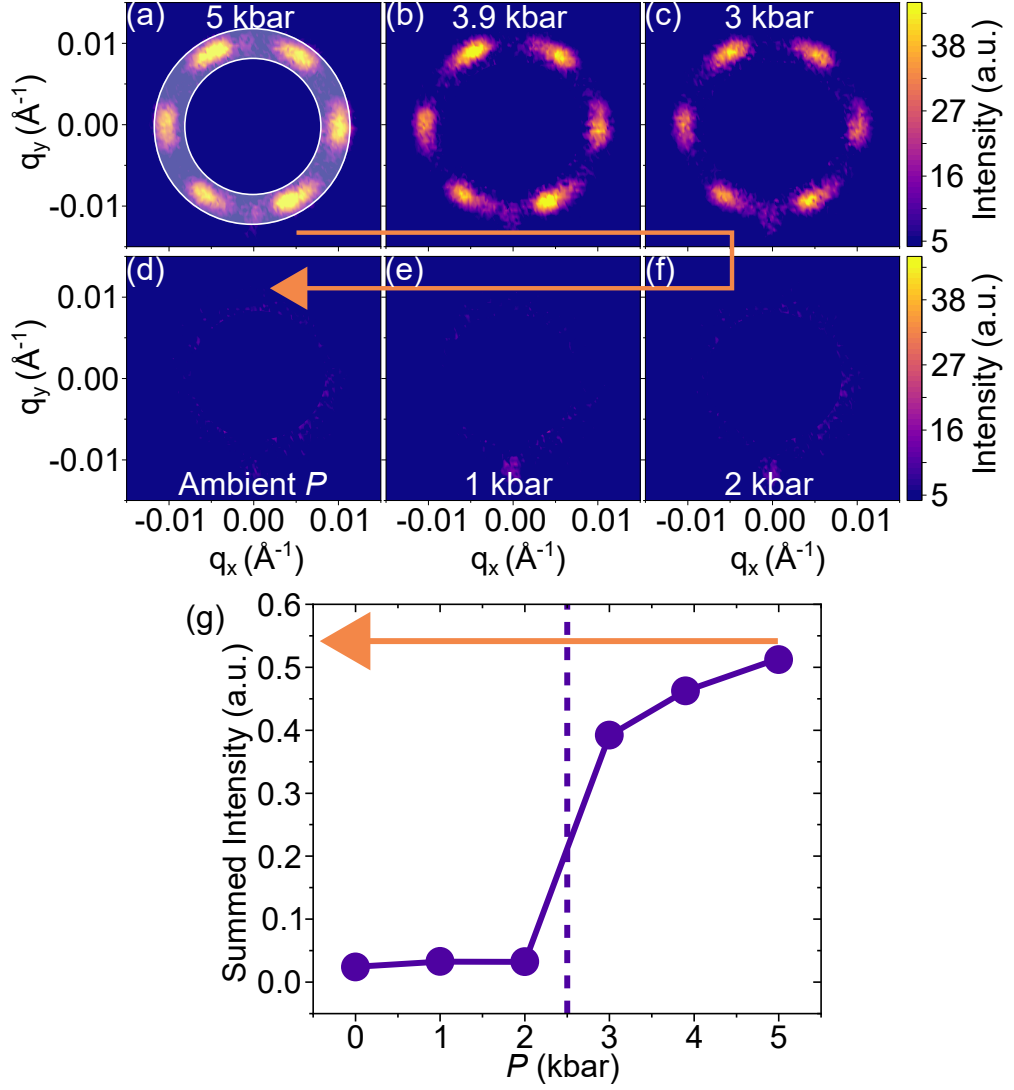
Figure 3.6: Panels (a) to (f) demonstrate the pressure-decreasing dependence of the SANS scattering patterns obtained at fixed $T = 58.25(10)$ K and $\mu_0 H = 21$ mT. The shaded area in (a) indicates the area of the detector over which the scattered intensity has been summed and is plotted versus the pressure value in panel (g). The scattering pattern in panels from (a) to (f) have been plotted with a fixed intensity scale. The orange arrows across all panels indicate the direction of pressure variation in the measurement.

pressure-driven transition between the skyrmion phase, present at 5 kbar of applied hydrostatic pressure at $T = 58.25(10)$ K and $\mu_0 H = 21$ mT, and the paramagnetic state at ambient pressure. The measurements were performed while slowly releasing the He gas pressure, avoiding possible temperature variations. For the set of measurements shown, we recorded no temperature variation larger than 10 mK. The scattered intensity from the skyrmion lattice decreases as temperature decreases and abruptly falls to 0 at $P_C = 2.5$ kbar, indicating a first order transition. Our results show how the skyrmion phase can be tuned by the exclusive application of hydrostatic pressure, effect that is explicitly shown in Figure 3.7. Figures 3.7(a) and 3.7(b) show the SANS scattering patterns collected at ambient pressure and at 5 kbar, respectively, each at $T = 56$ K and $\mu_0 H = 25$ mT. At these specific conditions, the skyrmion lattice loses stability under pressure, and its scattered intensity is significantly suppressed, as shown in Figure 3.7(b). The skyrmion state stability can also be enhanced by the application of pressure, as shown at $T = 58.5$ K and $\mu_0 H = 21$ mT. In this case, at ambient pressure, the sample lies in the uniformly magnetised state, while it is in the skyrmion state for $P = 5$ kbar.

Under applied pressure, the skyrmion lattice is characterised by a single domain, while we observe a multidomain lattice at ambient pressure. This change in the ordering of the skyrmion state could be linked to the modification of the internal strain equilibrium induced by the application of pressure, however, similar effects have already been observed in connection to the thermal and magnetic history of the sample [2, 91, 103, 104]. As the actual internal strain distribution is not known at both pressure conditions, we cannot draw conclusions on the possible coupling between the skyrmion lattice structure and the applied pressure.

3.4   Conclusions

The effects of quasi-hydrostatic pressure on the magnetic structure and phase diagram of Cu_2OSeO_3 with $H \parallel [0\bar{1}1]$ have been established. Under pressure, T_C increases by +2.8(2)%, the magnitude of the helical propagation vector $|q|$ decreases by -0.5(2)%. The critical field between the helical and conical phase increases by 2.5(1.0)%, while the critical field between the conical and paramagnetic phase remained unchanged within uncertainty.

According to mean field theory [36, 64], it is possible to link the change in these observable quantities to the strength of microscopic interactions as follows:
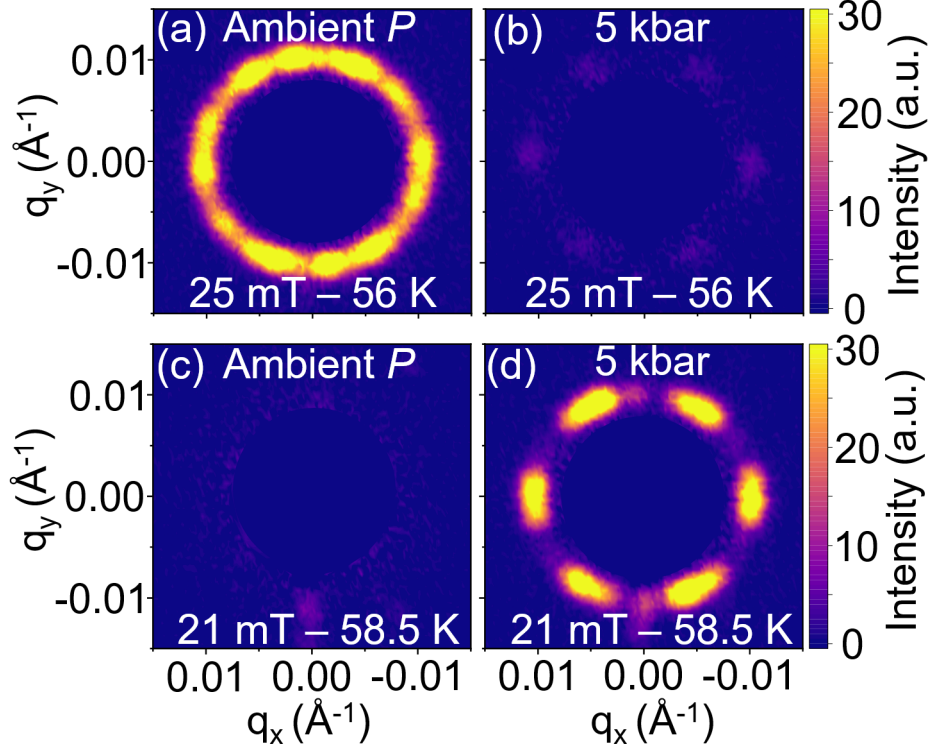
Figure 3.7: Illustration of the manipulation of the skyrmion stability with hydrostatic pressure in the $H \parallel \mathbf{k}_i$ geometry. In panels (a) and (b) are shown the SANS scattering patterns of the SkL at recorded at $T = 56$ K, $\mu_0 H = 25$ mT at ambient pressure and 5 kbar, respectively. In panels (c) and (d) are shown the SANS scattering patterns obtained at $T = 58.5$ K, $\mu_0 H = 21$ mT at ambient pressure and 5 kbar, respectively. The intensity scale has been fixed across all the panels to underline the differences in the scattered intensity in the different pressure conditions.

$$|q_h| \propto \frac{D}{J} \tag{3.1}$$

$$H_{C1} \propto K \tag{3.2}$$

$$H_{C2} \propto \frac{D^2}{J} \tag{3.3}$$

$$T_C \propto J \tag{3.4}$$

where J is the magnetic exchange interaction, D identifies the Dzyaloshinskii-Moriya interaction's strength, and K is the magnetic anisotropy. The application of quasi-hydrostatic pressure induced only minor changes in the structure of the phase diagram. The increase in $T_{\rm C}$ with the concomitant small suppression of $|q_h|$ indicates an increase in D of $+2.2(1)\%$, faster than the increase in J. The small enhancement of the size of the skyrmion pocket would be consistent with an increase of K, which has already been shown to be a parameter affecting the extent of the skyrmion phase stability [57, 64].

The variation in the critical fields and in $T_{\rm C}$ that we observe at 5 kbar can be contextualised with what reported in other quasi-hydrostatic pressure studies performed on Cu_2OSeO_3. AC susceptibility measurements in [64] show an increase of the ordering temperature of $+2.5\%$ at 6 kbar, comparable with what observed in our measurement. However, the concomitant increase in $H_{\rm C1}$ of 15%, the decrease in $H_{\rm C2}$ of 9%, and the massive enlargement of the skyrmion pocket ($\Delta T_{SkL}(6$ kbar$)=$ 10 K) compared to the ambient pressure data ($\Delta T_{SkL}($ambient $P)=$ 2 K) that are also reported in the same study, were not observed during our measurements. Other AC susceptibility measurements report a significant increase of the size of the skyrmion pocket in a single crystal of Cu_2OSeO_3, passing from a temperature extent of ≈ 3 K at ambient P to ≈ 5 K at 5.22 kbar [63], not consistent with our findings in our measurements.

Such strong effects on the critical fields and ordering temperatures are instead attributes of chiral magnets under directional stress. In MnSi, $T_{\rm C}$ is suppressed slightly under the application of uniaxial compressive stress, and it reaches 0 at a critical pressure of $P_C \approx 14.6$ kbar [99]. Under uniaxial stress, it has also been shown that $H_{\rm C1}$ increases or decreases according to the mutual orientation of the applied stress σ and the applied field H. Moreover, the skyrmion phase stability is enhanced when $\sigma \perp H$ and suppressed when $\sigma \parallel H$ [59, 60].

In Cu_2OSeO_3 the effects of uniaxial pressure have been studied in [61] where the compressive strain $\sigma \parallel [110]$ and the applied field was $\mu_0 H \parallel [1\bar{1}0]$. This study

showed an important increase of the temperature extent of the skyrmion pocket from 1 K at ambient pressure to ≈ 3 K at just 1 kbar. It was also reported a rise of H_{C1}, which tripled under the same applied pressure.

Considering the similarities in the variation of both the skyrmion pocket's size and H_{C1} observed in uniaxial stress measurements [59–61] and quasi-hydrostatic measurements [63, 64], these latter data are expected to be affected by unwanted uniaxial pressure components. The choice of the pressure transmitting medium is the most likely responsible for these effects.

The PTM of choice in both hydrostatic pressure studies was Daphne Oil 7373. In both cases, the pressure changes were performed at room T, however, the PTM freezes at temperatures linearly varying from ≈ 182 K at ambient pressure to ≈ 290 K at 1.9 GPa [105]. Contractions of the frozen PTM happening in the cooling from the PTM freezing temperature to the temperature of the measurements could induce unintentional directional components in the applied pressure. Although gaseous PTMs, as the one used in our work, provide better hydrostaticity than liquid PTMs, even when frozen [101], it is very difficult to completely get rid of these directional components of the pressure, as underlined in our measurements by the uneven populations of the helical domains. We still considered the effects of these strains to be small enough not to affect our measurements.

In conclusion, the application of quasi-hydrostatic pressure on Cu_2OSeO_3 induced only minor modifications of its magnetic phase diagram. For a fixed point in the **H-T** phase diagram, pressure act as a third thermodynamic variable that could be exploited to stabilise skyrmions at higher temperature in this archetypal insulating skyrmion material. The small effects observed are in contrast with the strong variation of the skyrmion pocket size and critical fields reported previously for Cu_2OSeO_3 under hydrostatic pressure [63, 64].

Chapter 4

Position dependent structure and metastability of the skyrmion state in Ni substituted Cu_2OSeO_3

The contents of this chapter are published in [80]. The SANS experiments were performed by M. Crisanti, Dr R. Cubitt, Dr M. N. Wilson, Dr M. T. Birch and S. Moody. Dr M. T. Birch performed the magnetometry measurements. Dr B. M. Huddart performed the DFT calculation. M. Crisanti and Dr R. Cubitt performed the neutron diffraction measurements. A. Tengattini performed the X-ray tomography measurements. The data analysis was done by M. Crisanti, who also worked on the article's publishing process. The figures in this chapter are adapted or reproduced from [80]

For the future development of skyrmionic devices, it is essential to understand the link between the features of the hosting materials and the skyrmion lattice's characteristics. This crucial link enables the engineering of skyrmion materials with features specific to the environment in which they have to be employed (e.g. room temperature T_C, zero field skyrmion state) and with specific characteristics of the skyrmion lattice. In this context, the study of how the shape of bulk skyrmion hosts influences the characteristics of the skyrmion lattice is of crucial importance to understand how such macroscopic features can modify the microscopic magnetism of the material.

Among the different techniques available to characterise bulk skyrmion hosts, magnetometry is widely employed to determine the magnetic phase transitions of the samples, however it does not provide information on the actual ordering of these magnetic phases. However, as the skyrmion lattice exhibits a very long periodicity, it is possible that its structure changes across the material and averaging techniques such as magnetometry cannot provide spatially resolved information. On the other hand, microscopy provides spatially resolved information on the magnetic ordering, but it is only sensitive to the surface of the sample. Techniques like SANS, in combination with high-brilliance sources such as the ILL, allow spatially resolved characterization of the sample while providing direct information on the magnetic ordering. The perfect candidate for the study of spatial variations of the skyrmion lattice and its metastable state was a very large single crystal of Ni substituted Cu_2OSeO_3 with a nominal concentration of Ni of 14% (($6 \times 3 \times 3$) mm^3, 225 mg). At the same time, a single crystal of pristine Cu_2OSeO_3 was also measured to provide a comparison with the parent compound.

4.1 Experimental setup and methods

The SANS measurements were performed on the D33 beamline at ILL. Both samples were mounted on a 200 μm thick Al plate and placed inside a cryomagnet. The samples were aligned to have a [110] crystal axis parallel to the incoming neutron beam, and a [1$\bar{1}$0] direction perpendicular to it, and vertical. The neutron beam was monochromatised to a wavelength $\lambda = 6$ Å, with a FWHM fractional spread of $\Delta\lambda/\lambda = 10\%$. The beam had a collimation length of 7.8 m before the sample, and the scattered neutrons were collected 7.8 m after the sample on a two-dimensional multi-detector. The Ni substituted Cu_2OSeO_3 sample was illuminated by neutron using two different apertures of the beam. A 6 mm diameter aperture was employed to illuminate the whole sample. A 1 mm diameter aperture was used to illuminate
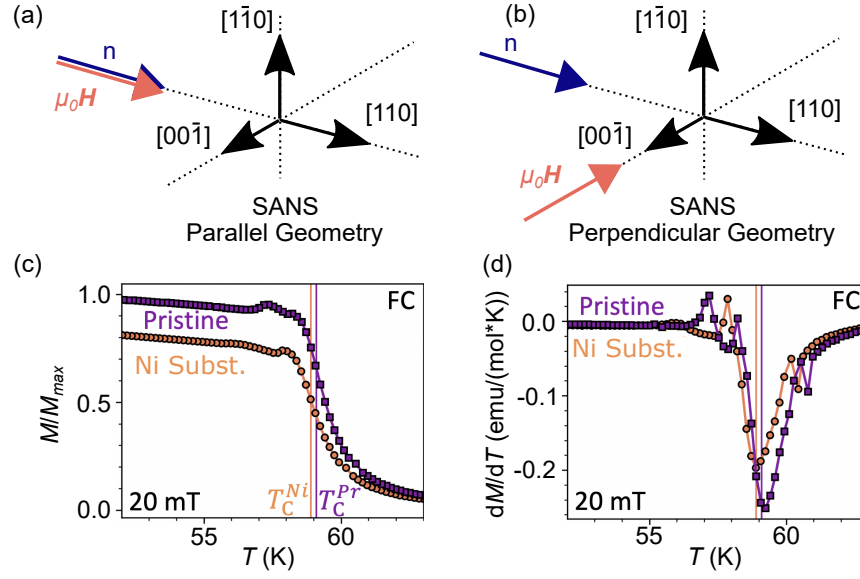
Figure 4.1: **(a)** and **(b)**: Schematic of the two SANS experimental geometries. **(c)** Magnetisation measured as a function of decreasing temperature with an applied magnetic field of 20 mT for the pristine (purple squares) and Ni substituted (orange circles) sample. **(d)** The calculated gradient of the magnetisation with temperature. The minima of this data were used to define T_{C}, indicated by the coloured vertical lines in both panels.

specific areas of the sample and spatially resolve the skyrmion lattice structure horizontally, translating the sample and the magnet relative to the neutron beam. Given the smaller dimensions of the pristine sample, it was impossible to perform the same type of measurements, hence a 3 mm aperture was employed, illuminating the whole sample. The magnetic field was applied parallel to the incoming neutron beam to study the skyrmion state, and perpendicular to it to study the conical state. The geometries of the experiments are shown in Figure 4.1.

The skyrmion lattice structure was studied collecting rocking curves, rotating the sample and magnetic field together around the vertical axis, recording the scattered intensity as a function of rocking angle. For these measurements, the rocking angle $\omega = 0°$ was calibrated to correspond to the direction of the applied magnetic field, using the scattering from the flux line lattice of superconducting Nb [106]. The phase diagrams collected during the neutron experiment were measured either by zero field cooling (ZFC) to a set of target temperatures and then performing field scans (6 mm aperture), or by high field cooling (HFC), in 50 mT, and then performing temperature scans at different target fields. In both cases, the magnetic history of the sample guarantees that only the equilibrium skyrmion state

was measured, with no effect induced by metastability.

The metastable skyrmion state was also measured in different areas of the Ni substituted sample. The sample was rapid field cooled (RFC) from 70 K to the chosen target temperatures at a 7 K/min cooling rate. The lifetime measurements were performed collecting diffraction patterns at a specific rocking angle. Although this method did not provide the time dependency of the full scattered intensity of the metastable skyrmion state, but only of part of it, measuring only one rocking angle made the measurement faster, optimising this type of measurement.

4.1.1 Magnetometry

The pristine and Ni substituted samples were first characterised with magnetometry measurements. Although the spatial characterisation of the different magnetic states was not possible, these measurements provided important information on the position and size of the skyrmion pocket, and about the population of the metastable skyrmion state. DC and AC magnetometry measurements were performed using commercial SQUID-VSM, a Quantum Design MPMS3. The samples were glued to a quartz rod and aligned with the [110] crystal axis parallel to the applied magnetic field, similarly to the neutron scattering measurements. The AC susceptibility measurements were performed with a field amplitude of 0.1 mT, oscillating at a frequency of 10 Hz. For the investigation of the metastable skyrmion state, the cooling rate was set to 40 K/min. In this case, two sets of measurements were performed, where the samples were FC in 22 mT to different target temperatures, then field scans were collected either increasing or decreasing the applied field. The magnetisation versus temperature curves are shown for both samples in Figure 4.1(c) and 4.1(d), and they were used to determine the ordering temperatures T_C, which resulted to be 59.1(1) K for the pristine sample, and 58.9(1) K for the Ni substituted sample.

4.1.2 Diffraction on SALSA

Neutron diffraction measurements were collected on the Ni substituted sample to investigate the presence of possible residual strain in the crystal structure. To look for a possible deformation of the crystal structure, the sample was aligned with the [110] crystallographic direction in the scattering plane and the [1$\bar{1}$0] perpendicular to it. In this orientation, the sample was rotated around its vertical axis to select a $2\theta = 63.5°$ to centre the position-sensitive detector on the Bragg reflection coming from the (440) plane. The intensity and position on the detector (2θ) of this Bragg

reflection was mapped across the sample with a neutron beam collimated to a voxel size of $0.5 \times 0.5 \times 2$ mm^3. The measurements were repeated at room temperature and zero applied magnetic field, and at 56 K and 22 mT. The data was reduced and analyzed with Large Array Manipulation Program [107].

4.1.3   X-ray Tomography

The sample volume and shape were studied with X-ray tomography measurements performed on NeXT instrument at the ILL [108] at room temperature and zero magnetic field. A polychromatic X-ray beam at 120 kV, 60 μA was collimated to a voxel size of 20 μm. A tin filter of 500 μm was added to cut low wavelengths, producing an X-ray beam peaking at 50 keV. The sample was mounted on a rotation stage. Transmission images were recorded as a function of sample rotation till the sample was fully illuminated. The tomography resulted in 1312 images, each recorded as an average of 7 single frames, each one with an exposition of 0.3 s.

4.1.4   Density Functional Theory calculations

To determine the Young's modulus of Cu_2OSeO_3, we used the plane-wave basis-set electronic structure code CASTEP [109] and worked within the generalized-gradient approximation (GGA) using the PBE functional [110]. We used a plane-wave cutoff energy of 1000 eV and a $5 \times 5 \times 5$ Monkhorst-Pack grid [111] for Brillouin zone sampling, resulting in stresses that converged to 0.1 GPa. Elastic constants were obtained by applying a series of strains to the unit cell and calculating the corresponding stresses.

4.2   Results

Figure 4.2(a) and 4.2(b) shown the magnetic phase diagrams of both the pristine and Ni substituted samples, respectively, derived by AC susceptibility χ'. The measurements were performed FC in 22 mT in a range of target temperatures between 49 K and 61 K, and then performing increasing scans. The systems were then reset and FC again in 22 mT to the same target temperatures, then performing decreasing field scans. The features in these scans identify the different magnetic states present in the samples at the range of temperature and magnetic field explored. In Figure 4.3 are presented the χ' measurements at 57.5 K and 50 K for both samples. The low intensity value measured at zero applied field corresponds to the helical state. When the field is increased, the intensity increases as the system passes into
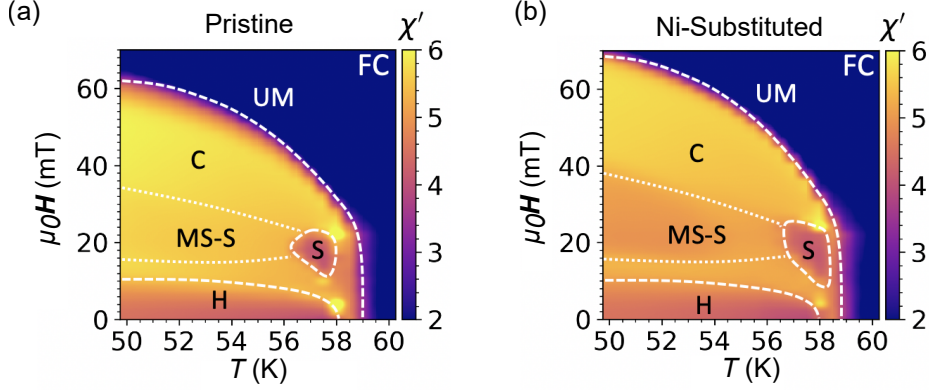
Figure 4.2: **(a)**, **(b)**: Magnetic phase diagrams of the pristine and Ni substituted samples, respectively. The colourmap plots the real component of the AC susceptibility, χ', as a function of temperature and applied magnetic field. The different magnetic states are labelled: helical (H), conical (C), skyrmion (S), metastable skyrmion (MS-S), uniform magnetisation (UM). The phase diagrams have been collected field cooling (FC).

the conical state. The lower intensity region for fields around 20 mT at temperatures around 58 K corresponds to the skyrmion state [112]. By further increasing the field, the intensity increased again when the sample entered conical state a second time and abruptly decreases for high applied magnetic fields, when the sample passes in the paramagnetic state.

Little difference is observed between the pristine and Ni substituted samples at 57.5 K, as depicted in Figure 4.3(a) and 4.3(b). In these panels are also shown the imaginary components of the susceptibility, χ''. The peaks in χ'' identify the transition regions between the conical and skyrmion states, and between the helical and conical sates. These peaks arise from magnetic excitations at the boundaries between different magnetic states of the sample [112]. To facilitate the comparison between the signals of the two different samples, the peaks of the imaginary components of the susceptibility were normalised to the highest measured value of χ'' in the pristine sample, at 57.5 K.

In Figure 4.3(c) and 4.3(d) are shown the real and imaginary part of the susceptibility collected for both samples at 50 K zero field cooling (ZFC) and field cooling (FC). From the comparison of the curves between the two samples, it is possible to notice that in the FC data of the Ni substituted sample, the value of χ' is reduced more significantly than for the pristine sample around 20 mT. This reduction is observed at all temperatures and indicates the creation of a metastable skyrmion state due to the FC across the skyrmion pocket [42, 56, 75]. The in-
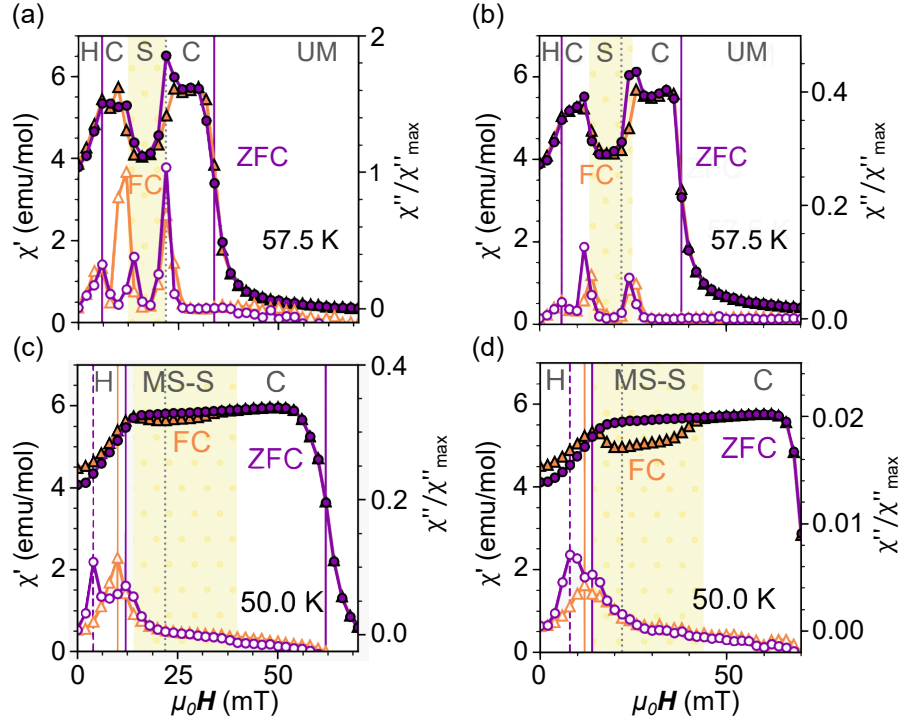
Figure 4.3: AC susceptibility measurements performed at 57.5 K **(a, b)** and 50.0 K, **(c, d)** following the ZFC (purple circles) and FC in 22 mT (orange triangles) plotted as a function of the applied field for the pristine **(a, c)** and substituted **(b, d)** samples. The real and imaginary components are denoted by the filled and outlined markers, respectively. Vertical lines indicate phase boundaries determined by features in the χ'' data, which was normalized to the highest value of χ'' of the pristine sample at 57.5 K. All the helical (H), conical (C), skyrmion (S), metastable skyrmion (MS-S), uniform magnetisation (UM) and paramagnetic (PM) states are labelled.

Figure 4.4: **(a)**: SANS H-T phase diagram of the Ni substituted sample, derived by summing the scattered neutron intensity in the region of the detector between the two white circles indicated in panel (b). The dashed lines serve as a guide to the eye to identify the boundaries between the various magnetic phases in the sample. The solid white vertical line indicates the value of T_C measured with AC susceptibility (Figure 4.3).
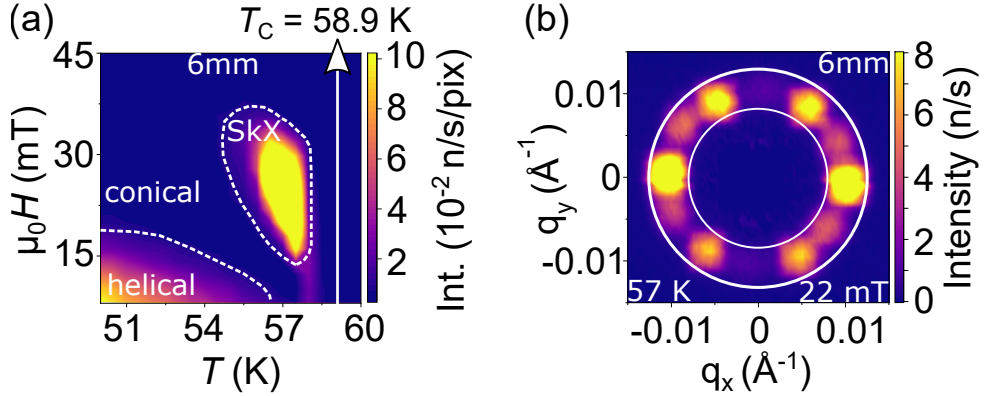
creased reduction of the χ' data in the Ni substituted sample indicates an increased metastable skyrmion population, suggesting that the substitution of Cu ions with magnetic Ni ions affected the metastable skyrmion state in a similar manner than what reported for Zn substituted Cu_2OSeO_3 [49].

The χ'' component at 50 K shows broader peaks in the Ni substituted sample Figure 4.3(d) rather than in the pristine Figure 4.3(c). This characteristic has been previously observed in Zn substituted Cu_2OSeO_3, and it was attributed to pinning effects on the different magnetic states introduced by the dopant [113]. Moreover, in both samples, two peaks are present in the ZFC χ'' data, indicating the reorientation of different helical domains when the field is applied along the [110] direction, already observed in pristine Cu_2OSeO_3. It was shown that this reorientation was suppressed in Zn substituted Cu_2OSeO_3 [113], suggesting that the Ni substitution affect the magnetic phase transitions in a completely different manner than the Zn substitution.

The Ni substituted sample phase diagram was also derived from SANS measurements, and it is shown in Figure 4.4(a). The equilibrium skyrmion pocket is enlarged compared to the pristine sample, in agreement with the magnetometry measurements in Figures 4.2(a) and 4.2(b). This enlargement of the skyrmion pocket was also previously reported for polycrystalline samples of Ni substituted Cu_2OSeO_3 [70, 72].

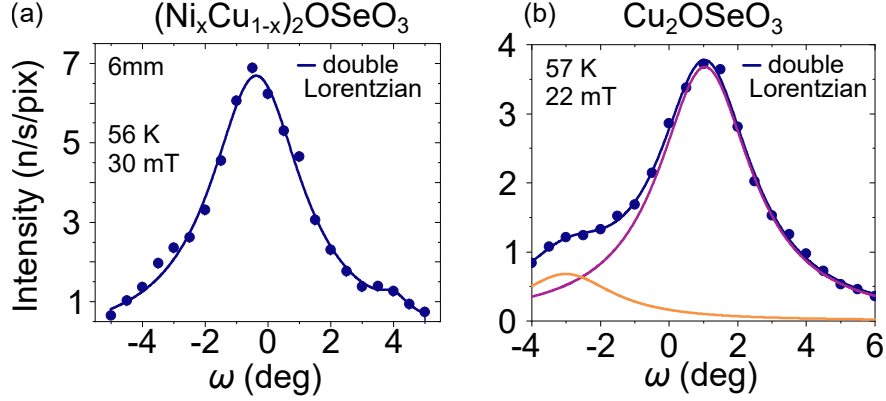During the SANS measurements, it was possible to characterise the ordering

Figure 4.5: **(a)** Mid pocket rocking curve of the equilibrium skyrmion state of the Ni substituted sample. **(b)** Mid pocket rocking curve of the pristine sample. Both data sets in panel (a) and (b) fit to the sum of two Lorentzian functions (dark blue), that are singularly shown in purple and orange in the case of panel (b).

of each magnetic state of the samples. The skyrmion lattice state was studied with the magnetic field applied parallel to the incoming neutron beam and it was identified by the typical hexagonal scattering pattern, shown for the Ni substituted sample in Figure 4.4(b). The helical state was also studied in the parallel geometry, where the helical domain visible was the one pinned along the [001] crystal axis and characterised on the detector by two horizontal spots. The conical state was studied in the perpendicular geometry, where the magnetic field was applied perpendicular to the incoming neutron beam, and it was also characterized by two horizontal diffraction spots. The scattering patterns of each magnetic states formed at specific values of momentum transfer, or $\mathbf{q}$. The one measured for the skyrmion state was $q_{SkX} = 0.0103(1)$ Å^{-1}, the same value, within experimental uncertainty, as that measured for the helical state $q_h = 0.0104(1)$ Å^{-1}. The corresponding lattice spacing of the skyrmion state was $d_{SkX} = \frac{2\pi}{q_{SkX}} \simeq 607(8)$ Å, in agreement with previously published work on the pristine and Zn substituted samples [2, 49].

To study the full scattered intensity of the horizontal diffraction spots of the skyrmion state, rocking curves were collected in the centre of the skyrmion pocket for both samples and are presented in Figure 4.5(a) for the Ni substituted sample and in Figure 4.5(b) for the pristine one. In both cases, the rocking curves display multiple peaks, one near to $\omega = 0°$ and a second one, less intense, at higher rocking angles. The data fit well to the sum of two Lorentzian functions, one for each peak, indicating the presence of two skyrmion domains tilting away differently from the direction of the applied magnetic field, and with a different spread of angles. These domains are in addition to the one azimuthally rotated by 30° that can be observed
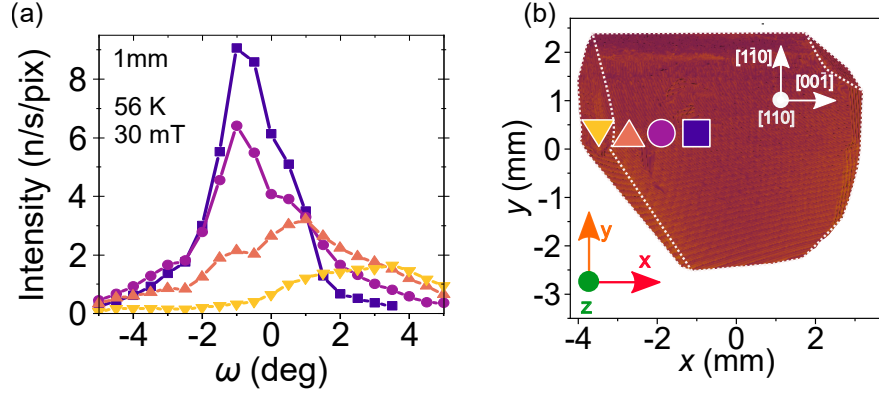
Figure 4.6: **(a)** Rocking curves recorded in the equilibrium skyrmion state with a 1 mm aperture at different positions on the Ni substituted sample. Each rocking curve was measured translating horizontally in steps of 0.5 mm on the sample surface indicated in panel (b). **(b)** X-ray tomography of the surface of the sample struck by neutrons during the SANS experiment. The dashed white lines are a guide to the eye that identify the edges between adjacent surfaces. The symbols are a guide to the eye to identify the positions at which each of the rocking curves in panel (a) were measured.

on the detector plane in Figure 4.4(b), as they lie on the plane perpendicular to the detector. In order to ascertain how the multiple skyrmion domains were distributed within the sample, a 1 mm aperture of the neutron beam was utilised to selectively study specific areas of the sample, and spatially resolve its magnetic features.

Rocking curves, presented in Figure 4.6(a), were collected with a 1 mm aperture in the equilibrium skyrmion pocket, translating the Ni substituted sample across its horizontal axis in 0.5 mm steps, as displayed in Figure 4.6(b). The rocking curves' features change dramatically at each step across the sample surface: towards the edge of the sample, the rocking curves are wider and peak away from the direction of the applied magnetic field. Moving towards the centre of the sample, the rocking curves peaks shift towards $\omega = 0°$ and become sharper, indicating skyrmion domains better aligned with the direction of the applied field.

The spatial dependence of the conical and skyrmion structures was thoroughly investigated with a detailed set of rocking curves collected across the sample's horizontal axis, on the line indicated by the symbols in Figure 4.6(b). As the rocking curves provide information on the ordering of the magnetic stated in the same direction as the neutron bean, hence perpendicularly to the detector plane, to help with the visualisation of their characteristics, Figure 4.7 was created. Here a three dimensional representation of each rocking curve is given at each different position on the sample. Each cone correspond to one fitted Lorentzian function to

the rocking curve data of the horizontal diffraction spots. The length of the cones is proportional to the fitted maximum intensity, the width of the cones is proportional to the FWHM of the peak, and the orientation of the cones is proportional to the tilting angle of the rocking curve, hence the fitted position of the peak.

To spatially resolve the characteristics of the conical state structure, the magnetic field was applied perpendicular to the incoming neutron beam, along the [001] crystal axis. This magnetic state produced two horizontal diffraction spots at the detector position, identifying the spatial variation of the conical state. The conical state was measured at 50 K at both 8 mT and 30 mT, as shown in Figures 4.7(a) and 4.7(b), respectively. For the lower field, are reported multiple cones in several sample positions. This indicated multiple conical domains tilting away differently from the direction of the applied magnetic field. As the field was increased to 30 mT, the multi domains present in the plane perpendicular to the detector were suppressed in favour of single peaking rocking curves varying smoothly across the sample. The tilting of the conical domains was overall comparable between the low and high field measurements, however an increased tilting was observed locally at the edges of the sample.

The detailed spatially resolved scan of the skyrmion lattice across the sample, performed at 56 K and 30 mT, is presented in Figure 4.7(c). Overall, the rocking curves collected do not show a smooth modification of their characteristics across the scan, in contrast to the conical state scan performed at the same applied magnetic field. The sample's right side displayed both multiple sets of six-fold scattering patterns, indicating multiple skyrmion domains on the detector plane, and multiple peaks in the rocking curve profile, indicating multiple skyrmion domains also in the plane perpendicular to the detector. The left side of the sample was instead characterised by a more uniform lattice, presenting only one six-fold scattering pattern, although still showing multiple peaks in the rocking curves of the horizontal scattering spots. Focusing on the left side of the sample, a decrease of the tilting angle of the skyrmion tubes was observed as moving from the edge to the centre. The skyrmion domains were tilting strongly up to an angle of $\pm 4°$ away from the applied magnetic field direction, compared with the thinner and more aligned rocking curves measured in the centre.

The increased tilting of the conical and skyrmion domains at the edges of the sample compared to its centre shows a difference in the alignment of the magnetic texture between the edges and centre of the sample. In combination with the increased tilting observed at the edge of the sample in the conical state when increasing field, these effects indicate a strong influence of demagnetisation on the

magnetic textures structures linked to the complex shape of our singe crystal. A similar effect was previously observed on the skyrmion state in MnSi and attributed to demagnetisation fields [114], consistent with our observations.

4.3   Equilibrium skyrmion region

In the complex map of the skyrmion lattice, two regions of the sample were chosen to focus on that hosted two different skyrmion states, identified in Figure 4.7(c) by a purple square and a yellow triangle, and shown in detail in Figures 4.8, 4.9 and 4.10. The first area was chosen towards the centre of the sample and was characterised by a rocking curve showing one main peak, mostly aligned to the direction of the applied magnetic field as it was peaking at $\omega = 0.65(5)°$, as shown in Figure 4.8(a). The second region of interest was chosen towards the edge of the sample, where the rocking curve of the skyrmion state showed a double peaking rocking curve with main angles $\omega_1 = -3.5(1)°$ and $\omega_2 = -1.2(1)°$, significantly tilting away from the direction of the applied field, as shown in Figure 4.8(b). The characteristics of the rocking curves in these two regions taken together represent the main features of the rocking curve collected illuminating the whole sample, where the main peak was found at $\omega \approx$ -1°, and a second one was observed at $\omega \approx 3.5°$, as shown in the double fit in Figure 4.5(a). The similarity in the positions of the peaks of the rocking curve of the fully illuminated sample, with the position of the peaks of the rocking curve in the centre and at the edge of it, suggested that focusing on these two specific areas could be representative of the general behaviour of also other regions of the sample that were not detailed during these measurements. We refer to these two selected regions of the sample as "centre" and "edge".

In addition to the differences that were observed in the structure of the skyrmion lattice, remarkably these two regions of interest displayed significantly different skyrmion pockets, extending over different regions in magnetic field and temperature, as shown in Figure 4.9(a) and 4.9(b). The skyrmion domain present in the centre of the sample existed over a region of the phase diagram similar to the one that was identified for the fully illuminated sample both with neutron and AC susceptibility, as shown by the comparison of Figures 4.9(a), 4.4(a) and 4.2(b). Instead, the edge skyrmion domain displayed a skyrmion pocket twice as much extended in temperature rather than in the central area but maintained a similar field range.

To identify the presence of these specific skyrmion domains across the sample, Figures 4.10(a) and 4.10(a) were produced. The skyrmion scattered intensity was
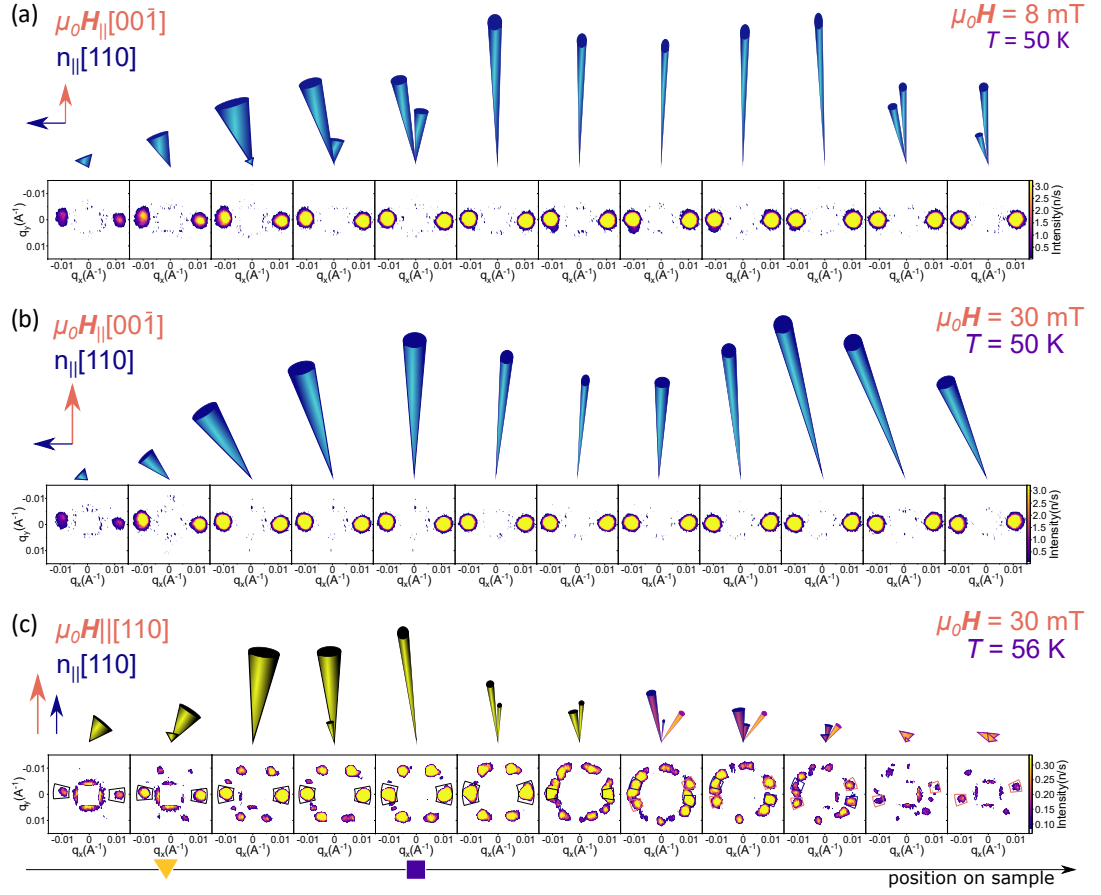
Figure 4.7: (a), (b): scattering patterns of the conical state at 30 mT and 8 mT, 50 K, collected across the sample surface in steps of 0.5 mm. (c) : scattering patterns of the skyrmion state at 30 mT, 56 K, collected across the sample surface in steps of 0.5 mm. In each case, the rocking curves of the horizontal spots in the scattering patterns were analysed, and their characteristics are reported by the cones above the scattering patterns. The rocking curves were fitted to a suitable combination of Lorentzian functions: each cone corresponds to one of these functions. Where multiple cones are present, the rocking curves were characterised by multiple peaks, hence fitted to the sum of multiple Lorentzian functions. The intensity of the fitted curves is proportional to cones' height, and in the skyrmion case this height was multiplied by 10 compared to that of the conical state. The FWHM of the fitted curves is proportional to the cones' width, in the range from 0.3° to 5°. The centre of the fitted curves is proportional to the cones' tilting angle, in a range going from −4° to +4°. The direction of the applied field and the neutron beam are shown in the top left of each panel. Where multiple domains were visible in the scattering patterns of the skyrmion state, the pairs of spots analysed were boxed and colour coded in the same way as the corresponding cones.

71
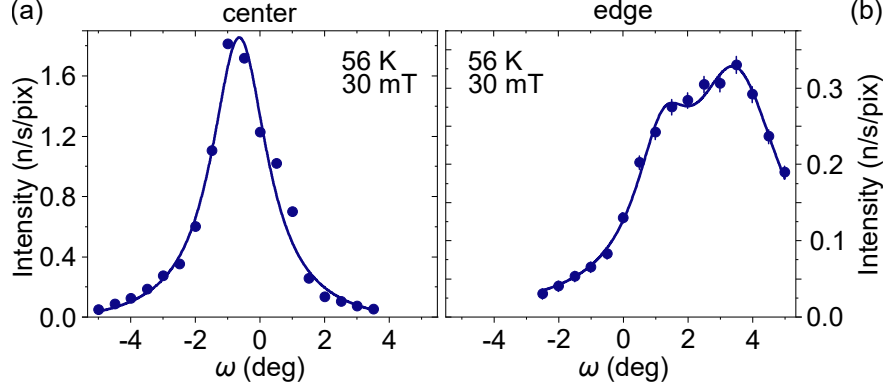
Figure 4.8: **(a)**, **(b)**: mid-pocket rocking curves collected towards the centre of the sample and at its edge, respectively, showing the differently oriented skyrmion domains.
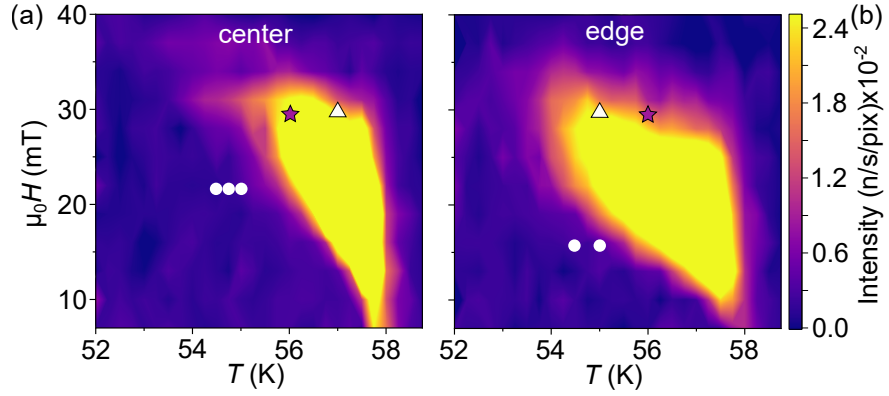
Figure 4.9: In (a) is shown the phase diagram measured at the centre of the sample, while in (b) the one measured at the edge. The skyrmion pocket appears enlarged in temperature at the edge of the sample compared to the centre. The white dots in the diagrams correspond to the H - T parameters at which the lifetime of the metastable skyrmion state was measured in each area. The stars indicate the point at which the rocking curves in Figure 4.8 were measured. The white triangles indicate the H - T conditions under which the graphs in Figure 4.10 were measured.
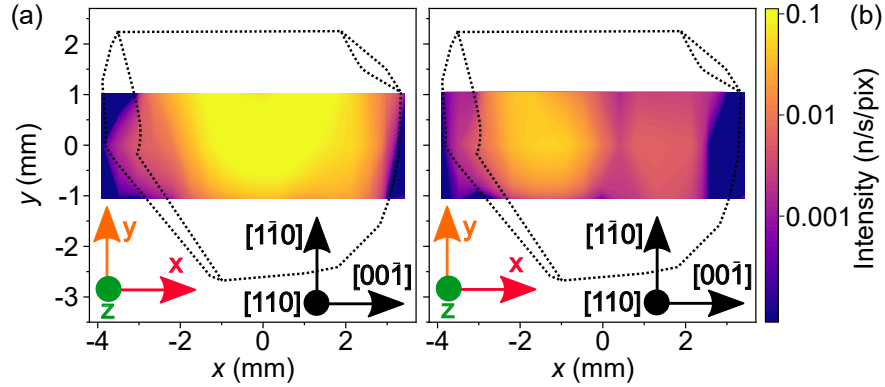
Figure 4.10: In this figure, the presence of the aligned (centered) skyrmion domain (a) and misaligned (edge) skyrmion domain (b) is measured across the sample. The colour map was constructed interpolating three horizontal scans performed with 1 mm aperture at three different y positions, in steps of 1 mm.

recorded at $\omega = -0.65°$ in the centre position, and at $\omega = 3.1°$ at the edge position, in three horizontal scans across the sample, performed at y = -1, 0 and 1 mm. The edge skyrmion domain was principally located on the left side of the sample, where we found the broadest rocking curves and the highest average tilts away from the applied magnetic field direction.

The structural differences of the skyrmion lattice across the sample identified in the edge and central position and the localised presence of the edge domains are effects consistent with strong demagnetisation effects [114] linked to the complex shape of the sample, which is shown in Figure 4.11(b). Specifically, thanks to the complementary X-ray tomography measurements, it was possible to identify a cavity inside the sample which position corresponds to the right side of the rocking curve scan presented in Figure 4.7(c). The skyrmion lattice structure between x = 0 and 2 mm is significantly affected by the presence of this cavity, which is consistent with demagnetisation effects coming from the inner structure of this small void in the sample. As the demagnetizing field changes the value of the internal field in the sample according to its shape, small shifts in the magnetic field extent and position of the skyrmion pocket could be expected in different areas. However, demagnetisation effects cannot explain the substantial enhancement of the temperature range of the skyrmion pocket observed at the sample's edge.

Non-uniform residual strain across the sample could be responsible for this disparity in the skyrmion pocket size, as previously shown for bulk skyrmion hosts under uniaxial stress [59–61]. This possibility was investigated with neutron diffraction on the SALSA beamline in ILL.
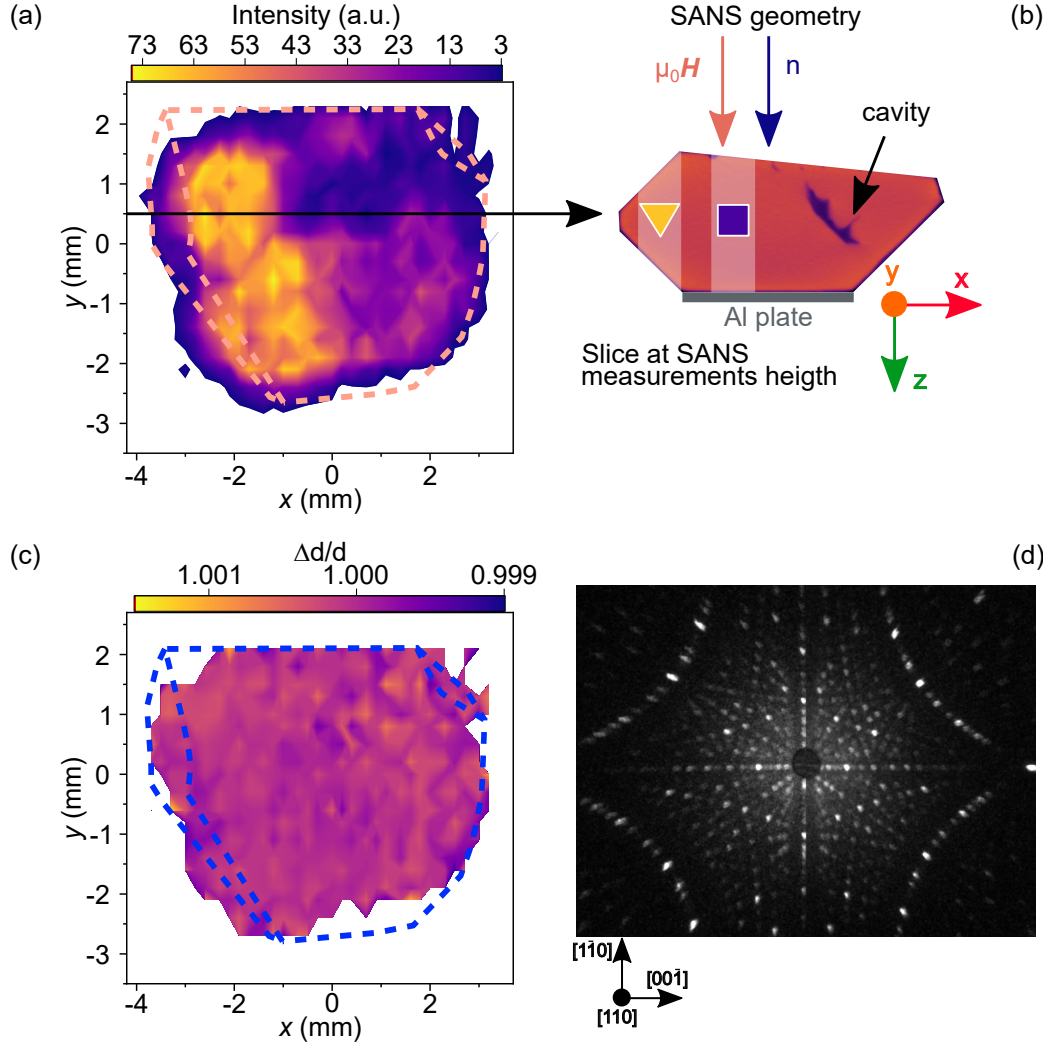
Figure 4.11: **(a)**: map of the intensity of the (044) Bragg peak. **(b)** mid height slice of sample in the x-z plane derived from X-ray tomography. Both the neutron beam and the magnetic field direction are indicated and refer to the SANS experiment's geometry. A cavity is visible on the right side of the sample. The shaded areas marked with the yellow triangle and the blue square refer to the edge and central skyrmion domains' positions, respectively. **(c)**: fractional variation of the crystal lattice d-spacing across the sample. **(d)**: neutron Laue image of the sample.

74

The neutron diffraction measurements were carried out at room temperature, zero applied magnetic field, and at 56 K in a field of 22 mT, to verify whether the temperature change or the application of an external field would influence the internal strain of the sample. The (044) Bragg reflection was positioned at the centre of the position-sensitive detector, then the sample was translated in the beam, mapping out the position and intensity of the reflection across the sample. Firstly, a rocking curve of this diffraction spot was taken illuminating the centre of the sample to identify the angle of the (044) peak (FWHM $\approx 1°$), and then scanned across the sample at this fixed angle to map the peak intensity. This data is shown in Figure 4.11(a).

The variation of intensity of the peak recorded during the measurements was due to two main factors. Firstly, as the rocking curve of the Bragg reflection had a narrow width, a decrease in intensity could correspond to a change in its mean direction, in its width, or both. However, the sample's structure was inspected with a neutron Laue instrument, illuminating the whole sample, and showed no defects in its single crystal structure, Figure 4.11(d). Hence, the variations expected in the mosaic spread were on the scale of a fraction of a degree. Secondly, the intensity variation of the (044) Bragg peak across the sample could be due to a variation in the sample volume illuminated. The complex shape of the sample, combined with the small cavity located with X-ray tomography, (Figure 4.11(b)) meant that different volumes of the sample were illuminated at different positions of the sample scan, which was expected to be the main contribution to this intensity variation.

The main objective of these measurements was to identify any variation of the fitted 2θ position of the Bragg reflection on the detector, hence any variation of the d-spacing of the (044) planes, indicating a variation in the residual strain in the sample. In Figure 4.11(c) is presented the mapping of the fractional variation of the d-spacing as a function of position in the sample at 56 K, 22 mT, up to a precision of 10^{-4}. No variation of the internal residual strain in any area of the sample was observed, as no variation of the d-spacing was observed across the sample. A 0.09% difference was observed between the room temperature, zero magnetic field measurement and the 56 K, 22 mT measurement, consistent with the thermal contraction expected for this material [89], which suggests the absence of strain induced by the magnetism below T_C.

The skyrmion pocket extension we observe in our measurements at the edge of the sample is comparable to what previously reported in [61], where uniaxial stress was applied to a single crystal of Cu_2OSeO_3. Our results would have required an applied stress of the order of 100 MPa to have produced an equivalent change

of the size of the pocket. To quantify the associated change in the d-spacing with the stated applied uniaxial pressure that was reported in [61], the Young's modulus of Cu_2OSeO_3 was calculated using density functional theory, and determined to be 67(9) GPa. Assuming that a stress of 100 MPa is necessary to obtain the extended skyrmion pocket measured at the edge of our sample, with the calculated Young's modulus, a difference of 1.5×10^{-3} is expected between the d-spacing at the centre and at the edge of the sample, well above the sensitivity of the neutron diffraction measurements of 10^{-4}. As no variation of the lattice parameter was observed on this scale, strain is not the cause of the skyrmion pocket expansion.

4.4   Skyrmion Metastability

As previously discussed in Section 1.1.4, a metastable skyrmion state can be created via rapid field cooling (RFC) through the skyrmion pocket to low temperatures. Such skyrmion state decays over time in the actual magnetic ground state of the system studied. To study the decay of the metastable skyrmion state, it is important to select the target temperatures of the RFC procedure to produce a metastable state with a lifetime suitable for the time resolution provided by the technique used. According to previously reported measurements on pristine and Zn substituted Cu_2OSeO_3, lifetimes of minutes to hours were expected when RFC in 22 mT to 54.5 K, 54.75 K and 55 K, suitable for the neutron scattering experiment. However, for these target temperatures, the sample would have still been in the equilibrium skyrmion state at the edge, as shown in 4.9(b). To maintain the same range of lifetimes while maintaining the same target temperatures for the RFC, the magnetic field was adjusted to 16 mT for the metastable measurements at the edge of the sample. In both areas, the lifetimes were measured by collecting single scattering patterns sequentially at single rocking angles, corresponding to the peak of the rocking curves measured in the equilibrium pocket.

The lifetimes of the central metastable skyrmion state were determined fitting the decaying intensity to a single exponential with the addition of a flat background, $I = y_0 + I_0 exp(-t/\tau)$. The characteristic times obtained for each measurements were: $\tau(54.5 \text{ K}) = 2978(56)$ s, $\tau(54.75 \text{ K}) = 768(11)$ s, $\tau(55 \text{ K}) = 356(5)$ s. As expected from previous measurement on pristine and Zn substituted Cu_2OSeO_3 samples, the lifetimes decrease when increasing temperature. An increase of the characteristic lifetimes was observed compared to the ones reported for the pristine case [49], as supported by the magnetometry measurements shown in Figures 4.3(c) and 4.3(d). The lifetimes can be modelled using a modified Arrhenius's law, as
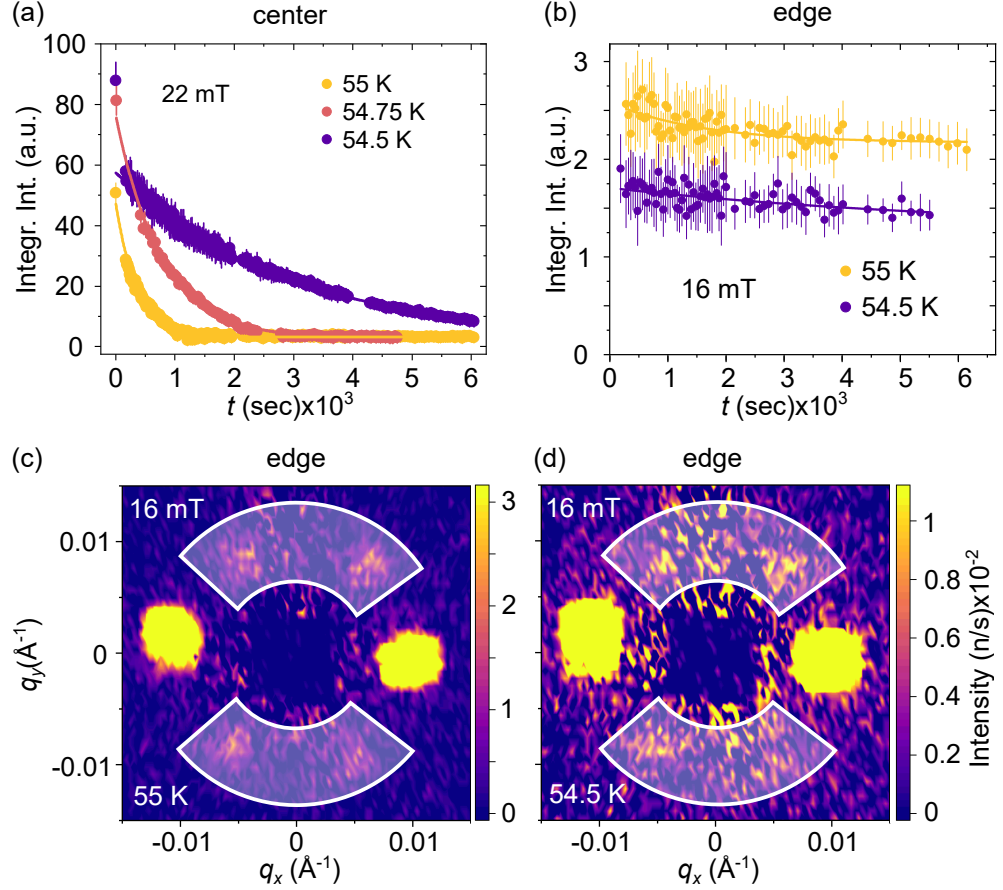
Figure 4.12: **(a)**: lifetimes measured in the centre of the sample, FC in 22 mT to 55 K, 54.75 K and 54.5 K. **(b)** lifetimes measured at the edge of the sample, FC in 16 mT to 55 K and 54.5 K. The solid lines correspond to the fit of the data to a single decaying exponential with an added background. **(c), (d)**: sum of scattering patterns over full rocking scans performed ~ 4000 s after the beginning of the lifetime measurements of the edge metastable skyrmion state at 55 K and 54.5 K respectively. The shaded areas highlight the parts of the detector where it was possible to observe scattering from the skyrmion lattice.

previously reported other work on metastable skyrmion states [34, 49, 67, 75]. The modified Arrhenius law used to fit the data was

$$\tau(T) = \tau_0 e^{\frac{a(T-T_C)}{k_B T}},$$

(4.1)

expressing the temperature dependence of the metastable skyrmion state's lifetime in terms of the activation energy of the decaying process. From the fit of the data, we extracted the activation energy parameter, $|a| = 209(36)$, and the attempt time, $\tau_0 = 9(3)$ s. These results are comparable with what was reported for the CoZnMn alloys in [34]. Moreover, an increase in the activation energy parameter a, compared to pristine and Zn substituted Cu_2OSeO_3 [49], is also observed.

Remarkably, the edge metastable skyrmion state did not show a clear time dependence at any of the selected target temperatures, as shown in Figure 4.12(b), compared to the lifetimes measured at the centre of the sample, shown in Figure 4.12(a). Overall, it was possible to notice a small decay of the scattered intensity over time, however the scattered intensity never approached zero, and the scattering pattern of the skyrmion lattice was visible at the end of the measurements, as shown in Figures 4.12(c) and 4.12(d). The scattered intensity was fitted to a decaying exponential with the addition of a flat background, similarly to the central state, but with poorer results compared to the central metastable state, mainly caused by the almost flat time dependency observed.

The results of both the fits of the central and edge metastable lifetimes are reported in Table 4.1. For the edge state, it is worth noticing that while for the 55 K data, the fit catches the early time small decay of the intensity. The fit of the 54.5 K data instead was more difficult, as the intensity variation over time is very small and on very long times, as showed by the fitting results indicating a characteristic time of 6500 s with an error of 9600 s, as reported in Table 4.1. Moreover, while for the central skyrmion state the fitted amplitude A is orders of magnitude bigger than the added flat background y_0, for the edge state the value of y_0 is indeed bigger than A, as reported in Table 4.1. In particular, the fact that the fitted amplitude result was just a fraction of the fitted flat background indicates the presence of a stable skyrmion structure, although presenting a long time dependence.

The fit results were used to produce the Arrhenius plot for both the central and edge states, as shown in Figure 4.13. Similarly to [34, 49, 67, 75], the data of both skyrmion states were fitted to a modified Arrhenius law, $\tau(T) = \tau_0 e^{\frac{a(T-T_C)}{k_B T}}$, expressing the temperature dependence of the metastable skyrmion state's lifetime in terms of the activation energy of the decaying process. From the fit, the activation
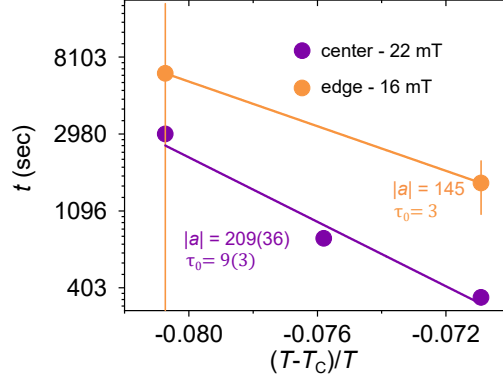
Figure 4.13: Arrhenius plot for the lifetime fits Figure 4.12. The data were fitted to a modified Arrhenius-like law. From the linear fit of the data, the activation energy parameter a and the attempt time τ_0 were extracted.

	T	y_0		A		τ	
	K	Value	Std.Err.	Value	Std.Err.	Value	Std.Err.
E	54.5	1.26735E-4	4.2698E-5	4.39564E-5	3.97145E-5	6560	9684
	55	2.17033E-4	3.07601E-6	4.12181E-5	5.706E-6	1576	527
C	54.5	1.24635E-4	3.93613E-5	0.00563	3.00824E-5	2978	56
	54.75	2.61165E-4	9.94339E-6	0.0074	1.19347E-4	768	11
	55	3.17443E-4	4.74491E-6	0.00445	8.39528E-5	356	5

Table 4.1: Fitted values of y_0, A, and τ for both the edge (E row) and central (C row) metastable skyrmion states.

Figure 4.14: Field warming scans performed in the centre and on the sample's edge, respectively. In each panel, the history of the measurement is indicated in the inset. The lifetimes' target temperatures shown in Figure 4.12 are marked on the temperature axis by coloured filled circles. Their colour matches the colour with which the lifetime measured at different temperatures are indicated in Figure 4.12.

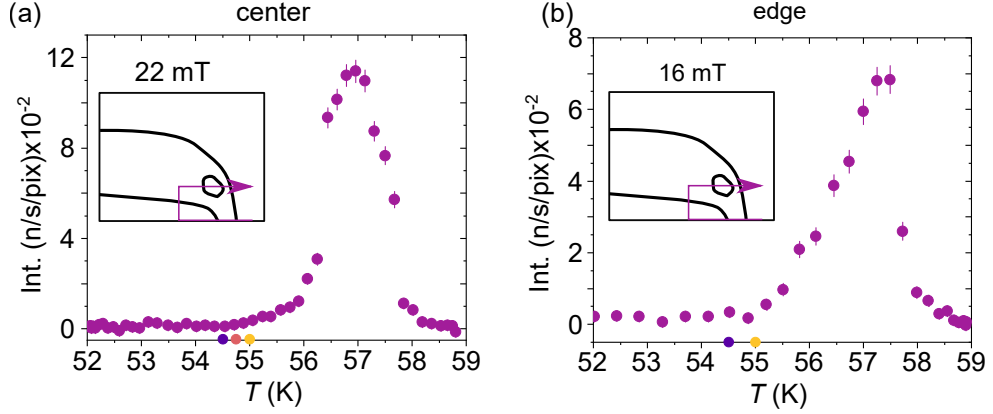energy parameter a and the attempt time τ_0 were extracted. For the central domain $|a_C| = 209(36)$ and $\tau_{0C} = 9(3)$ s. These results are comparable with what was reported for the CoZnMn alloys in [34]. Moreover, an increase in the activation energy parameter a, compared to pristine and Zn substituted Cu_2OSeO_3 [49], is also observed.

The Arrhenius plot of the edge data was of more difficult interpretation, given the poor quality of the lifetime fit and the stable component identified for the edge state. For this reason, although indicative of a possible change in the energy barrier and in the attempt time, the Arrhenius fit of the edge metastable lifetimes was not considered successful. Further measurements are needed to ascertain the actual time dependency of the metastable edge skyrmion state.

In Figures 4.14(a) and 4.14(b), we show the extent of the skyrmion pocket in the centre and at the edge of the sample, measured field warming after ZFC to 52 K. This demonstrates that the target temperatures chosen for the lifetime measurements, indicated by the coloured dots in both panels, were outside the equilibrium region of the skyrmion state both at 22 mT in the central area of the sample and at 16 mT at the edge.

4.5 Conclusions

Our measurements showed several differences between the skyrmion state at the edge and at the centre of the sample. These differences affected the skyrmion pocket

size, hence the stability of the skyrmion state (Figure 4.9(a) and 4.9(b)). They also affected the metastable skyrmion state (Figure 4.12(a) and 4.12(b)) and the skyrmion lattice structure (Figure 4.8(a) and 4.8(b)).

Demagnetisation effects explain the structural differences observed in the skyrmion lattice. In fact, from Figure 4.11(b), it is possible to notice that the shape of the sample is different between the two areas studied: the edge area is characterised by two surfaces, perpendicular to the incoming neutron beam, which are at approximately $45°$ to the applied field direction. The edge area is instead characterised by two surfaces almost parallel to each other and almost perpendicular to the applied field. The demagnetising field is responsible for variations in the direction and strength of the internal field [115], and these variations can explain the rocking curve profile of the skyrmion and conical state observed along the horizontal axis of the sample. The rocking curves at the edge presented higher tilting angles and wider profiles compared to the centre area. As both the skyrmion state and conical state align along the applied magnetic field's direction, these tiltings correspond to the tilt of the internal field lines, compared to the applied field, induced by demagnetisation effects due to the complex shape of the sample in this area. The observation of an increase of the tilting in the conical rocking curves when the external field strength is increased, shown in Figure 4.7(b), supports the demagnetisation as the main responsible for these structural differences, as this would accentuate the effects of the demagnetising field.

These results are supported by a previous work on MnSi, where on a disc-shaped sample, it was observed a broadening and a tilting of the skyrmion domains at the edges [114]. This is largely consistent with our observations. However, in the same study, the demagnetisation field affected the strength of the internal field significantly, inducing the nucleation of the skyrmion state at lower fields at the edge of the disc-shaped sample, compared to the centre [114]. We did not observe any measurable shift in field of the skyrmion pocket in our sample, instead we observed a surprising enhancement of the temperature range of the skyrmion pocket at the edge, compared to the centre. Demagnetisation effects alone do not account for the increased size of the skyrmion pocket.

A possible explanation for the observed enlargement of the skyrmion pocket is an uneven distribution of Ni content across the sample, as it has already been shown that an increase of Ni content is related to an expansion of the temperature range of the skyrmion pocket in Ni substituted Cu_2OSeO_3 [72]. However, the increased size of the skyrmion pocket is also accompanied by an increase in the ordering temperature T_C, hence a change in the boundary between the paramagnetic and conical state.

This boundary was measured in both areas of the sample, and resulted to be the same within uncertainty, ruling out a possible non-uniformity of the Ni content in the sample as an explanation for the enlarged skyrmion pocket in the edge area of the sample.

A steady value of T_C with a simultaneous extension of the temperature range of the skyrmion pocket towards lower temperatures is characteristics of the application of uniaxial pressure [59–61]. However, this effect was ruled out by our neutron diffraction measurements reported in Section 4.1.2.

Recently, the stability of individual skyrmions was related to the local order surrounding them [79]. In their work, Peng and collaborators studied the decay of metastable skyrmions in FeGe lamellae with Lorentz transmission electron microscopy, showing that isolated skyrmions have longer lifetimes, hence higher energy barriers for the decay into the helical state, compared than skyrmions situated in the interior of the lattice.

In [79] is observed how the local ordering surrounding a single skyrmion, its position relative to the skyrmion lattice, influence its stability. In this context, the skyrmion lattice's stability can be assumed to be dependent on its local structure and local perfection. As observed and discussed before, the rocking curves at the edge of the sample characterised by high tilting angles, broader profiles and multiple peaks are descriptive of a skyrmion lattice made of multiple skyrmion domains, tilting away from the direction of the applied magnetic field differently. At the same time, the centre of the sample is characterised by single peaking rocking curves almost aligned with the direction of the external field and with smaller FWHM, descriptive of a more ordered skyrmion lattice, compared to the edge area. Furthermore, the presence of demagnetisation effects induces a co-existence of the skyrmion and conical phase, as it was shown in a large part of the magnetic phase diagram of MnSi [114]. Given the shape of the sample and our previous considerations on the higher demagnetisation effects present in the sample's edge area, a more pronounced co-existence of the skyrmion and the conical state is expected in this area compared to the centre. At the edge of the sample, the skyrmion lattice regularity is likely interrupted by the conical state, and the skyrmions at the border with the conical state have a higher stability than the skyrmions at the interior of the lattice [79]. A similar enhancement of the skyrmion stability could be caused by different types of interruption of the regularity of the skyrmion lattice, like the rotating neighbouring skyrmion domains. These two contributions, based on the local ordering of the skyrmion state, may explain the increased temperature range of the skyrmion pocket observed at the edge of the sample.

The unclear decaying behaviour observed at the edge is also worth discussing. The measurements in this area of the sample were performed at a lower applied magnetic field than the measurements in the centre of the sample. This difference in magnetic field is expected to change the metastable state's lifetime between the two areas. However, lower fields are generally associated with reduced lifetimes, rather than increased ones [51], as shown in our measurements. Moreover, the metastable state's lifetime is expected to be determined by the temperature difference between the target temperature of the cooling and the ordering temperature T_C [34, 67, 75]. Since no change in T_C was observed, one would expect the same Arrhenius temperature dependence of the lifetime both at the edge and in the centre of the sample. In this context, the unclear decaying behaviour observed at the edge of the sample is also possibly related to the skyrmion lattice's local ordering. In the presence of several skyrmion domains with different metastable behaviours and different regions of stability, it is possible to explain both the impossibility of fitting the decaying data with a single decaying exponential and the persistent scattered intensity of the skyrmion lattice presented in Figure 4.12(c) and 4.12(d).

Chapter 5

Bloch points velocity measurements in Zn substituted Cu$_2$OSeO$_3$

As mentioned in Section 1.1.4 and Chapter 4, the decay of the metastable skyrmion state is a process mediated by Bloch points that have been largely studied in several different samples and under different conditions [31, 42, 49, 51, 79]. The decay happens in a two-stage process: firstly, a pair of Bloch points is nucleated, and their subsequent motion across the length of the skyrmion tubes unwind the topologically non trivial state into the competing helical or conical states. When the skyrmion tubes decay into the helical state, the two Bloch points let two adjacent skyrmion tubes merge together, and their motion along the length of the tubes acts like a zipper [31]. When the decay is into the conical state, the pair of Bloch points is created along one single skyrmion tube, and their subsequent motion away from each other shortens the length of the tube [46, 74].

Most of the studies on the metastable skyrmion state focus on the measurement of its lifetime and the consequent determination of the energy barrier of the decay. Here we show how it is possible to determine the velocity of the Bloch point movement with small angle neutron scattering. We measure the decay of the metastable skyrmion state into the conical state in a single crystal of Zn substituted Cu_2OSeO_3. It was observed that the chemical substitution induces a shift of the skyrmion pocket, along with the whole $\boldsymbol{H}$-$\boldsymbol{T}$ phase diagram toward lower temperatures [71, 72]. The Zn ions also affect the metastable skyrmion state, acting as pinning sites that slow down the dynamic of the decay [49].

We analysed the decay through the length distribution of skyrmion tubes pieces, which is exponential, leading to a constant velocity for the movement of the Bloch points, which increases with the increasing of temperature.

5.1 Methods

A 2% Zn substituted single crystal of dimensions $(3 \times 2 \times 2)$ mm^3 was mounted in a cryomagnet and aligned with the [110] crystal axis along the direction of the neutron beam, and a [1$\bar{1}$0] axis vertical, perpendicular to the neutron beam. In the process of vertical alignment to the neutron beam, a pair of Cadmium strips were placed on top and at the bottom of the sample. The single crystal was grown by chemical vapour transport, as reported in [71], and illustrated in Chapter 2.

The direction of the magnetic field at the sample position was determined by aligning the scattering from the flux line lattice in superconducting Nb, as the magnetic vortexes align with the direction of the applied magnetic field [106]. All the measurements were performed with the magnetic field parallel to the neutron beam, applied along the [110] crystal axis. The neutron beam had a collimation

length of 7.8 m, and a wavelength of $\lambda = 6$ Å, with a FWHM fractional spread of $\Delta\lambda/\lambda = 10\%$. The scattered neutrons were detected 7.8 m after the sample with a two-dimensional multi-detector.

The structure of the skyrmion lattice along the direction of the applied neutron beam, hence the length of the skyrmion tubes, was studied collecting rocking curves performed by rotating the cryomagnet and the sample together about their vertical axis. The scattered intensity was measured as a function of this rocking angle ω. $\omega = 0$ was aligned to correspond to the direction of the applied magnetic field parallel to the incoming neutron beam.

The skyrmion metastable state was created by field cooling (FC) at 7 K/min from 60 K to several target temperatures in an applied field of 22 mT. The decay into the conical state was sampled by collecting rocking curves repeatedly once the target temperature was reached and stabilised. In all the measurements presented in this work, a paramagnetic background, measured at 60 K and 22 mT, was subtracted using GRASP software [116].

5.2 Results

Figure 5.1(a) shows the typical six-fold SANS pattern of the skyrmion state collected at 54 K, 22 mT, in the equilibrium skyrmion pocket. From the scattering, the momentum transfer was measured $q = 0.01003(2)$ Å^{-1}, corresponding to a characteristic spacing of $d = 2\pi/q = 62.7(9)$ nm, in agreement with what observed before in the same compound [49], in pristine Cu_2OSeO_3 [2, 86], and in the Ni substituted compound [80]. Figure 5.1(b) shows the rocking curve of the horizontal diffraction spots in Figure 5.1(a). As discussed in Chapter 4, the characteristics of the rocking curve give information on the structure of the skyrmion tubes along the direction of the incoming neutron beam. Specifically, the presence of multiple peaks identifies multiple skyrmion domains tilting away from the direction of the applied magnetic field ($\omega = 0$) by different angles. Moreover, the full width half maximum (FWHM) of the rocking curves is inversely proportional to the correlation length of the skyrmion tubes. The integrated intensity of the rocking curve is proportional to the population of that skyrmion domain. The rocking curve of the equilibrium skyrmion lattice shown in Figure 5.1(b) fitted to a sum of two Lorentzian functions, hence the presence of two skyrmion domains was identified. The presence of multiple peaks indicate strong demagnetisation effects bending the internal field lines, already shown in both MnSi [114] and $(Ni_xCu_{1-x})_2OSeO_3$, discussed in the previous chapter and published in [80].
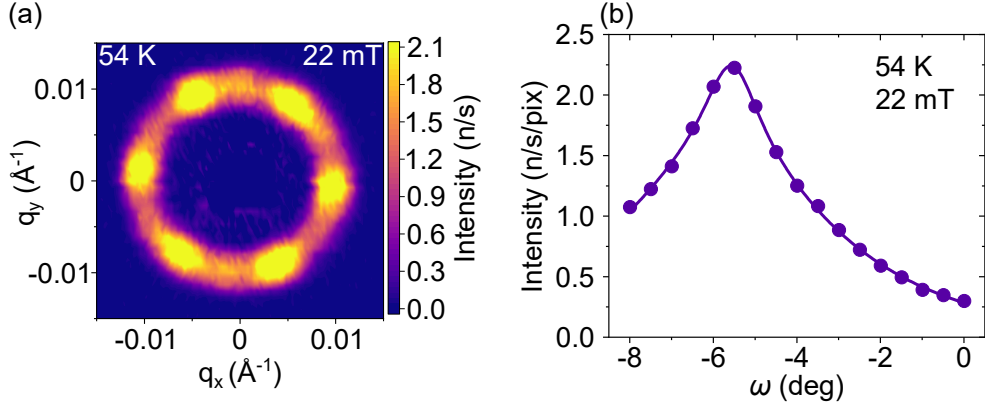
Figure 5.1: (a): small angle neutron scattering pattern measured in the middle of the skyrmion pocket, at 54 K and 22 mT. (b): rocking curve of the horizontal scattering spots of panel (a). The solid line corresponds to a fit of the data to a sum of two Lorentzian functions centered at $\omega_1 = -5.55(3)°$, $\omega_2 = -5.75(6)°$.

The time dependent behaviour of the metastable skyrmion state was measured by the collection of rocking curves repeatedly over time, at each target temperature. In this way, it was possible to follow both the intensity decay and the time dependent behaviour of the structure of the skyrmion lattice. In Figure 5.2 are shown the rocking curves collected at the beginning of these lifetime measurements. The rocking curve collected at 49.5 K shown in Figure 5.2(a) fitted well to the sum of two Lorentzian functions, indicated by the orange and purple lines, similarly to what observed in the skyrmion pocket in Figure 5.1(b). The other data shown in Figure 5.2(b-d), instead, fitted to a single Lorentzian function. However, as this set of data was taken over a smaller ω range, it is possible that other peaks of these rocking curves would show for ω outside the range. Another possibility is that additional skyrmion domains, peaking within the rocking angle range, were not visible due to their very broad FWHM profile.

To monitor the time dependent behaviour of the structure of the skyrmion tubes and their lifetime, both the FWHMs and the amplitudes of the Lorentzian functions fitted on the rocking curves are plotted versus time in Figure 5.3. For the 49.5 K dataset, the only amplitude and FWHM show are the ones of the most intense Lorentzian fitted (see Figure 5.2(a)), since it was identified as the main component of the rocking curve. The time dependency of the amplitudes shown in Figures 5.3(a, c, e, g) was fitted to a single exponential plus a flat background $y = y_0 + exp(-t/\tau)$. As it was discussed in Chapter 4, and shown in [80], demagnetisation effects can induce the presence of metastable skyrmion domains with different lifetimes, according to the local ordering of the skyrmion lattice. For this reason,
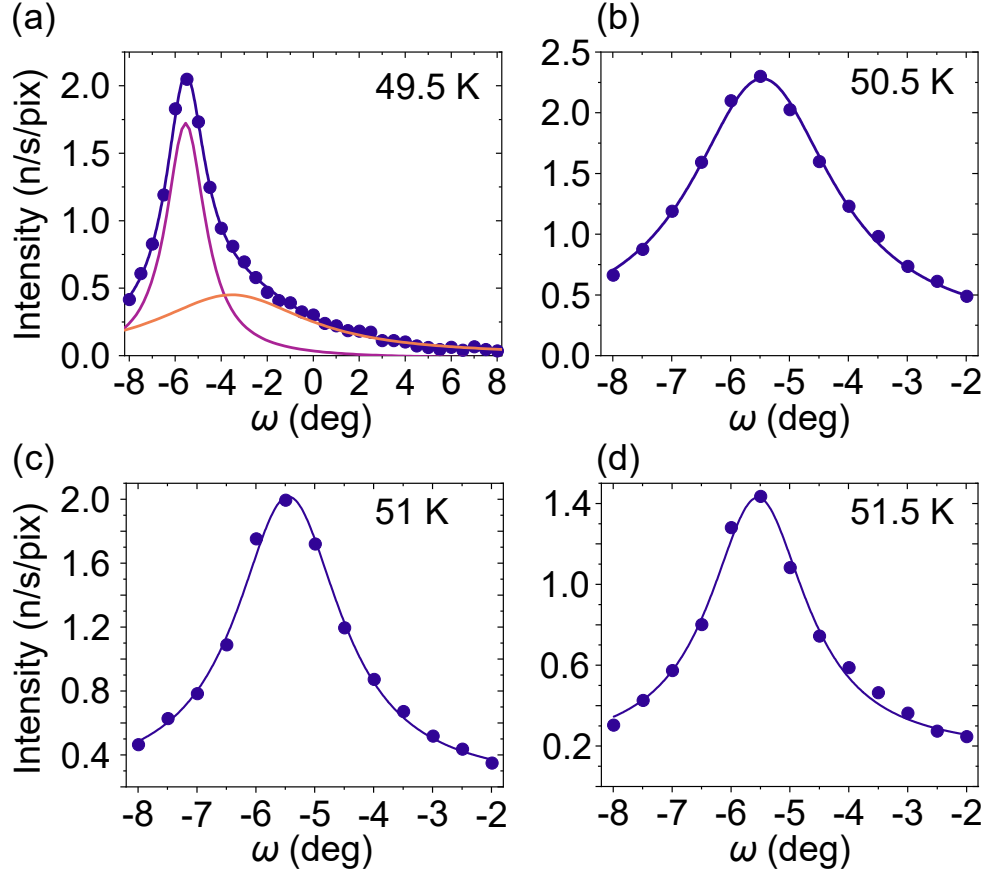
Figure 5.2: (a)-(d): first rocking curves recorded during the measurement of the lifetime of the metastable skyrmion lattice at each selected target temperature. All the measurements were performed after rapid FC in 22 mT from 60 K to each reported target temperatures. In panel (a), the solid blue line corresponds to the fit of the data to a sum of two Lorentzian functions, which are indicated by the solid lines in purple and orange. In panels (b) to (d), the solid line corresponds to a fit of a single Lorentzian function.

the added flat background takes into account those skyrmion domains which are decaying with a lifetime far longer than the timescale of the measurements, which were not visible in the rocking curve profile. In Figures 5.3(b, d, f, h) are shown the time dependencies of the FWHM of the rocking curves. Each data set was fitted to a linear function. The fitted slope value m is reported for each data set in the corresponding panel of Figure 5.3. The FWHM variation between the beginning and the end of the measurement was on the same order of magnitude as the mean error for all temperatures, with the exception of 51.5 K, as shown in Figure 5.3(h). For this data set, it is possible to notice that the amplitude time dependency deviated from an exponential profile. In the inset of Figure 5.3(g), where the amplitude decay is plotted in logarithmic scale, one can see the data do not follow a straight line (corresponding to the fit to the decaying exponential). This behaviour is indicative of the presence of metastable skyrmion domains with different decay times.

While the characteristic decay times decrease with increasing temperature, the FWHMs of the rocking curves stay almost constant over time and their value changes between $\sim 1.8°$ and $\sim 3°$ between different temperatures.

5.3   Discussion

It has previously been shown in MnSi [74] and in $Fe_{0.5}Co_{0.5}Si$ [31, 51] that the transformation of skyrmion tubes into another topologically trivial state of the magnetisation happens through the movement of Bloch points, singularities in the magnetisation state that exist at the point where two skyrmion tubes merge or where one skyrmion tube breaks. The motion of these Bloch points lets the topologically non trivial skyrmion state unwind into the conical, helical or ferromagnetic states. Recently, the various mechanism of decay of metastable skyrmion tubes in Zn substituted Cu_2OSeO_3 were thoroughly investigated in [117].

As mentioned before, the decay of the metastable skyrmion state is a two-stage process that starts with the nucleation of Bloch points. In the calculations shown here, the main assumption is that once nucleated, the number of Bloch points does not increase with time. Once nucleated, the Bloch points move across the skyrmion tubes, whose length shorten over the time of the decay. One might assume that the shortening of the lengths would correspond to a reduction in the mean correlation length, hence an increase of the rocking curve's FWHM over time. Indeed, no significant change of FWHM with time was observed. However, as shown below, this is what is expected for an exponential distribution of lengths where all lengths are reduced over time with a constant velocity.
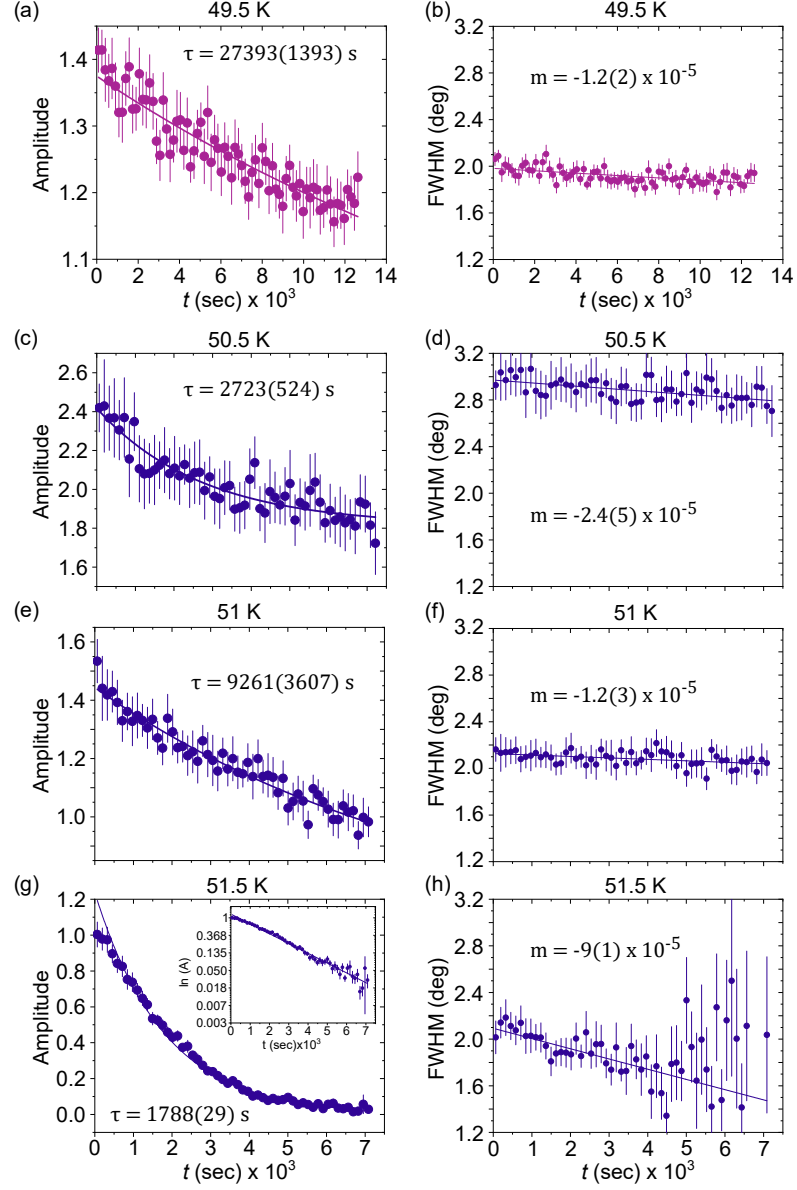
Figure 5.3: (a),(c),(e),(g): Lifetime of the metastable skyrmion state at the selected target temperatures, expressed by the time dependency of the fitted amplitude of the Lorentzian functions to the rocking curves measured. (b),(d),(f),(h): time dependency of the FWHM of the fitted Lorentzian functions to the rocking curves measured. The data were fitted to a linear function $y = mx + y_0$. The fitted slope value m is reported in each panel for each temperature. In panel (a) and (b), only the amplitude and FWHM, respectively, of the main component of the rock are presented. The colour used for the data in panel (a) and (b) corresponds to the colour of the fitted Lorentzian function in Figure 5.2(a), identifying the main component studied.

Let us consider one skyrmion tube broken at random by Bloch points. This problem is analogous to the one of a stick of a finite length broken at random, presented in [118]. Here the distribution of lengths is exactly calculated and proven to be an exponential distribution, assuming that the breaking of the stick is a Poisson process. Analogously, assuming the creation of Bloch points is as well a Poisson process, the distribution of lengths obtained by randomly breaking a skyrmion tube with them will be exponential:

$$P(x) = e^{-\frac{x}{x_0}} dx, \tag{5.1}$$

where x_0 is the mean length of the pieces of skyrmion tubes, and $P(x) = 0$ for $x > L_{max}$, where L_{max} is the sample size in the direction of the applied field. Given this distribution of lengths, the sum of all of them should be proportional to the scattered intensity, which can be written as:

$$T = \int_0^{L_{max}} e^{-\frac{x}{x_0}} dx = x_0 \left(1 - e^{-\frac{L_{max}}{x_0}} \right). \tag{5.2}$$

Equation 5.2 is valid as long as the number of Bloch points do not increase with time. The weighted sum of the lengths is:

$$I = \int_0^{L_{max}} x \, e^{-\frac{x}{x_0}} dx = x_0^2 \left(1 - e^{-\frac{L_{max}}{x_0}} \right) - x_0 L_{max} e^{-\frac{L_{max}}{x_0}}. \tag{5.3}$$

From Equations 5.2 and 5.3 it is possible to write the expected value as:

$$\bar{x} = \frac{I}{T} = x_0 - \frac{L_{max} e^{-\frac{L_{max}}{x_0}}}{1 - e^{-\frac{L_{max}}{x_0}}}, \tag{5.4}$$

which gives $\bar{x} = x_0$ when L_{max} is very big, as expected since L_{max} is in the order of mm and x_0 in the order of nm. Let us now consider Bloch points breaking the skyrmion tubes, and moving along them at a velocity v. In this case, the probability distribution of lengths in Equation 5.1 shifts towards lower values of lengths, as they are shortening by $2vt$. For the same reason, the maximum length is also shortening $L_{max} \to L_{max} - 2vt$. In this case, Equation 5.1 can be written as:

$$P(x, t) = e^{-\frac{(x+2vt)}{x_0}} dx. \tag{5.5}$$

While the total of all lengths, proportional to the scattered intensity, becomes:

$$T(t) = \int_0^{L_{max}-2vt} e^{-\frac{(x+2vt)}{x_0}} dx = x_0 e^{-\frac{2vt}{x_0}} \left(1 - e^{-\frac{(L_{max}-2vt)}{x_0}}\right), \qquad (5.6)$$

giving an intensity decaying exponentially with a characteristic time of $\tau = x_0/(2v)$, consistent with our observations. The time dependent weighted sum becomes:

$$\begin{aligned}
I(t) &= \int_0^{L_{max}-2vt} x\ e^{-\frac{(x+2vt)}{x_0}} dx \\
&= e^{-\frac{2vt}{x_0}} \left(x_0^2 \left(1 - e^{-\frac{L_{max}-2vt}{x_0}}\right) - x_0(L_{max} - 2vt)e^{-\frac{L_{max}-2vt}{x_0}}\right), \quad (5.7)
\end{aligned}$$

giving a time dependent mean length of:

$$\bar{x}(t) = \frac{I(t)}{T(t)} = x_0 - \frac{(L_{max} - 2vt)\,e^{-\frac{(L_{max}-2vt)}{x_0}}}{1 - e^{-\frac{(L_{max}-2vt)}{x_0}}}, \qquad (5.8)$$

which is constant over time for $2vt << L_{max}$. As the correlation lengths of the skyrmion tubes are in the order of 10^4 Å, four orders of magnitude smaller than L_{max}, Equation 5.8 supports the observation of a constant mean length of the skyrmion tubes over time. The only target temperature at which the FWHM shows a time dependence, presented in Figure 5.3(h), corresponded to a decaying amplitude not showing a simple exponential decaying behaviour, as shown in the inset of Figure 5.3(g).

In Figure 5.4 is presented the temperature dependence of the velocity of the unwinding of the skyrmion tubes into the conical state. The calculated values of the velocity support our assumption $2vt << L_{max}$, as the time needed to unwind a skyrmion tube as long as L_{max} is in the order of years for all the calculated velocities. The velocity increases with increasing temperature but shows a valley at 51 K. The increase with increasing temperature is in contrast with simulations performed Bloch points dynamics in the decay of a single skyrmion string into the helical state [46].

5.4   Conclusions

We observed the dynamic of Bloch points during the decay of the metastable skyrmion lattice in a single crystal of Zn substituted Cu_2OSeO_3 with SANS. Specif-
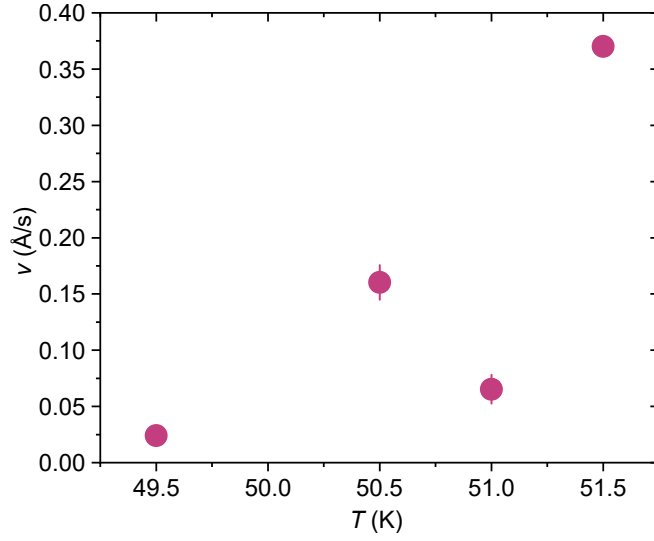
Figure 5.4: Temperature dependence of the unwrapping velocity of the skyrmion tubes. The values were obtained following the calculations given in the text.

ically, it was possible to extract the velocity of the Bloch points moving along the skyrmion tubes, and allowing the decay into the conical state. The velocity was calculated from the decay's characteristic lifetime, extracted from the time dependence of the scattered intensity, and from the average correlation length of the skyrmion tubes, extracted from the FWHM of the rocking curves of the skyrmion lattice. The average correlation length of the skyrmion tubes remains constant over the time of the decay. This effect is a direct consequence of the exponential distribution of skyrmion tube's lengths created by the nucleation of Bloch points at the beginning of the decay process. The calculated velocity of the Bloch points increases linearly with increasing temperature, as the thermal energy of the system is higher. Our calculations relies on the assumption that the number of nucleated Bloch points at the beginning of the decay does not increase over time. Moreover, we assumed that the FWHM of the rocking curves is representative of the average distance between two Bloch points along the skyrmion tube. However, the rocking curve width is also related to the average correlation length of a skyrmion tube, in this case measured along the direction of the applied magnetic field and incoming neutron beam. The average correlation length is affected both by the actual length of the skyrmion tubes, and by distortions present along their length. Both these characteristics are responsible for the finite FWHM observed in the rocking curves, as thoroughly discussed in Chapter 4. There, the demagnetising field was shown to be responsible for bending the internal magnetic field direction, followed by the skyrmon tubes. This affected the FWHM of the rocking curves of the skyrmion lattice, and the cor-

responding average correlation length measured. The demagnetising field was also shown to be responsible for the coexistence of conical and skyrmion states. This coexistence directly affected the length of the skyrmion tubes, resulting in wider rocking curves, and affecting the average correlation length measured.

In a previous work [46], the decay of a single skyrmion tube was modelled with different numerical methods, and the velocity of the Bloch points was predicted to be weakly dependent on temperature, while decreasing with increasing temperature. Although our observations differ from what predicted in [46], it is worth mentioning that in this simulation work the skyrmion tubes were modelled to decay into the helical state through the shortening of their length, instead of the *zipper* dynamic which has more recently been identified as the decay behaviour when passing from the skyrmion to the helical state [31, 51, 74, 117]. Further measurements, possibly with different techniques, are needed to characterise the dynamic of Bloch points fully.

With these measurements, we also highlight the versatility of small angle neutron scattering. We show how it is possible to study both the structure of the skyrmion lattice and the dynamic of Bloch points in its decay.

Chapter 6

Summary and Conclusions

In this work, the properties of the skyrmion state have been studied with small angle neutron scattering measurements in pristine and chemically substituted single crystals of Cu_2OSeO_3. Particular attention has been given to the identification of mechanisms that would affect the stability of the skyrmion lattice, as in hydrostatic pressure and demagnetisation effects. Moreover, it is also shown how the metastable skyrmion tubes' unwinding mechanism can be studied through SANS measurements.

We observed minor distortions of the phase diagram of pristine Cu_2OSeO_3 under the application of quasi-hydrostatic pressure. A shift of the phase diagram is observed towards higher temperatures, with a small enhancement of the skyrmion pocket's size, while the critical fields are only weakly affected. We concluded that the main effects of the application of quasi-hydrostatic pressure are the increase of the Dzyaloshinskii-Moriya interaction term and a concomitant increase of the magnetic anisotropy, responsible for the increased size of the skyrmion pocket. We identified quasi-hydrostatic pressure as a third thermodynamic variable that could be exploited to stabilise skyrmions at higher temperatures. We also underlined the importance of the choice of pressure transmitting medium, as the skyrmion stability is the result of a fine interplay between magnetic interactions.

We also show the effect the macroscopic shape of the sample has on the stability and metastability of the skyrmion state on a big Ni substituted Cu_2OSeO_3 single crystal. Demagnetisation effects are usually disregarded as it is very difficult to compute the correct demagnetising field of complex sample shapes. Nonetheless, our measurements show how the demagnetising field can induce an enlargement of the skyrmion pocket in specific areas of the sample, allowing the coexistence of the conical and skyrmion states. This increased stability is yet to be completely understood, as it relies on the local ordering of a topologically non trivial state. Moreover,

the local ordering also affected the metastable skyrmion state decay, inducing a remarkably long lifetime in certain areas of the sample. A more complete study of the effects of the local ordering of the skyrmion lattice on its stability and metastability would be of great interest to understand the link between a topologically non trivial state's stability and its ordering.

We also studied in detail the unwinding mechanism of metastable skyrmion tubes in Zn substituted Cu_2OSeO_3. We provided a simple mathematical method for the extraction of the velocity of the Bloch points motion in the decay from the lifetime and the average correlation length of the skyrmion tubes. Considering a number of Bloch points that do not increase with time, we observed a velocity of the unwinding mechanism that increases with increasing temperature, as the thermal energy of the system increases. Our measurements show how SANS can be used to gather information on the dynamics of Bloch points, in addition to its more common use for gathering information on the magnetic structure of materials.

Bibliography

1. Nagaosa, N. & Tokura, Y. Topological properties and dynamics of magnetic skyrmions. *Nat. Nano.* **8,** 899 (2013).

2. Seki, S., Yu, X. Z., Ishiwata, S. & Tokura, Y. Observation of Skyrmions in a Multiferroic Material. *Science* **336,** 198 (2012).

3. Chatterji, T. *et al. Neutron Scattering from Magnetic Materials* (ed Chatterji, T.) ISBN: 978-0-444-51050-1 (Elsevier, 2006).

4. Pynn, R. *Neutron Scattering—A Non-destructive Microscope for Seeing Inside Matter* (eds Liang, L., Rinaldi, R. & Schober, H.) 15–36. ISBN: 978-0-387-09416-8 (Springer US, 2009).

5. Boothroyd, A. T. *Principles of Neutron Scattering from Condensed Matter* ISBN: 978–0–19–886231–4 (Oxford University Press, 2020).

6. Mühlbauer, S. *et al.* Magnetic small-angle neutron scattering. *Rev. of Modern Physics* **91,** 1–75 (2019).

7. Cubitt, R. *et al.* Neutron diffraction by the flux lattice in high-T_C superconductors. *Physica B: Physics of Condensed Matter* **180-181,** 377–379 (1992).

8. Skyrme, T. H. R. A unified field theory of mesons and baryons. *Nuclear Physics* **31,** 556–559 (1962).

9. Wright, D. C. & Mermin, N. D. Crystalline liquids: The blue phases. *Rev. of Mod. Phys.* **61,** 385–432 (1989).

10. Sondhi, S. L., Karlhede, A., Kivelson, S. A. & Rezayi, E. H. Skyrmions and the crossover from the integer to fractional quantum Hall effect at small Zeeman energies. *Phys. Rev. B* **47,** 16419–16426 (1993).

11. Ho, T. H. Spinor bose condensates in optical traps. *Phys. Rev. Lett.* **81,** 742–745 (1998).

12. Thermodynamically stable "vortices" in magnetically ordered crystals. The mixed state of magnets. *Zh. Eksp. Teor. Fiz* **95,** 178 (1989).

13. Bogdanov, A. N. & Hubert, A. Thermodynamically stable magnetic vortex states in magnetic crystals. *Journal of Magnetism and Magnetic Materials* **138,** 255–269 (1994).

14. Bogdanov, A. N. & Rößler, U. B. Chiral symmetry breaking in magnetic thin films and multilayers. *Phys. Rev. Lett.* **87,** 37203–1–37203–4 (2001).

15. Rößler, U. K., Bogdanov, A. N. & Pfleiderer, C. Spontaneous skyrmion ground states in magnetic metals. *Nature* **442,** 797–801 (2006).

16. Mühlbauer, S. *et al.* Skyrmion Lattice in a Chiral Magnet. *Science* **323,** 915 (2009).

17. Yu, X. Z. *et al.* Real-space observation of a two-dimensional skyrmion crystal. *Nature* **465,** 901–4 (2010).

18. Wilhelm, H. *et al.* Precursor Phenomena at the Magnetic Ordering of the Cubic Helimagnet FeGe. *Phys. Rev. Lett.* **107,** 127203 (2011).

19. Kurumaji, T. *et al.* Skyrmion lattice with a giant topological Hall effect in a frustrated triangular-lattice magnet. *Science* **365,** 914–918 (2019).

20. Hirschberger, M. *et al.* Skyrmion phase and competing magnetic orders on a breathing kagomé lattice. *Nat. Comm.* **10,** 1–9 (2019).

21. Tokunaga, Y. *et al.* A new class of chiral materials hosting magnetic skyrmions beyond room temperature. *Nat. Commun.* **6,** 7638 (2015).

22. Yu, X. Z. *et al.* Near room-temperature formation of a skyrmion crystal in thin-films of the helimagnet FeGe. *Nature Mater.* **10,** 106 (2011).

23. Heinze, S. *et al.* Spontaneous atomic-scale magnetic skyrmion lattice in two dimensions. *Nat. Phys.* **7,** 713–718 (2011).

24. Moreau-Luchaire, C. *et al.* Additive interfacial chiral interaction in multilayers for stabilization of small individual skyrmions at room temperature. *Nat. Nano.* **11,** 444–448 (2016).

25. Jonietz, F. *et al.* Spin Transfer Torques in MnSi at Ultralow Current Densities. *Science,* 1648–1652 (2011).

26. Everschor, K., Garst, M., Duine, R. A. & Rosch, A. Current-induced rotational torques in the skyrmion lattice phase of chiral magnets. *Phys. Rev. B* **84,** 064401 (6 2011).

27. Zhang, X. *et al.* Skyrmion-electronics: Writing, deleting, reading and processing magnetic skyrmions toward spintronic applications. *J. Phys.: Condens. Matter* **32** (2020).

28. Everschor, K., Masell, J., Reeve, R. M. & Klaui, M. Perspective: Magnetic skyrmions — Overview of recent progress in an active research field. *J. Appl. Phys.* **24,** 240901 (2018).

29. Kovalev, A. A. & Sandhoefner, S. Skyrmions and antiskyrmions in quasi-two-dimensional magnets. *Frontiers in Physics* **6,** 1–8 (2018).

30. Seki, S. & Mochizuki, M. *Skyrmions in Magnetic Materials* (SpingerBriefs in Physics, 2016).

31. Milde, P. *et al.* Unwinding of a Skyrmion Lattice by Magnetic Monopoles. *Science* **340,** 1076 (2013).

32. Beausoleil, W. F., Brown, D. T. & Phelps, B. E. Magnetic Bubble Memory Organization. *IBM Journal of Research and Development* **16,** 587–591 (1972).

33. Moutafis, C. *et al.* Magnetic bubbles in FePt nanodots with perpendicular anisotropy. *Phys. Rev. B* **76,** 1–5 (2007).

34. Karube, K. *et al.* Metastable skyrmion lattices governed by magnetic disorder and anisotropy in β-Mn-type chiral magnets. *Phys. Rev. B* **102,** 064408 (6 2020).

35. Okubo, T., Chung, S. & Kawamura, H. Multiple-q states and the Skyrmion lattice of the triangular-lattice Heisenberg antiferromagnet under magnetic fields. *Phys. Rev. Lett.* **108,** 1–5 (2012).

36. Bak, J. & Jensen, M. H. Theory of helical magnetic structures and phase transitions in MnSi and FeGe. *J. Phys. C: Solid State Phys* **13,** 881 (1980).

37. Garel, T. & Doniach, S. Phase transitions with spontaneous modulation-the dipolar Ising ferromagnet. *Phys. Rev. B* **26,** 325–329 (1982).

38. Grigoriev, S. V. *et al.* Flip of spin helix chirality and ferromagnetic state in $Fe_{1-x}Co_xGe$ compounds. *Phys. Rev. B* **90,** 1–5 (2014).

39. Michels, A., Mettus, D., Honecker, D. & Metlov, K. L. Effect of Dzyaloshinski-Moriya interaction on elastic small-angle neutron scattering. *Phys. Rev. B* **94,** 1–10 (2016).

40. Cullity, B. D. & Graham, C. D. *Introduction to Magnetic Materials* **6.** ISBN: 978-0-471-47741-9 (John Whiley and Sons, 2011).

41. Nakajima, T. *et al.* Skyrmion lattice structural transition in MnSi. *Sci. Adv.* **3,** 1602562 (2017).

42. Karube, K. *et al.* Robust metastable skyrmions and their triangular–square lattice structural transition in a high-temperature chiral magnet. *Nat. Mater.* **15,** 1237 (2016).

43. Chacon, A. *et al.* Observation of two independent skyrmion phases in a chiral magnetic material. *Nat. Phys.* **14,** 936–941 (2018).

44. Halder, M. *et al.* Thermodynamic evidence of a second skyrmion lattice phase and tilted conical phase in Cu_2OSeO_3. *Phys. Rev. B* **94,** 1–19 (2018).

45. Bannenberg, L. J. *et al.* Skyrmions and spirals in MnSi under hydrostatic pressure. *Phys. Rev. B* **100,** 054447 (5 Aug. 2019).

46. Schütte, C. & Rosch, A. Dynamics and energetics of emergent magnetic monopoles in chiral magnets. *Phys. Rev. B* **90,** 174432 (2014).

47. Zhang, S. *et al.* Reciprocal space tomography of 3D skyrmion lattice order in a chiral magnet. *PNAS* **115,** 6386–6391 (2018).

48. Rybakov, F. N., Borisov, A. B., Blügel, S. & Kiselev, N. S. New Type of Stable Particlelike States in Chiral Magnets. *Phys. Rev. Lett.* **115,** 117201 (2015).

49. Birch, M. T. *et al.* Increased lifetime of metastable skyrmions by doping. *Phys. Rev. B* **100,** 014425 (2019).

50. Kanazawa, N. *et al.* Critical phenomena of emergent magnetic monopoles in a chiral magnet. *Nat. Comm.* **7,** 1–7 (2016).

51. Wild, J. *et al.* Entropy-limited topological protection of skyrmions. *Sci. Adv.* **3,** 1701704 (2017).

52. Leonov, A. O. & Inoue, K. Homogeneous and heterogeneous nucleation of skyrmions in thin layers of cubic helimagnets. *Phys. Rev. B* **98,** 054404 (5 2018).

53. Wilson, M. N. *et al.* Measuring the formation energy barrier of skyrmions in zinc-substituted Cu_2OSeO_3. *Phys. Rev. B* **99,** 174421 (17 2019).

54. Zheng, F. *et al.* Experimental observation of chiral magnetic bobbers in B20-type FeGe. *Nat. Nano* **13,** 451–455 (2018).

55. Yi, S. D., Onoda, S., Nagaosa, N. & Han, J. H. Skyrmions and anomalous Hall effect in a Dzyaloshinskii-Moriya spiral magnet. *Phys. Rev. B* **80,** 054416 (2009).

56. Okamura, Y., Kagawa, F., Seki, S. & Tokura, Y. Transition to and from the skyrmion lattice phase by electric fields in a magnetoelectric compound. *Nat. Commun.* **7,** 12669 (2016).

57. Kruchkov, A. J. *et al.* Direct control of the skyrmion phase stability by electric field in a magnetoelectric insulator. *Sci. Rep.* **8,** 10466 (2018).

58. White, J. S. *et al. Phys. Rev. B* **97,** 020401 (2018).

59. Chacon, A. *et al.* Uniaxial Pressure Dependence of Magnetic Order in MnSi. *Phys. Rev. Lett.* **115,** 267202 (2015).

60. Nii, Y. *et al.* Uniaxial stress control of skyrmion phase. *Nat. Commun.* **6,** 8539 (2015).

61. Nakajima, T. *et al.* Uniaxial-stress Effects on Helimagnetic Orders and Skyrmion Lattice in Cu_2OSeO_3. *J. Phys. Soc. Jpn.* **87,** 094709 (2018).

62. Sidorov, V., Petrova, A., Berdonosov, P., Dolgikh, V. & Stishov, S. Comparative Study of helimagnets MnSi and Cu_2OSeO_3 at high pressures. *Phys. Rev. B* **89,** 100403(R) (2014).

63. Wu, H. C. *et al.* Physical pressure and chemical expansion effects on the skyrmion phase in Cu_2OSeO_3. *Sci. Rep.* **5,** 13579 (2015).

64. Levatić, I. *et al.* Dramatic pressure-driven enhancement of bulk skyrmion stability. *Sci. Rep.* **6,** 21347 (2016).

65. Crisanti, M. *et al.* In situ control of the helical and skyrmion phases in Cu_2OSeO_3 using high-pressure helium gas up to 5 kbar. *Phys. Rev. B* **101,** 1–9 (2020).

66. Bauer, A., Garst, M. & Pfleiderer, C. History dependence of the magnetic properties of single-crystal $Fe_{1-x}Co_xSi$. *Phys. Rev. B* **93,** 235144 (June 2016).

67. Karube, K. *et al.* Skyrmion formation in a bulk chiral magnet at zero magnetic field and above room temperature. *Phys. Rev. Materials* **1,** 074405 (2017).

68. Franke, K. J. A. *et al.* Magnetic phases of skyrmion-hosting $GaV_4S_{8-y}Se_y$ ($y = 0, 2, 4, 8$) probed with muon spectroscopy. *Phys. Rev. B* **98,** 054428 (5 2018).

69. Hicken, T. J. *et al.* Magnetism and Néel skyrmion dynamics in $GaV_4S_{8-y}Se_y$. *Phys. Rev. Research* **2,** 032001 (3 2020).

70. Chandrasekhar, K. D., Wu, H. C., Huang, C. L. & Yang, H. D. Effects of Jahn–Teller distortion on the skyrmion stability of $(Cu_{1-x}Ni_x)_2OSeO_3$. *J. Mater. Chem. C* **4,** 5270 (2016).

71. Štefančič, A. *et al.* Origin of skyrmion lattice phase splitting in Zn-substituted Cu_2OSeO_3. *Phys. Rev. Mat.* **111402(R),** 1–5 (2018).

72. Sukhanov, A. S. *et al.* Increasing skyrmion stability in Cu_2OSeO_3 by chemical substitution Cu$_2$OSeO$_3$. *Phys. Rev. B* **100,** 184408 (2019).

73. Münzer, W. *et al.* Skyrmion lattice in the doped semiconductor $Fe_{1-x}Co_xSi$. *Phys. Rev. B* **81,** 041203(R) (2010).

74. Kagawa, F. *et al.* Current-induced viscoelastic topological unwinding of metastable skyrmion strings. *Nat. Commun.* **8,** 1332 (2017).

75. Oike, H. *et al.* Interplay between topological and thermodynamic stability in a metastable magnetic skyrmion lattice. *Nat. Phys.* **12,** 62 (2016).

76. Morikawa, D. *et al.* Deformation of Topologically-Protected Supercooled Skyrmions in a Thin Plate of Chiral Magnet $Co_8Zn_8Mn_4$. *Nano Lett.* **17,** 1637 (2017).

77. Milde, P. *et al.* Heuristic Description of Magnetoelectricity of Cu_2OSeO_3. *Nano Lett.* **16,** 5612 (2016).

78. Milde, P., Neuber, E., Bauer, A., Pfleiderer, C. & Eng, L. M. Surface pinning and triggered unwinding of skyrmions in a cubic chiral magnet. *Phys. Rev. B* **100,** 37–40 (2019).

79. Peng, L. *et al.* Relaxation Dynamics of Zero-Field Skyrmions over a Wide Temperature Range. *Nano Letters* **18,** 7777–7783 (2018).

80. Crisanti, M. *et al.* Position-dependent stability and lifetime of the skyrmion state in nickel-substituted Cu_2OSeO_3. *Phys. Rev. B* **102,** 29–32 (2020).

81. Ashcroft, N. W. & Mermin, N. D. *Solid State Physics* (Holt-Saunders, 1976).

82. Coey, J. M. D. *Magnetism and Magnetic Materials* ISBN: 978-0-511-67743-4 (Cambridge University Press, 2009).

83. Neutron diffraction studies of flowing and pinned magnetic flux lattices in 2H-NbSe2. *Phys. Rev. Lett.* **73,** 2748–2751 (1994).

84. Toft-Petersen, R., Abrahamsen, A. B., Balog, S., Porcar, L. & Laver, M. Decomposing the Bragg glass and the peak effect in a Type-II superconductor. *Nat. Comm.* **9** (2018).

85. Kanazawa, N. *et al.* Possible skyrmion-lattice ground state in the $B20$ chiral-lattice magnet MnGe as seen via small-angle neutron scattering. *Phys. Rev. B* **86,** 134425 (13 2012).

86. Adams, T. *et al.* Long-Wavelength Helimagnetic Order and Skyrmion Lattice Phase in Cu_2OSeO_3. *Phys. Rev. Lett.* **108,** 237204 (2012).

87. Seki, S., Ishiwata, S. & Tokura, Y. Magnetoelectric nature of skyrmions in a chiral magnetic insulator Cu_2OSeO_3. *Phys. Rev. B* **86,** 060403(R) (2012).

88. Ruff, E., Lunkenheimer, P., Loidl, A., Berger, H. & Krohns, S. Magnetoelectric effects in the skyrmion host material Cu_2OSeO_3. *Sci. Rep.* **5,** 15025 (2015).

89. Bos, J.-W. G., Colin, C. V. & Palstra, T. T. M. Magnetoelectric coupling in the cubic ferrimagnet Cu_2OSeO_3. *Phys. Rev. B* **78,** 094416 (2008).

90. Seki, S. *et al.* Formation and rotation of skyrmion crystal in the chiral-lattice insulator Cu_2OSeO_3. *Phys. Rev. B* **85,** 220406 (2012).

91. White, J. S. *et al.* Electric field control of the skyrmion lattice in Cu_2OSeO_3. *J. Phys.: Condens. Matter* **24,** 432201 (2012).

92. White, J. S. *et al.* Electric-Field-Induced Skyrmion Distortion and Giant Lattice Rotation in the Magnetoelectric Insulator Cu_2OSeO_3. *Phys. Rev. Lett.* **113,** 107203 (10 2014).

93. Zhang, S. L. *et al.* Resonant elastic x-ray scattering from the skyrmion lattice in Cu_2OSeO_3. *Phys. Rev. B* **93,** 214420 (2016).

94. Wu, H. C. *et al.* Unexpected observation of splitting of skyrmion phase in Zn doped Cu_2OSeO_3. *J. Phys. D: Appl. Phys.* **48,** 475001 (2015).

95. Magnusson, J., Djurberg, C., Granberg, P. & Nordblad, P. A low field superconducting quantum interference device magnetometer for dynamic measurements. *Review of Scientific Instruments* **68,** 3761–3765 (1997).

96. https://www.ill.eu/users/instruments/instruments-list/orientexpress/description/instrument-layout/.

97. Pedrazzini, P. *et al.* Metallic State in Cubic FeGe Beyond Its Quantum Phase Transition. *Phys. Rev. Lett.* **98,** 047204 (2007).

98. Pfleiderer, C., Julian, S. R. & Lonzarich, G. G. Non-Fermi-liquid nature of the normal state of itinerant-electron ferromagnets. *Nature* **414,** 427 (2001).

99. Pfleiderer, C., McMullan, G. J., Julian, S. R. & Lonzarich, G. G. Magnetic quantum phase transition in MnSi under hydrostatic pressure. *Phys. Rev. B* **55,** 8330–8338 (13 1997).

100. Ritz, R. *et al.* Giant generic topological Hall resistivity of MnSi under pressure. *Phys. Rev. B* **87,** 134424 (2013).

101. Klotz, S. *Techniques in high pressure neutron scattering* ISBN: 978-1-4398-3562-3 (CRC Press, 2012).

102. Huang, P. *et al.* In situ Electric Field Skyrmion Creation in Magnetoelectric Cu_2OSeO_3. *Nano Lett.* **18,** 5167–5171 (2018).

103. Makino, K. *et al.* Thermal stability and irreversibility of skyrmion-lattice phases in Cu_2OSeO_3. *Phys. Rev. B* **95,** 134412 (2017).

104. Bannenberg, L. J. *et al.* Reorientations, relaxations, metastabilities, and multidomains of skyrmion lattices. *Phys. Rev. B* **96,** 184416 (2017).

105. Torikachvili, M. S., Kim, S. K., Colombier, E., L., B. S. & Canfield, P. C. Solidification and loss of hydrostaticity in liquid media used for pressure measurements. *Rev. Sci. Instr.* **86,** 123904 (2015).

106. Forgan, E. *et al.* Intrinsic Behavior of Flux Lines in Pure Niobium near the Upper Critical Field. *Phys. Rev. Lett.* **88** (2002).

107. Richard, D., Ferrand, M. & Kearley, G. Analysis and visualisation of neutron-scattering data. *J. Neutron Research* **4,** 34–39 (1996).

108. Tengattini, A. *et al.* NeXT-Grenoble, the neutron and X-ray tomography in Grenoble. *Nuclear Inst. and Methods in Physics Research A* (2020).

109. Clark, S. *et al.* First principles methods using CASTEP. *Z. Kristallogr - Cryst. Mater.* **200,** 567 (2009).

110. Perdew, J., Burke, K. & Ernzerhof, M. Generalized Gradient Approximation Made Simple. *Phys. Rev. Lett.* **77,** 3865–3868 (18 1996).

111. Monkhorst, H. & Pack, J. Special points for Brillouin-zone integrations. *Phys. Rev. B* **13,** 5188–5192 (12 1976).

112. Bauer, A. & Pfleiderer, C. Magnetic phase diagram of MnSi inferred from magnetization and ac susceptibility. *Phys. Rev. B* **85,** 214418 (2012).

113. Birch, M. T. *et al.* Anisotropy-induced depinning in the Zn-substituted skyrmion host Cu_2OSeO_3. *Phys. Rev. B* **102,** 104424 (10 2020).

114. Reimann, T. *et al.* Neutron diffractive imaging of the skyrmion lattice nucleation in MnSi. *Phys. Rev. B* **97,** 020406(R) (2018).

115. Joseph, R. I. & Schlömann, E. Demagnetizing filed in nonellipsoidal bodies. *Journal of Applied Physics* **36,** 1579 (1965).

116. C. D. Dewhurst, GRASP User Manual, Technical Report No. ILL03DE01T, Institut Laue- Langevin, Grenoble (2003), available at: www.ill.fr/lss/grasp.

117. Birch, M. T. *et al.* Bloch point-mediated skyrmion annihilation in three dimensions. **arXiv:2012.14813** (2021).

118. Holst, L. On the Lengths of the Pieces of a Stick Broken at Random. *Journal of Applied Probability* **17,** 623–634 (1980).